0485: Validate Production of Neutrons from Gas Gun-Driven Targets

G. C. Burdiak [Lead author], J. W. Skidmore [Lead experimentalist], J. R. Allison, R. L. Barker, H. W. Doyle, E. M. Escauriza, N.-P. L. Niasse, Z. Pešić, T. J. Ringrose, N. A. Hawker

First Light Fusion Ltd., Unit 10 Oxford Industrial Park, Yarnton, OX5 1QU, United Kingdom

(Dated: April 4, 2022)

We describe an experimental campaign to confirm the production of deuterium-deuterium (DD) fusion neutrons by an inertial confinement fusion target that is driven by a one-sided impact. Experiments were performed on First Light Fusion's 38 mm bore, two-stage light gas gun. This facility can launch a 100 g solid projectile at 6.5 km s^{-1}. Neutron diagnostics included scintillators and moderated helium-3 proportional counters.

We have demonstrated repeatable, coincident detection of particles on multiple scintillator detectors, within the expected time window. Background contribution to the dataset was found to be negligible. In null shots, where the DD fuel was replaced with hydrogen, no particles were observed. These results indicate that dynamics within a DD target result in the generation of energetic particles. The number of scintillator hits recorded dropped off according to the solid angle subtended by detector groups at different distances, consistent with a particle source at the target location.

The nature of the energetic particles was determined using He-3 detectors and scintillator-based time-of-flight measurements. The shot-aggregated He-3 detector dataset demonstrates that neutron levels within the anticipated detection time window are well above background. The particle arrival time at scintillators positioned at different distances from the source was used to determine the particle velocity. Additionally, a fusion event timing fiducial inserted into each target provided an additional point (at $x = 0$) for assessing particle time-of-flight. On multiple shots, time-of-flight data was recorded that is consistent with the propagation of 2.45 MeV DD fusion neutrons. Assuming a neutron mass, an average particle energy of 2.46 ± 0.3 MeV was determined, which, within error, is in agreement with the energy of an unscattered DD fusion neutron. No data was recorded that is consistent with the propagation of target generated photons.

Estimates of neutron yield from the detected number of hits on both detector types are in agreement. The scintillators and He-3 proportional counters were independently, absolutely calibrated for their 2.5 MeV counting efficiency. Consistency between the two detector types therefore provides further evidence that observed counts were induced by a common source of DD fusion neutrons.

The collective evidence presented leads to the conclusion that DD fusion neutrons have been observed and that they were produced within targets driven by FLF's large two-stage gas gun. The UK Atomic Energy Authority (UKAEA) have verified the experimental setup, modelled the detector responses and witnessed two experiments. They have also reviewed the full campaign dataset, analysis and interpretation of the results.

CONTENTS

I. INTRODUCTION

A. Overview of the FLF concept

First Light Fusion is researching inertial confinement fusion (ICF) with a one-sided pressure drive. Targets containing fusion fuel are impacted by a high velocity projectile, launched by a two-stage light gas gun or a pulsed-power machine. Impact velocities and pressures are of order 10 km s^{-1} and 100 GPa, respectively. FLF have developed targets that amplify the input pressure to achieve conditions relevant for DD fusion. Target dynamics are modelled using the in-house hydrodynamics codes **B** and **Hytrac**. In simulations, the compression and heating of the fuel within the target results in a <1 ns pulse of thermonuclear fusion neutron emission. This work aims to validate the operating principles of the targets at low yields, using the modest input pressures currently available. In simulations, target yields are found to scale favourably with drive pressure. Target design details are confidential and are documented within an internal companion report.

B. Preliminary results from 2021

A DD fuel experiment performed in November 2021 (s0075) recorded scintillator hits on 6 detectors positioned approximately 1 m from the target. The temporal spread in the signals was 100 ns. The experimental scintillator data were referenced to the simulated fusion event time using an impact timing fiducial with ±100 ns accuracy. The observation of coincident scintillator hits at the expected time on a single shot prompted the design of a fusion validation campaign with multiple shots and an improved diagnostics suite. This includes a fusion event timing fiducial, multiple scintillator distances and a helium-3 detector array.

C. Fusion validation campaign description

The campaign aims to confirm the production of fusion neutrons from deuterium-fuelled target impact experiments. Experiments are focussed on a single class of fusion target driven by FLF's 38 mm bore two-stage light gas gun (the BFG). Detection and discrimination of neutrons in experiments provides evidence that fusion reactions occur within the target, thereby validating the performance of the target and design codes.

The campaign consists of a series of deuterium fuel and hydrogen fuel (null) experiments with notionally identical targets. The only design change in the target and experimental setup across these shots is the choice of fuel. The dominant remaining variables affecting target performance are the projectile velocity, planarity and integrity, which vary shot-to-shot. The neutron diagnostic suite consists of an array of fast scintillators and moderated helium-3 proportional counters. A detailed description of the experimental setup is given in Section III. The following hierarchy of evidence for the detection and discrimination of fusion neutrons was established and used to guide the experimental plan:

1. Record single shot coincidence hits on scintillators within the 'expected' event window.

2. Demonstrate repeatability of deuterium-fuelled shots.

3. Perform null shots with hydrogen fuel.

4. Measure particle time-of-flight to confirm consistency with 2.45 MeV neutrons.

5. Detect hits on an alternate detector with better discrimination for neutrons – a He-3 detector in this case.

The combination of items 1-3 above was the minimum objective for the validation campaign and might indicate that high energy particles were produced during an experiment. The pulsed nature of the experiment enables gating for the detection time of neutrons on the scintillators and their discrimination from random ionising background radiation (terrestrial, cosmic, etc.) by statistical arguments based on measured background rates (discussed in Section III D 2). Repeat shots demonstrate that the result was not an anomaly. Null shots are important for ruling out all spurious sources of detector signals including random background ionising radiation, visible radiation and mechanical vibration. Items 4 and 5 provide *direct* evidence for neutron production: time-of-flight measurements demonstrate that the emitted particle velocity is consistent with the velocity of a 2.45 MeV DD fusion neutron. Helium-3 detectors operate on an entirely different physical principle to scintillators and are relatively insensitive to particles other than neutrons. The case for the production of thermonuclear neutrons was built over the course of a ∼10 shot campaign. UKAEA have verified the experimental setup, modelled the detector responses and witnessed two experiments. They will review the full campaign dataset, analysis and interpretation of the results.

II. TARGET DESIGNS

Target design details are confidential and are documented within an internal companion report.

III.   EXPERIMENTAL

A.   Experimental setup

Experiments were performed on FLF's 38 mm bore two-stage light gas gun (the 'BFG'). The gun launches an 80 g tantalum-tipped projectile at ∼6.5 km s^{-1} into a DD-fuelled target mounted on the end of the gun barrel. A 40 mm stand-off between the barrel and the target impact face allows the projectile to be imaged in free flight by a fast framing camera (Shimadzu HPV-X2, 256 frames, 100 ns inter-frame) to determine its velocity and integrity before impact. Sensors embedded in the target monitor the impact time and fusion event time (see Section III B). A schematic of this system is shown in Figure 1.

The target is located within a 1.7 m diameter, 2.5 m long vacuum vessel (the experimental 'chamber'), which is evacuated to an ambient pressure of 1–10 mbar. Ballistic shielding protects the chamber from impact debris. A sectioned view of the experimental chamber showing the gun barrel, ballistic shielding and target location is shown in Figure 2.

Neutron detectors including scintillators and moderated He-3 proportional counters are installed on a framework surrounding the chamber, as shown in Figure 3. Scintillators are shown in blue and He-3 detectors are shown in yellow. To minimise vibrational coupling of the gun to the detectors, the framework has no direct contact with the chamber. The neutron diagnostic suite comprises the following (further details are given in Sections III D and III E):

- 16 large format EJ-200 plastic scintillators (1000 × 500 × 50 mm), each coupled to a 51 mm diameter ET-Enterprises 9266 PMT, assembled by Scionix.

- A small format EJ-200 plastic scintillator (200 × 100 × 40 mm) coupled to a 38 mm diameter Hamamatsu R9420 PMT, assembled by Scionix. This can be placed within the chamber in close proximity to the fusion target.

- 60 He-3 proportional counters (24" active length, 1" diameter, 5 bar pressure) packaged in 12 groups of 5. Each group is embedded in a 690 × 330 × 95 mm polyethylene moderator slab.

The positioning of scintillator detectors was a compromise between the overall sensitivity required for coincident detection (the primary goal) and multiple distances required for a n-TOF measurement (secondary goal). Nine large format scintillators were fielded on the core hexagonal framework approximately 1 m from the target. Four were located on the pitched framework 'roof' approximately 2 m from the target. Three were located in the orthogonal plane approximately 1.5 m from the target. On some shots, a single small format scintillator was placed inside the chamber approximately 10 cm from the source. This is destroyed by ballistic debris on each shot. Details of the work
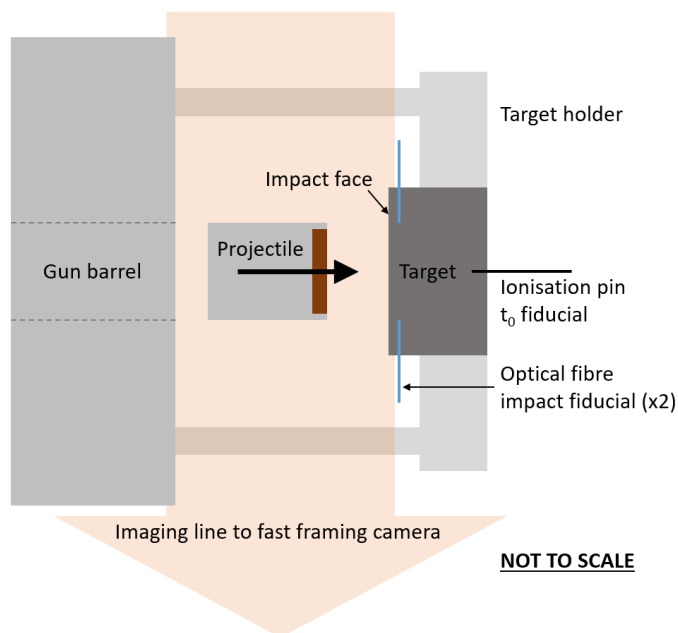

Figure 1.   Schematic of a fusion target and incident projectile, including the imaging field-of-view and the location of timing fiducials.
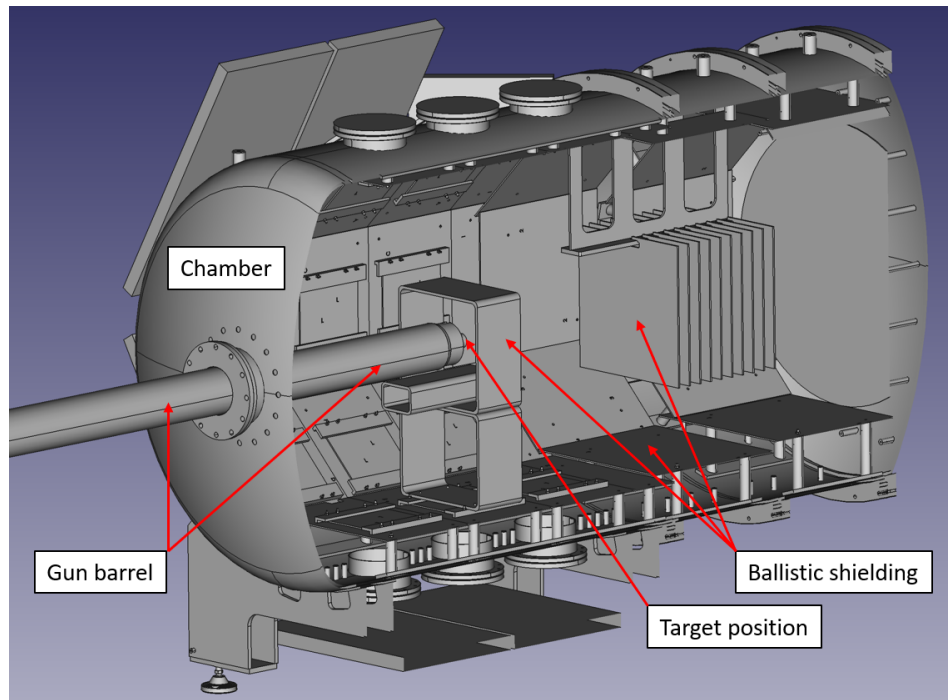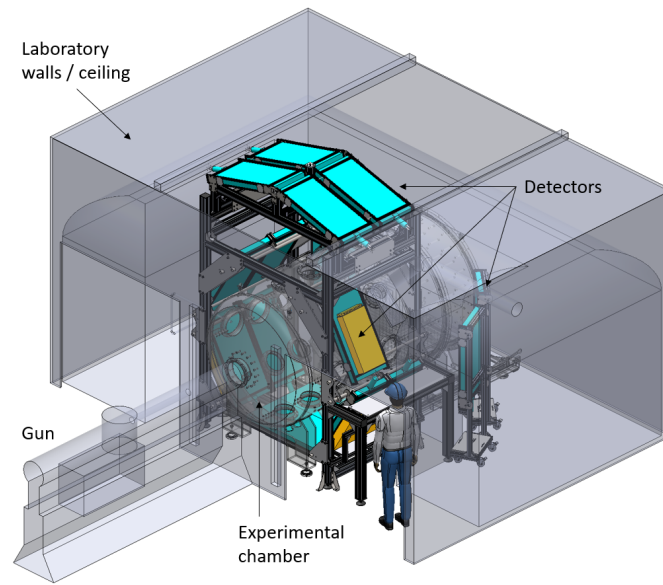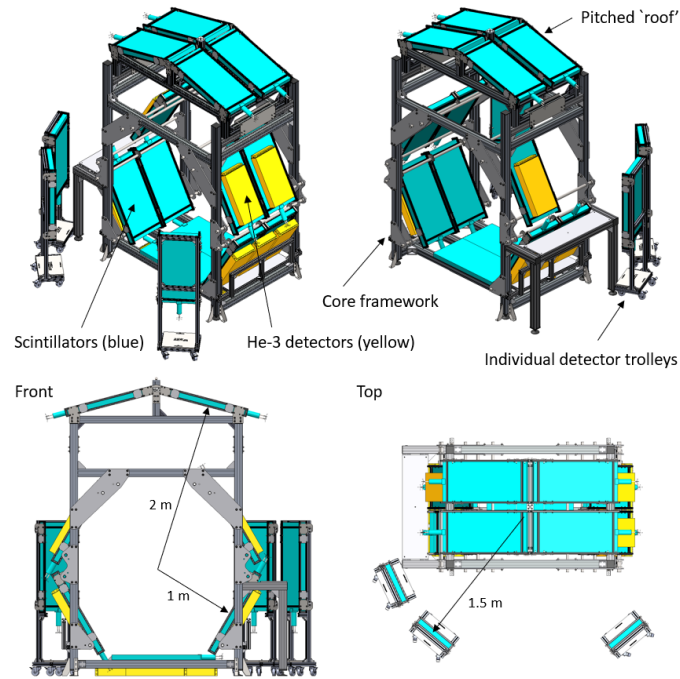
Figure 2. Sectioned CAD image of the experimental chamber, showing the gun barrel, ballistic shielding and target location. The gun barrel feeds into the chamber and the target is mounted on the end.

required to field a PMT inside the chamber are presented in Appendix F. Twelve He-3 detectors, each containing 5 proportional counter tubes, are mounted immediately behind the scintillators on the core hexagonal framework. The scintillator plastic acts to moderate the incident neutron field, which increases the sensitivity of the He-3 detectors. Maps of specific detector locations are given in Appendix D.

There are several mechanisms for the generation of bright optical emission within the experimental chamber which, if detected by a scintillator PMT, would increase the background count rate. Prior to installation on the framework, the integrity of the scintillator optical shielding was checked by scanning over all scintillator surfaces with a high power illumination source whilst monitoring the PMT output with a rate counter. During an experiment, the temporal profile of the ambient light level in the laboratory was monitored using an avalanche photodiode positioned close to a viewport on the chamber. This checks for any correlation between ambient light levels and 'hits' on the neutron detector array. A lack of correlation indicates the scintillators are optically light-tight. Null shots also confirm light tightness.

Laboratory
walls / ceiling

Detectors

Gun

Experimental
chamber

(a)

Pitched `roof'

Core framework

Scintillators (blue)   He-3 detectors (yellow)

Individual detector trolleys

Front   Top

2 m

1 m

1.5 m

(b)

Figure 3.   Upper: Experimental chamber located in laboratory. The gun enters from the bottom left. Scintillators (blue) and He-3 detectors (yellow) surround the chamber. Middle and lower: Detector framework and positions viewed from different angles.

B. Timing fiducials

Knowledge of the neutron emission time, t_0, is important for discrimination of signals from background radiation, stray optical light and mechanical vibration. This is of particular importance when the expected number of detections is low. If the event time is known accurately, then the short temporal duration ($\sim$0.1 ns) of the fusion event allows a narrow detector event time window to be determined. Additionally, knowledge of t_0 in principle enables a neutron time-of-flight (n-TOF) measurement to be made from a single target-to-scintillator distance. The targets include three timing fiducials: two situated close to the impact face and one close to the fusion location. These are shown schematically in Figure 1. Together, these fiducials bracket the fusion event time.

The target impact timing fiducials consist of optical fibres that are inserted radially into the target close to the impact face. Shock heating of the fibre optic causes the emission of light. This light propagates down the optical fibre and out of the chamber to an avalanche photodiode. From hydrodynamics simulations, the temporal offset from the fibre being shocked to bang time is approximately 1500 ns. t_0 can be predicted from the impact time to ±100 ns accuracy. Two impact fiducials are fielded to provide redundancy in the oscilloscope triggering scheme (see Section III G).

The dedicated t_0 fiducial consists of an ionisation pin with a sub-ns rise time which is embedded in the rear of the target. As the target shock front reaches the tip of the ionisation pin, the pin shorts and the bias voltage drops. A $100\,\mu$m thick Kapton layer prevents shorting of the pin by the base of the hole. A schematic of the probe is shown in Figure 4. From hydrodynamics simulations, the ionisation pin is shocked within $\Delta t = 20$ ns of the neutron emission time. Given the close proximity of the probe to the fusion event, the uncertainty in Δt for a fixed probe position in simulations is $-1.5/+0.75$ ns. The net Δt uncertainty is dominated by the exact probe position. The probe is located in a drill hole with a depth that is metrologised to $1\,\mu$m. The uncertainty in the probe depth is determined by the Kapton insulation thickness and the finite radius of the 'flat bottom' drill hole (r in the figure). The maximum bound on the probe depth is set by assuming there is no Kapton on the end of the probe, because it could become displaced during assembly. The minimum bound on the probe depth is set by assuming the probe 'bottoms out' on the top of a $50\,\mu$m radius at the bottom of the hole. From simulations, these limiting cases give a temporal uncertainty in the probe shock time of -8 / +5 ns.
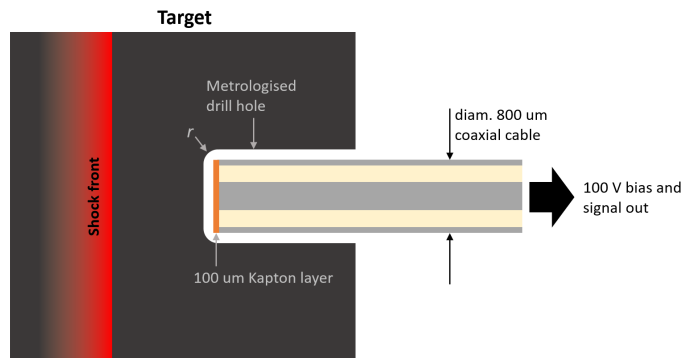

Figure 4. Schematic diagram of the ionisation pin (cleaved coaxial cable) neutron emission time (t_0) diagnostic. A shock in the target propagates toward the pin from the left. A Kapton layer prevents shorting of the pin by the base of the hole. A zoomed out image of the sensor location is shown in Figure 1.

C.   Neutron time-of-flight measurements

Neutron time-of-flight measurements are made using the t_0 timing fiducial and scintillators located approximately 0.1, 1, 1.5 and 2 m from the target. The large detector format and close proximity to the source introduces a non-negligible variation in the detector-source distance over the surface area of the scintillator. Table I lists the detector-source distances for all scintillators in their fielded locations. Maps of specific detector locations are given in Appendix D. The nominal distance is defined from the source to the centre of the scintillator cuboid. Shortest and longest distances to any point within each detector are also given. The TOF values for 2.45 MeV neutrons (46.2 ns/metre of flight) are calculated assuming a direct line from the source to the detector slab. There is resolvable worst-case difference in time of flight between detectors at each location, despite the n-TOF range in any given detector (see final column) . Note that the response time of the detectors themselves is of order 5 ns.

Detector ID	Location	Nominal distance (mm)	Nominal n-TOF (ns)	Shortest distance (mm)	Shortest n-TOF (ns)	Longest distance (mm)	Longest n-TOF (ns)	Max. n-TOF range (ns)
Small 1	In chamber	165	7.6	145	6.7	210	9.7	3.0
Large 1	Core (a)	1087	50.2	999	46.2	1320	61.0	14.8
Large 2	Core (a)	1087	50.2	999	46.2	1320	61.0	14.8
Large 3	Core (a)	1087	50.2	999	46.2	1320	61.0	14.8
Large 4	Core (a)	1087	50.2	999	46.2	1320	61.0	14.8
Large 5	Core (a)	1087	50.2	999	46.2	1320	61.0	14.8
Large 6	Core (b)	1027	47.4	996	46.0	1223	56.5	10.5
Large 7	Core (b)	1027	47.4	996	46.0	1223	56.5	10.5
Large 8	Core (b)	1027	47.4	996	46.0	1223	56.5	10.5
Large 9	Core (b)	1027	47.4	996	46.0	1223	56.5	10.5
Large 10	Roof (a)	2001	92.4	1933	89.3	2160	99.8	10.5
Large 11	Roof (a)	2001	92.4	1933	89.3	2160	99.8	10.5
Large 12	Roof (b)	1955	90.3	1926	89.0	2081	96.1	7.1
Large 13	Roof (b)	1955	90.3	1926	89.0	2081	96.1	7.1
Large 14	Perimeter	1548	71.5	1520	70.2	1674	77.3	7.1
Large 15	Perimeter	1548	71.5	1520	70.2	1674	77.3	7.1
Large 16	Perimeter	1548	71.5	1520	70.2	1674	77.3	7.1

Table I. Detector locations and n-TOF ranges.

The geometrically calculated n-TOF ranges in the table are in good agreement with temporal responses predicted by MCNP calculations performed by UKAEA, shown in Figure 5. The geometry and material assignment of the MCNP model are presented in Appendix G. Scintillator hits will also be produced by scattered neutrons that appear later than predicted by the direct n-TOF numbers in Table I. This effect is evident in the relatively long decay times of the scintillator responses in Figure 5. It is also possible for neutrons to interact with metal hardware *between* the source and scintillator, generating gamma rays that propagate ahead of the neutron field and produce early scintillator hits, as highlighted in Figure 5. The MCNP modelling can assess the likelihood and potential impact of neutron scatter and gamma production on interpretation of the experimental data.
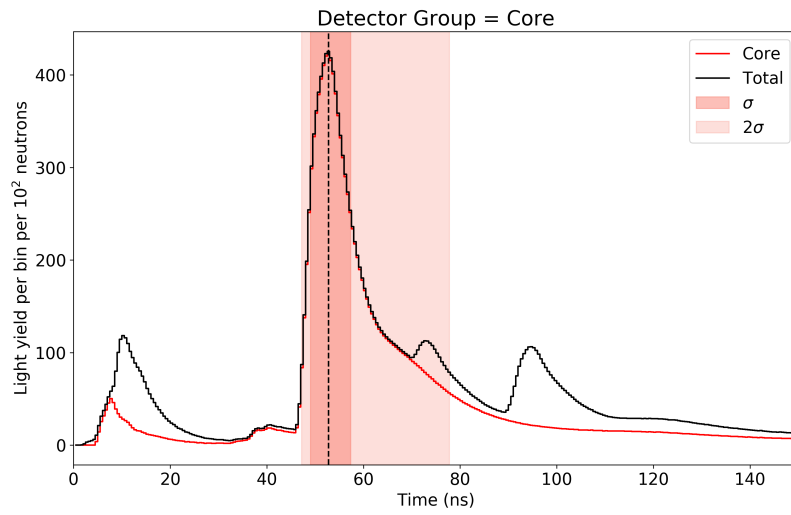
Figure 5. Response of the scintillator detectors over time as modelled by UKAEA using the code MCNP with our detector geometry. The black line shows the total response summed over all our detectors. The red line shows the contribution from all the detectors at one metre distance from the target. The temporal spread for a set detector distance arise from three main causes: the large detector size; slow down of neutrons as they scatter in metal shielding on the way to the detector and also a small component of secondary gammas resulting from the scattering which arrive early.

D. Scintillator description and characterisation

The scintillating medium of the large and small format detectors is a monolithic slab of EJ-200, an anthracene-doped polyvinyltoluene (PVT) manufactured by Eljen Technology. The scintillation efficiency is 10,000 photons/MeV electron, with an emitted photon peak energy at 425 nm and a 3.8 m optical attenuation length. The PMTs are located on the ends of the scintillator slabs, as shown in Figure 6. The scintillators are wrapped in a reflective medium to increase the scintillation photon collection efficiency of the PMT photocathode. An opaque outer covering prevents ambient optical light from reaching the photocathode. Detectors are operated with a negative bias as recommended by the manufacturer, Scionix. The bias is set at the maximum specified value of 1500 V, to maximise the detection sensitivity.
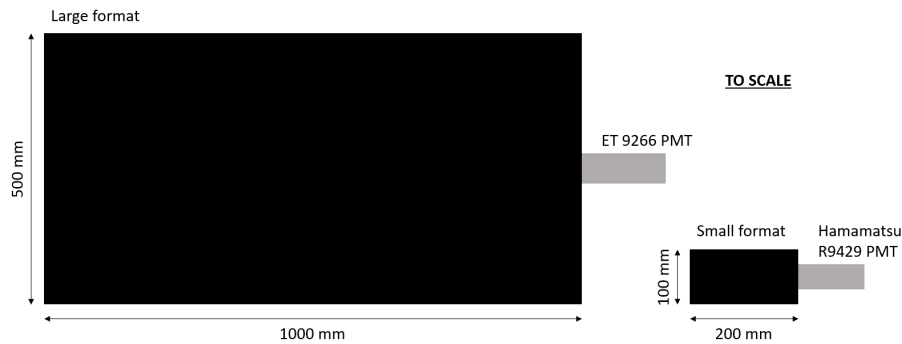
Figure 6. Dimensions of the large and small format scintillator detectors.

The cross section for the elastic scattering of DD neutrons (2.45 MeV) by protons and carbon atoms is 2.6 and 1.6 barns, respectively, and the elastic cross section dominates in this energy region. Using the following 1D equation for the scattering efficiency from reference [1]:

$$\eta = \frac{N_H \sigma H}{N_H \sigma_H + N_C \sigma_C} \{1 - \exp[-(N_H \sigma_H + N_C \sigma_C)d]\}, \tag{1}$$

DD neutrons have a $\sim 42\%$ probability of creating hydrogen or carbon recoils when propagating through a 5 cm slab of EJ-200. This value is in good agreement with the intrinsic detector efficiency of 0.527 calculated by UKAEA using MCNP (TechD-19-070). It is important to note that the light yield decreases with energy of the recoil atoms and the efficiency of optical transport is not included in these simple calculations. The discrimination level of the detection system, which is related to the photocathode quantum efficiency and PMT gain, will also further reduce the net efficiency.

The response of the coupled scintillator/PMT detectors to neutrons and gammas was studied in-house using a Cs-137 isotope source ($E_\gamma = 661$ keV) and a dense plasma focus neutron source ($E_n = 2.45$ MeV). Compton edge recoil electrons from Cs-137 ($E_e = 476$ keV) produce a similar scintillation light yield to a 2.45 MeV recoil proton from a DD neutron scattering event ($\sim$5000 photons). This makes the Cs-137 gamma source a useful proxy for DD neutrons. This work is described in detail in a separate report (WP2). The detector efficiencies were also calibrated for 2.5 MeV neutrons at the National Physical Laboratories (NPL) Van der Graaf neutron source.

1. Efficiency

The absolute 2.5 MeV neutron detection efficiency of a small and large detector was determined at the NPL Van der Graaf neutron source. The efficiencies, correcting for background, room scatter and acquisition live time are shown in Table II. A 2 µs detector dead time and 20 mV lower discrimination signal threshold were used.

2. Background rate

Figure 7 shows the background recorded in the FLF ground level laboratory using one of the large scintillation detectors, along with the Cs-137 calibration spectrum (no background subtraction) and dark counts of the PMT. The Cs-137 gamma response can be seen on MCA channels below 1200. The dark count spectrum was obtained

Scintillator detector	Efficiency
Small	$(42.4 \pm 6)\%$
Large	$(30.7 \pm 6)\%$

Table II. Absolute efficiency of a small and large scintillator for 2.5 MeV neutron detection, accounting for background, room scatter and acquisition live time. A $2\,\mu s$ detector dead time and 20 mV lower discrimination signal threshold were used. Measurements performed at NPL.

with the PMT removed from the scintillator and placed in a light-tight enclosure. Acquisitions were obtained over approximately 12 hours. The data are normalized to the MCA live time. The measured background rate during the acquisition was a few kHz.
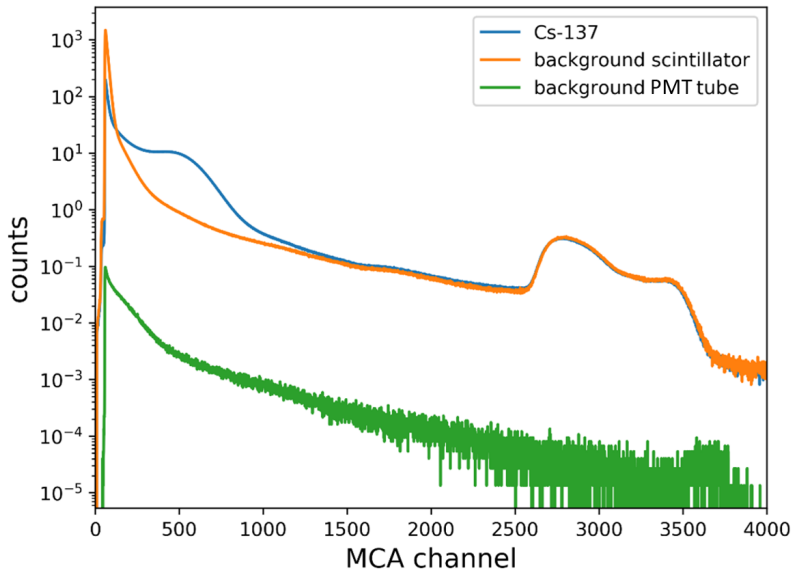
Figure 7. Pulse size distribution of large scintillation detector collected using the MCA card. Background (orange), Cs-137 gamma spectrum without background subtraction (blue) and background with the PMT decoupled from the scintillator (green).

The average background count rate of the full large scintillator array was measured with the detectors installed as fielded on gun experiments. 2 ms of raw PMT data were recorded for each detector. Pulses were counted after applying a pulse shape discrimination (PSD) routine to avoid double counting due to delayed fluorescence peaks. This process yielded an average background rate per detector of 2.5 kHz, in agreement with the 12 hour MCA acquisition on a single detector. Assuming independent events, we can expect a background rate of 16×2.5 kHz = 40 kHz across the full array of 16 large detectors. Within an event time window of 400 ns, we therefore have a probability for recording a background hit of 1.6×10^{-2}. From Poisson statistics, the probability for coincident detection of two or more background hits within the same 400 ns window from independent events (i.e. not a multiplicity event such as spallation), is approximately 1.3×10^{-4}. The rate of background multiplicity events needs to be investigated over a long time period to understand random fluctuations and accurately measure the value. For the purposes of the background analysis in this report we take a very conservative approach and assume that if at least one background hit is recorded in a shot (with a probability of 1.6×10^{-2}) then we assume a worst case multiplicity type event and treat all the other hits in that shot as background. This is discussed further in Section IV D.

E. Helium-3 detector description and characterisation

Helium-3 proportional counters are an alternate detector type based on the ^{3}He(n,p) reaction. The advantage of these detectors is that they are relatively insensitive to other types of radiation. The main disadvantage is that the neutron field must be moderated for the cross section to be sufficiently high and dominant over other possible interactions. This means that temporal information about the source of radiation is not recoverable.

The 12 He-3 detector units comprise sets of 5 He-3 tubes (24" active length, 1" diameter, 5 bar pressure) embedded in polyethylene moderator slabs. A drawing of the moderator housings is shown in Figure 8. During gun experiments, each unit is oriented with the thin side of the housing (identified in the figure) facing the target. Units are located immediately behind large format scintillators to moderate the incident neutron field. The detector sensitivity is dependent on the moderator design. This has been investigated by UKAEA using MCNP and measured experimentally (see Section III E 1 below). The temporal window over which to expect hits from a prompt source is also dependent on the moderator design. From private communications with AWE, 300 µs is appropriate. This is in agreement with results from MCNP calculations performed by UKAEA, as shown in Figure 9.
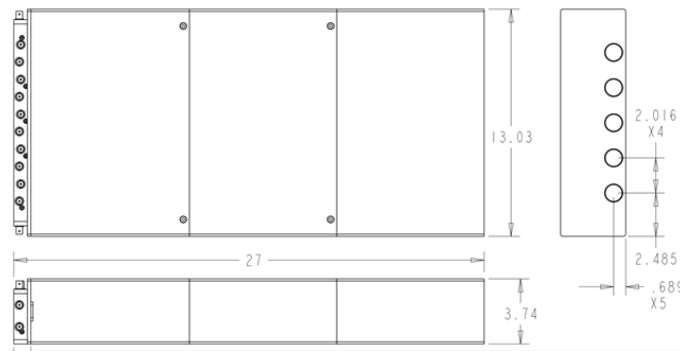
Figure 8. Schematic of He-3 detector slab. Dimensions in inches. He-3 tubes located within the five 1" circles.
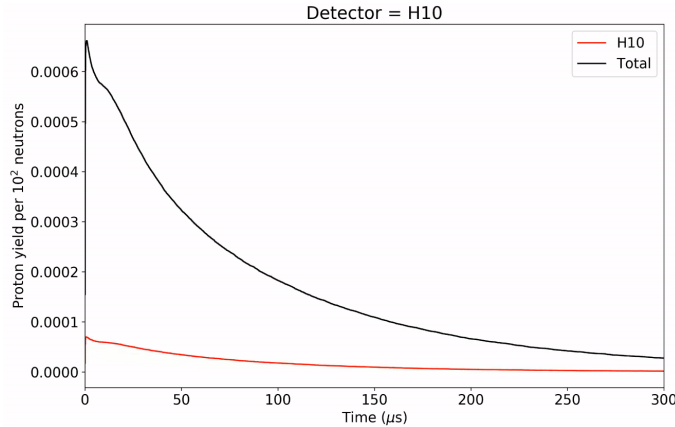

Figure 9. Temporal response of the He-3 array to a prompt DD neutron source, according to MCNP calculations performed by UKAEA. The combined array response is shown in black. The response of detector 10 is shown in red. Individual detector responses vary by ±40%. Figure credit: S. Bradnam, UKAEA.

The He-3 high voltage bias is of order 1 kV and generated on board. Discrimination and analogue-TTL conversion electronics are also housed on board each unit. The detectors have the option to monitor analogue tube signals or 100 ns TTL pulses for each signal. A low voltage discriminator removes noise and gammas before analogue-TTL pulse conversion. The TTL pulses can be summed on board each detector (5 tubes per detector), reducing the number of acquisition channels required from 60 to 12. On gun experiments, the combined TTL outputs were monitored.

The analogue response of the He-3 tubes to moderated 2.45 MeV neutrons has not yet been recorded. Qualitatively, the response shown in Figure 10 is expected (modified from Figure 14.5 in reference [1]). The position of a low voltage discrimination threshold for rejecting gammas and noise is marked.
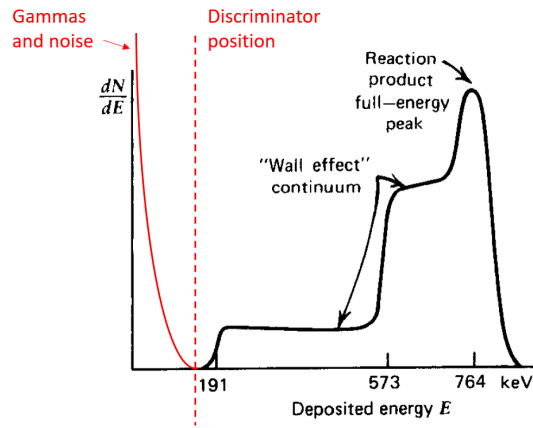
Figure 10. Typical pulse height spectrum from a He-3 proportional counter. Modified (red) from the original Figure 14.5 in reference [1].

1. Efficiency

The absolute 2.5 MeV neutron detection efficiency of a He-3 detector was determined at the NPL Van der Graaf neutron source. Pulses from the combined TTL output were monitored. Measurements were performed with a large format scintillator positioned immediately in front of the He-3 detector, as is the case when fielding on gun experiments. Using a solid angle defined by the area of the polyethylene housing, the net efficiency was found to be $(11.9 \pm 0.4)\%$.

2. Background rate

The analogue background spectrum of a single He-3 tube (detector 8, tube 2) was recorded with the detector in it's fielded location on the gun, see Figure 11. This was recorded over 12 hours with an MCA. The peak at the left hand side is caused by background gammas and noise. The background neutron spectrum is too low frequency to register over the acquisition time of the run.
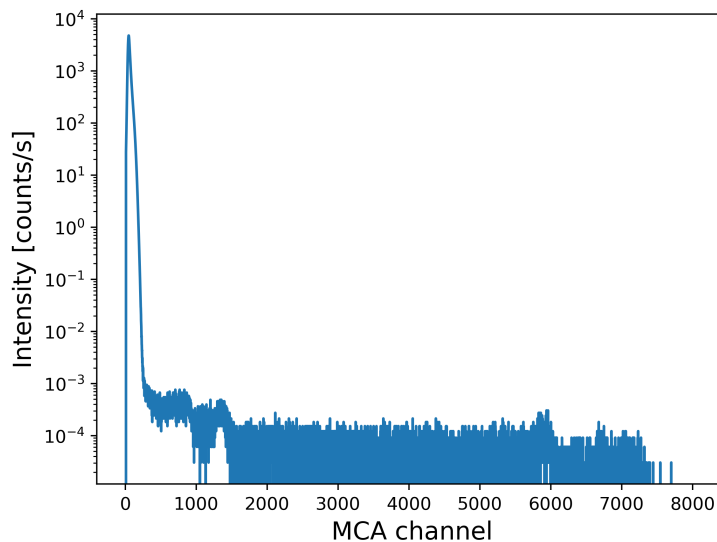
Figure 11. Analogue background spectrum from a single He-3 tube (#2) within He-3 detector 8. ∼12 hour acquisition. Spectrum normalised to the acquisition live time.

The low level discriminator before the TTL output rejects the background counts within the main peak in Figure 11 (private communication with AWE). The residual background rate after discrimination was monitored using the combined TTL output of a single unit (detector 8). 811 pulses were counted in 587.6 s, giving a rate of 1.38 Hz. The combined background rate over the full He-3 array was estimated at $12 \times 1.38 = 16.6$ Hz. Within our specified $300\,\mu s$ detection window, the probability of a background hit is 0.005.

F. Overall detection efficiency and threshold

From the detector geometries on the gun, we can estimate the overall detection efficiency of the system using the following expression:

$$P = \frac{\Omega}{4\pi}\epsilon, \tag{2}$$

where Ω is the solid angle occupied by the detectors and ϵ is the net detection efficiency. Note that the effect of absorption and scattering of neutrons by hardware (shielding, chamber, etc.) is not accounted for in this simple equation.

The solid angles subtended by a large scintillator at 1.0, 1.5 and 2.0 m from the source are 0.435 sR (3.46%), 0.208 sR (1.65%) and 0.120 sR (0.95%), respectively. For 9 detectors at 1 m, the total solid angle covered is 3.9 sR (31%). Using the experimentally determined detector efficiency of 0.307 we find $P = 0.095$. For 3 detectors at 1.5 m, $P = 0.015$ and for 4 detectors at 2.0 m, $P = 0.012$. The He-3 array subtends a solid angle of 2.22 sR (17.7%). Using the experimentally determined detector efficiency of 0.119 we find $P = 0.021$. We can use the negative binomial probability distribution to determine the probability for detection of different numbers of neutrons with different certainty levels. The required yields for at least 1 and 2 detections on the 1 m scintillator and He-3 arrays at 65% and 90% certainty are presented in Table III.

	65% certainty	90% certainty
Large scintillators		
1 detection	11	23
2 detections	23	40
He-3 detectors		
1 detection	50	109
2 detections	105	184

Table III. Yields required for the detection of at least one or two neutrons on the 1 m scintillator and He-3 arrays with 65% and 90% certainty.

G. Data acquisition and analysis

The three target timing fiducials, seventeen analogue PMT outputs and the ambient light monitor are recorded directly onto three, eight-channel 350/500 MHz LeCroy oscilloscopes with no prior amplification, filtering, discrimination or gating electronics processes. The recording window of every channel is 200 µs (note that the expected neutron arrival time window is several hundred ns, which allows for background levels to be recorded during the shot and longer timescale processes (e.g. ambient light levels) to be monitored. The raw PMT data is interrogated for pulses by eye, without any pre-applied discrimination algorithms. The combined TTL signals from each He-3 detector are recorded onto four, four-channel, 250 MHz LeCroy oscilloscopes. Every channel records 5 ms of data to assess background levels. A 300 µs window from t_0 onwards is interrogated for TTL pulses.

A diagram of the oscilloscope triggering and synchronisation scheme is shown in Figure 12. The first oscilloscope (the 'trigger' scope) is triggered by one of three target timing fiducials for redundancy using the oscilloscope internal OR gate functionality. The auxiliary output of the first oscilloscope is distributed using identical cable lengths (not represented by arrow lengths in the figure) to trigger the remaining 6 oscilloscopes. This signal is monitored on all 7 oscilloscopes, enabling synchronisation to within 1 ns.

To measure the time-of-flight of neutrons detected on scintillators, the neutron emission time, t_0, must be accurately measured and relative diagnostic delays must be taken into account. Each diagnostic has a relative delay associated with internal operation and connecting cable/fibre propagation time. These delays can be found in Appendix E. A 30 m run of identical, 50 Ω, LBC240 Extraflex coaxial cables from Gigatronix (transit time $\sim$150 ns) connects the diagnostics around the experimental chamber to the oscilloscopes housed in a separate enclosure. This common cable run has no impact on timing analysis. The neutron emission time is monitored by the ionisation pin placed behind the target, as described in Section III B. Diagnostic delays and trigger synchronisation offsets are applied to the raw oscilloscope data before it is all referenced to t_0 using the ionisation pin pulse. The ionisation pin sends a signal within time $t_{0\mathrm{IP}}$ of the fusion event. This variable, $t_{0\mathrm{IP}}$, changes between shots due to the absolute positioning of the pin in target manufacture. The value of $t_{0\mathrm{IP}}$ is determined from metrology of the pin position combined with simulations. The value used for each shot can be found in Appendix E.
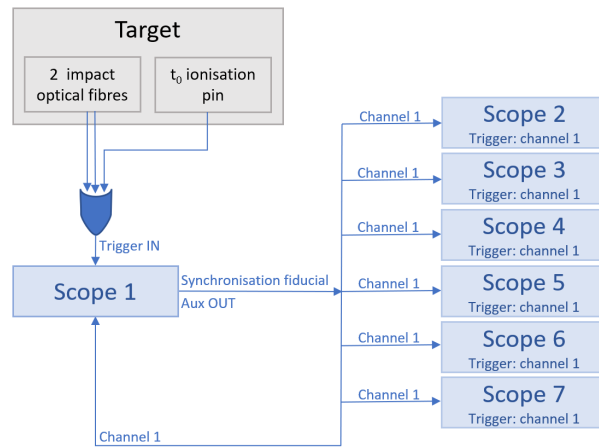
Figure 12. Diagram of the triggering and synchronisation scheme for the 7 oscilloscopes used in these experiments. The first scope (the trigger scope) is triggered by the rising edge of an impact or t_0 diagnostic. The auxiliary OUT is monitored on scope 1 and distributed to all other scopes for triggering and synchronisation. The synchronisation pulse cable lengths are identical (not represented by the arrow length in the figure). Oscilloscopes 1-3 monitor the PMTs. Oscilloscopes 4-7 monitor the He-3 detectors.

When plotting the data, the following process is used, based on the timeline of trigger events shown in Figure 13. This process aligns all data from all scopes with the same zero time point (the fusion event time):

1. The trigger scope automatically records two measurements:

    - The time from the trigger scope triggering to the time synchronisation fiducial reaching 20 mV, t_{fid}.
    - The time from the trigger scope triggering to the ionisation pin reaching 0.5 V, t_{ion}.

2. Calculate t_0 as seen by the trigger scope: $t_{0,\,\text{trigger}} = t_{\text{ion}} - t_{\text{ion delay}} - t_{0\text{IP}}$. Here, $t_{\text{ion delay}}$ is the cable transit time from the ionisation pin to the scope and $t_{0\text{IP}}$ is the temporal offset from the fusion event to the ionisation pin being shocked. The value for $t_{0,\,\text{trigger}}$ is subtracted from all channels of the trigger scope, thus setting t_0, the fusion event time, at zero.

3. Calculate t_0 as seen by all other scopes: $t_{0,\,\text{other}} = t_{\text{ion}} - t_{\text{ion\_delay}} - t_{\text{fid}} - t_{0\text{IP}}$. This value, $t_{0,other}$ is subtracted from all channels of these scopes, thus setting t_0, the fusion event time, at zero.

4. When loading data from any channel of any scope, the relevant delay is immediately subtracted: ($t_{0,\,\text{trigger}}$ if it is the trigger scope and $t_{0,\,\text{other}}$ if any other scope). The delay for the specific diagnostic on that channel is also subtracted from the time data. For example, from Appendix E, if the diagnostic is a large PMT the delay applied is 190 ns.
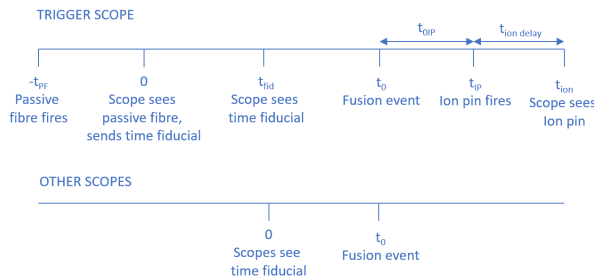
Figure 13. Timeline of the trigger event, captured by the first scope, and the subsequent synchronising timing fiducial sent by the trigger scope and received by all scopes.

H.   Potential sources of spurious signals on neutron detectors

Potential sources of spurious signals on detectors are listed and briefly addressed below:

1. Background ionising radiation: It is statistically unlikely that a background hit will occur within the time gated measurement window. The background count rate was measured at 40 kHz on the full large scintillator array and 12 Hz on the full He-3 detector array. Within a time gated neutron measurement window of 100 ns and 300 µs for scintillator and He-3 detectors, respectively, the probability of observing a single background hit is 4×10^{-3} for both detector types. Repeat fuel shots and hydrogen null shots will be performed to strengthen the case against random background radiation.

2. Stray optical light: Light-tight scintillator integrity is checked offline using a bright illumination source and a rate metre. Test shots are performed before fusion shots to look for increases in hits over the normal background. Time-varying ambient room light levels are recorded during a shot. This allows us to look for correlation in the ambient optical light levels and hits on the detectors. The brightest emission occurs 10–100 microseconds after the fusion event, as the hydrogen gun propellant releases into the experimental chamber, and not during target impact. Hydrogen null shots will also address this issue.

3. Mechanical vibration: The scintillators and He-3 detectors are mounted on a dedicated framework that is not directly coupled to the experimental chamber. Test shots are performed before fusion shots to look for increases in hits over the normal background. Null shots also address this issue.

4. EM noise / generator radiation: Not present on a gas gun experiment driven by explosives.

5. Target ionising radiation: Simulated target temperatures are of order 100s of electronvolts. Therefore, we do not expect significant emission of photons with energies above several keV. Such low energy photons cannot penetrate the target or vacuum vessel to be detected by the scintillators. Hydrogen null shots can strengthen the case against the detection of target x-rays because they will produce similar x-ray fields to DD fuel shots. The target is driven in a purely hydrodynamic manner (no applied electromagnetic fields). Therefore, any beam-target mechanism yielding fusion would have to be driven by self-generated magnetic field.

6. High energy particles from nuclear interactions. MCNP calculations from UKAEA inform the production rate of secondary high energy particles from fusion neutron scattering. The probability of these events should be considered when interpreting the experimental data. Without extraneous sources, the only production mechanisms for gammas are a consequence of neutron production in the target.

IV.   RESULTS

A.   Results summary

A summary of the 21 gun experiments performed during the fusion validation campaign is presented in Table IV. These included 12 base case DD target shots, 1 DD design variant shot, 4 H_2 null shots and 4 test shots. Test shots were required to increase the projectile velocity and reliability by tuning the gun parameters. Nine of the base case DD shots had no known issues, although the projectile velocity varied across these from $6.2 - 6.7 \pm 0.2$ km s^{-1}. These 9 shots are highlighted in green in Table IV and will be referred to as 'operational'. The number of scintillator and He-3 detector hits recorded during each experiment is listed. Scintillator hits are counted in a 400 ns window from the fusion event time, t_0. This window is appropriate given n-TOF and scattering considerations discussed later. He-3 hits are counted in a 300 µs window from t_0. A full dataset is provided in the appendix.

Shot	Description	Projectile velocity [km/s]	Scintillator hits*	He-3 hits[†]	Notes
0086	DD	6.4	2 [1,3]	0	Only 3 He-3 fielded
0087	DD	6.3	3 [1,8,9]	2 [1,5]	Only 5 He-3 fielded
0088	H_2 null	6.2	0	0	Only 5 He-3 fielded
0089	H_2 null	6.3	0	0	
0090	DD	6.5	1 [4]	0	In-chamber PMT fielded
0091	DD	6.3	3 [9,11,15]	0	In-chamber PMT fielded
0092	DD	5.9	0	0	Projectile failure
0093	Test shot*	n/a	0	0	No projectile imaging
0094	DD variant[‡]	6.7	0	0	
0095	DD	6.2	0	0	
0096	Test shot	6.6	0	0	
0097	Test shot	6.6	n/a	n/a	Detectors not on
0098	Test shot	6.4	0	0	
0099	DD	6.5	0	0	Mechanical target failure
0100	DD	6.4	2 [5,15]	0	
0101	DD	6.8	0	0	Mechanical target failure
0102	DD	6.7	9 [1,4,5,6,8,9,12,15,16]	1 [11]	
0103	DD	6.7	6 [2,6,7,8,9,16]	1 [5]	
0104	DD	6.7	3 [s,1,16]	1 [4]	In-chamber PMT fielded
0115	H_2 null	6.6	0	0	
0116	H_2 null	6.5	0	0	

Table IV. Shot log for the DD fusion validation campaign. Projectile velocities are ± 0.2 km s^{-1}. *Performed to tune the gun parameters. Test shots have inert plastic block targets and no DD fuel. [‡] A DD target design variant, previously untested. *Scintillator hits recorded in a 400 ns time window after neutron emission time. Number of hits is followed by the detector IDs in square brackets. [†] He-3 hits recorded in a 300 us time window after neutron emission time. Number of hits is followed by the detector IDs in square brackets. 12 He-3 detectors were fielded from shot s0089 onward. Detector locations are given in Appendix D. 'Operational' base case shots are highlighted in green.

Over the 9 operational DD shots, 29 scintillator hits and 5 He-3 hits were recorded within the anticipated time windows. Scintillator hits were distributed over 8 shots and He-3 hits were distributed over 4 shots. This demonstrates repeatability in the operation of the target. Multiple scintillator hits were recorded on 7 shots. Multiple He-3 hits were recorded on 1 shot. Random ionising background radiation is expected to contribute negligible hits to the tallies from both detector types (see Section IV D). Measurements of the temporal profile of the ambient optical intensity in the laboratory show that the room is brightest ∼100 µs after the target is compressed. The scintillator PMTs do not respond to the increase in ambient light, demonstrating that they are optically light tight throughout. Null shots resulted in no detections. A statistical analysis of the null shots is presented in Section IV E.

Scintillator hits were recorded at multiple distances from the target. The time-integrated, shot-aggregated scintillator hits at each gross detector location (1 m, 1.5 m and 2 m) are compared to the solid angle coverage of each detector grouping in Figure 14. The detected counts follow the drop with detector solid angle. This relationship is consistent with detection of particles that were produced at the target location, and not with spurious sources such as mechanical vibration, ambient room light or background ionising radiation.

A basic analysis, shown in Figure 15, suggests that the hits are randomly distributed among the detectors at 1 m and 2 m around the radial plane. However, the yield was too low to field detectors on the gun axis such that a full isotropy analysis could take place; this will be completed as yields increase with new higher performance targets.

Observations of scintillator hits at multiple distances allowed for a time-of-flight analysis to discern the energy/mass
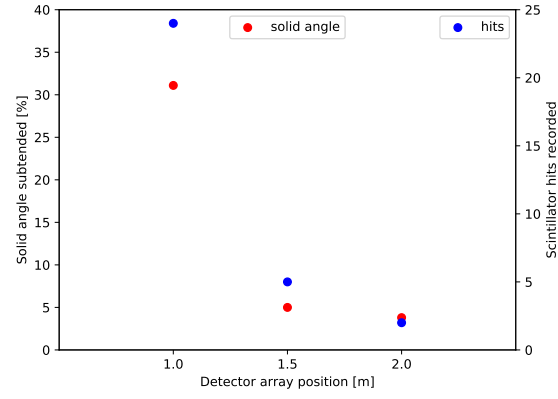
Figure 14. Comparison of solid angle coverage by each scintillator detector group and total hits recorded by each group. Solid angle represented as a percentage of 4π coverage.
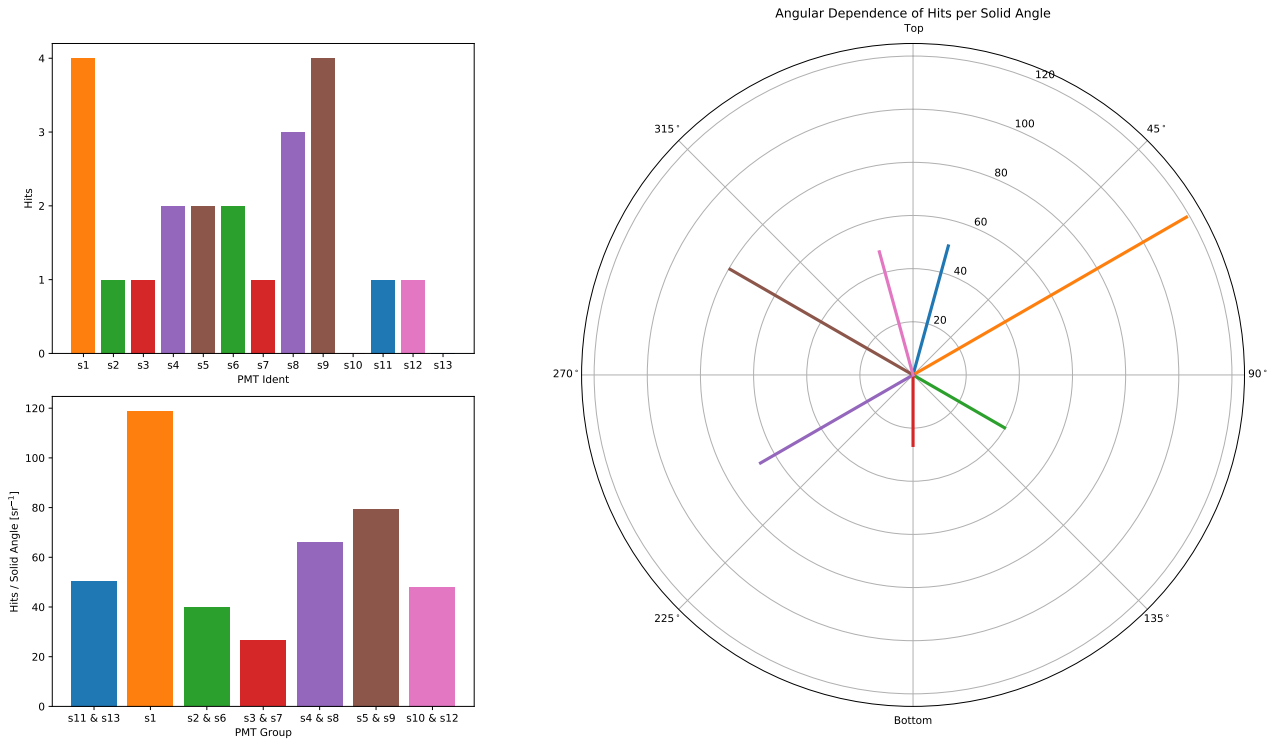

Figure 15. Plot illustrating the angular distribution of neutron emission. The upper left pane shows the total number of counts on each radial scintillator. The lower left pane groups the detectors by angular and radial position. The number of hits is summed over the detectors in the group then divided by their combined solid angle to allow comparison. The right hand pane represents this normalised data on polar axes where the angle of the line corresponds to the position of the detector group around the vacuum chamber and the length of the line is the number of detections normalised by detector group solid angle.

ratio of the particles responsible. These results are discussed in Section IV B. On multiple shots, time-of-flight data were recorded that is consistent with the propagation of 2.45 MeV DD fusion neutrons. The observation of a hit on a small scintillator detector positioned close to the target validated the operation of the fusion event (t_0) timing fiducial inserted into each target. The t_0 diagnostic allowed time referencing of all the experimental data and provided an additional point (at $x = 0$) for assessing particle time-of-flight.

A positive correlation between the target neutron yield and the projectile impact velocity is observed. This is expected because the impact pressure is a strong function of the impact velocity and the targets work by amplifying the initial impact pressure to reach conditions in the fuel that are relevant for DD fusion. The projectile velocity is variable shot-to-shot and this could affect the target performance. Scatter plots of the number of scintillator hits

against measured projectile velocity are shown in Figure 16. Data are split into detections on the 1 m, 1.5 m and 2 m scintillator groups. It is useful to plot linear regression lines to visualise any correlation in the data. The regression lines are not an attempt to model the velocity dependence of the yield. Evidently there is a lot of scatter in the data. However, no neutrons were detected at 5.9 km s^{-1} (s0092) or 6.2 km s^{-1} (s0095), which may indicate the yield drops below the detection threshold at these velocities. We note that in shot s0092, there was also evidence of the projectile breaking up before impact, which would further degrade target performance. Three of the four null shots were at least 6.3 km s^{-1} and would have seen signal using this velocity correlation if they had been deuterium instead of hydrogen fuel - meaning they were effective null shots.
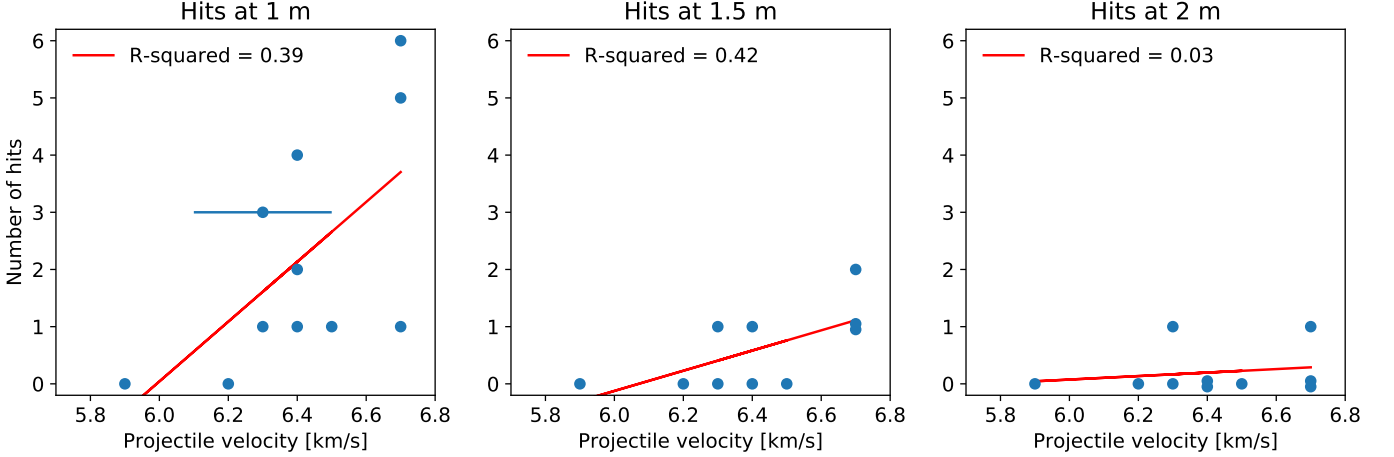
Figure 16. Scatter plots of number of scintillator hits against measured projectile velocity. Data are split into detections on the 1 m, 1.5 m and 2 m scintillator groups. Linear regression lines are plotted in red. ± 0.2 km s^{-1} velocity error bar is shown on one data point.

The Spearman rank correlation coefficient was calculated as an alternative test for correlation in the velocity versus hits data. The coefficient returns values between +1 and -1, with 0 implying no correlation. Correlations of +1 and -1 imply exact positive and negative correlation, respectively. Spearman coefficients for the datasets in Figure 16 are presented in Table V. For the 1 m and 1.5 m detector groups, the calculations suggest a positive correlation in the number of detector hits versus the projectile velocity. This is another indication that the scintillator hits occur as a result of target dynamics. Also shown are corresponding probabilities for the null hypothesis of no correlation, i.e., the probability that the observed correlation would be found in a randomly distributed dataset.

Detector group	Spearman coefficient	P-value
1 m	0.6310	0.0374
1.5 m	0.6212	0.0552
2 m	0.0965	0.7909

Table V. Spearman rank correlation coefficients for number of scintillator hits versus projectile velocity. Values between 0 and 1 indicate positive correlation. P-values give the probability for the null hypothesis of no correlation. Data are split into detector groups at 1 m, 1.5 m and 2 m (see Figure 16).

The variation in projectile velocity (± 0.5 km s^{-1}) observed in this project is typical for FLF's 38 mm bore gas gun and agrees with data collected since commissioning. This is also in line with performance from other gas guns found in literature. Two stage gas guns are subject to many input variables leading to changes in performance. The likely main variables causing spread in projectile velocity are: room temperature variation, barrel wear and smokeless powder burn consistency.

B. Neutron time-of-flight results

Aggregated n-TOF results from 8 DD experiments are presented on an $(x - t)$ plot in Figure 17. These experiments all produced scintillator hits within 400 ns of t_0 (as measured by the ionisation pin), with the expected negligible background rate outside of this window. The choice of time window is somewhat arbitrary and was chosen to include the data recorded at 2 m. This broader time window allows for inclusion of a larger number of scattered neutrons within the plot. It also increases the likelihood that background radiation contributes to the dataset. From the statistical analysis presented in Section IV D, we expect not more than one of these data points to be produced by background.

Horizontal dashed lines on the plot depict the distances of scintillator groups as measured from the neutron source location to the centre of the scintillator volumes (see Table I). The diagonal dashed grey line is the path drawn by a 2.45 MeV DD neutron ($v = 2.17 \times 10^7$ m s^{-1}) produced at $t = 0$. The diagonal dashed yellow line is the path drawn by a photon (moving at c) produced at $t = 0$. Coloured markers indicate the time of scintillator hits for different shots. The time of a hit was defined as the time of the first peak in the corresponding oscilloscope trace. This process is discussed further in Section IV F. Data points have been referenced to t_0 on a shot-by-shot basis using the ionisation
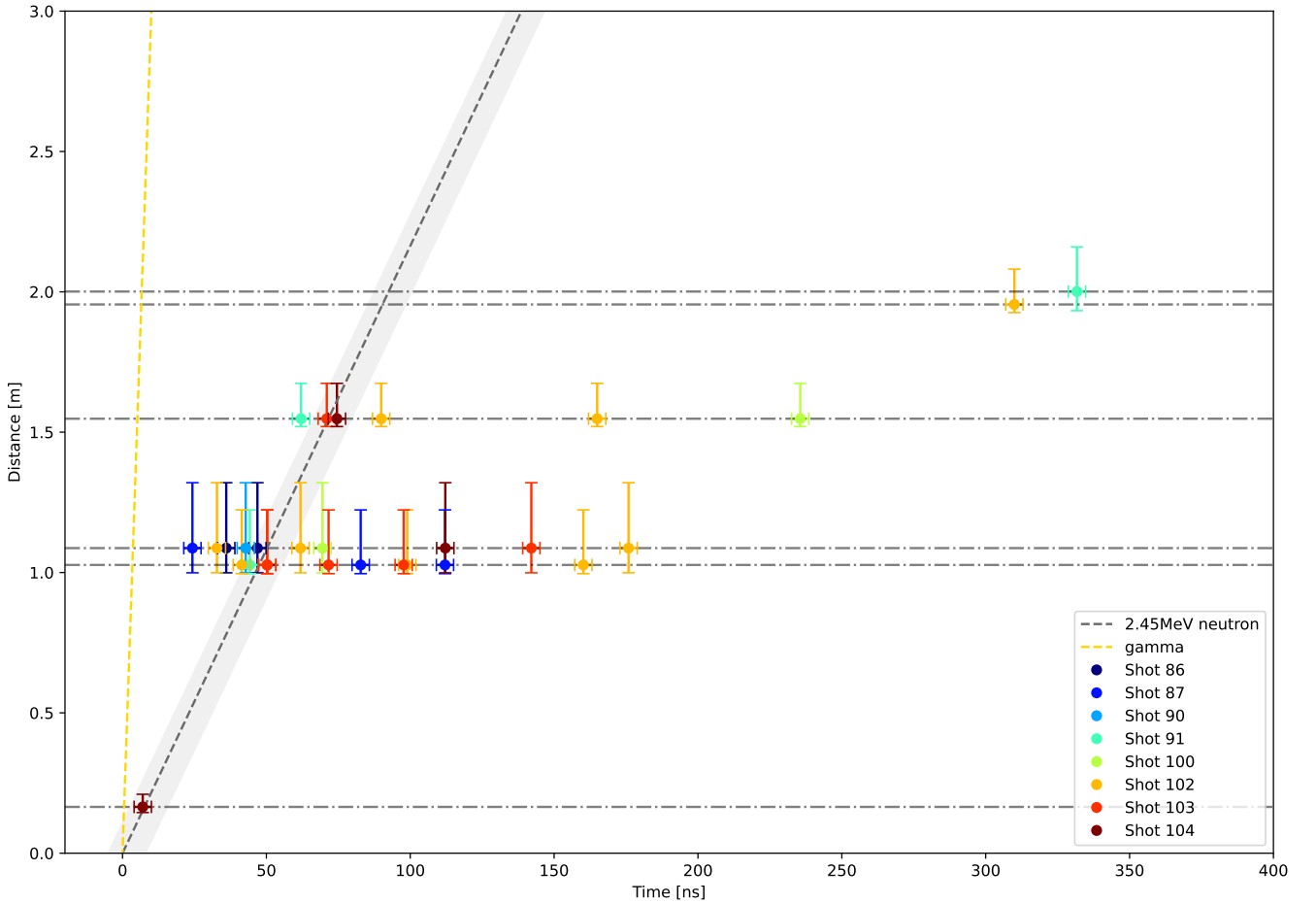
Figure 17. Aggregated n-TOF $(x - t)$ plot for all DD experiments with scintillator hits. Scintillator PMT data plotted from $t = 0$ (fusion event time) to 400 ns. Oscilloscope traces are vertically offset according to the distance from the target to the detector. Oscilloscope peaks are located, defining the time of a 'hit'. These hits are plotted at the corresponding detector distance. The trajectory of an unscattered DD neutron is shown as a diagonal dashed grey line. The trajectory of an unscattered prompt gamma ray is shown as a diagonal dashed yellow line. The time error bar on each data point represents the transit time spread of the scintillator PMTs. The position error bar on each data point represents the maximum and minimum distance of the scintillator slabs to the source. The error band on the 2.45 MeV neutron line represents the notional uncertainty in the temporal offset of the ionisation pin signal from the fusion event. Two data points from s0087 (1 m, 83 ns) and s0103 (1 m, 61 ns) are hidden behind others.

pin timing fiducial (see Section III B). The time error bar on each data point represents the transit time spread of the large scintillator ET9266 PMTs (FWHM/2 = ±3 ns, according to the manufacturer). The position error bar on each data point represents the maximum and minimum distance of the scintillator slabs to the source. The error band on the 2.45 MeV neutron line represents the notional uncertainty (-5 / +8 ns) in the temporal offset of the ionisation pin signal from the fusion event. The individual data for all PMT oscilloscope traces that were analysed to produce the dataset in Figure 17 can be found in Appendices A and B.

The aggregated n-TOF data show a clustering of data points close to the DD neutron flight path, which is consistent with the anticipated production of fusion neutrons within the target. There are no data points consistent with direct hits from a prompt (t_0) gamma source. The general scatter in the data will be partly due to the low number of counts and partly due to real physical effects. Data points to the right of the DD line can be caused by scattering of neutrons as they propagate towards detectors. This effect will reduce the velocity and increase the flight path of neutrons, causing them to arrive 'late' at the detectors. Scintillator hits consistent with unscattered DD neutrons were not observed on the 2 m detectors. We propose this is the result of statistical variability caused by the low total yield and the low solid angle subtended by the 2 m detector group. Being furthest from the source, these detectors are most likely to detect a higher fraction of scattered neutrons within their total count. Neutron scattering can also result in the production of gamma rays, which propagate faster than the neutron field and arrive 'early' at the detectors. This effect could be responsible for the data points to the left of the DD neutron line at 1 m. Alternatively, there could be an unknown issue associated with the placement of the ionisation pin during these shots.

Shots 91, 103 and 104 have scintillator hits recorded at multiple distances and with the anticipated temporal offset from both each other *and* t_0. Accounting for error bars, there are no hits to the left of the DD neutron line on these shots. In shot s0104 (brown points), a small format scintillator was positioned 17 cm from the target. The small scintillator data point lies on the DD neutron line, 8 ns from t_0. Given the close proximity of the detector to the target and the relatively tight position error bar from the small detector format, this result validates the use of the ionisation pin method for referencing data points to t_0. This experiment also registered the longest n-TOF path between 2 detectors (1.38 m). A hit was recorded at 74 ns on a large scintillator located 1.55 m from the target. The 0.17 m and 1.55 m data points plot a straight line through t_0, on top of the notional DD neutron line. This provides strong evidence that the observed signals are produced by unscattered neutrons originating in the target.

An average particle velocity was determined by analysing a subset of the above data. The subset is highlighted in Figure 18, left, and was chosen by eye to reject potential down-scattered particles. A linear regression line is plotted over the data in Figure 18, right. The regression line is forced through (0,0), which is reasonable given the validation of the t_0 diagnostic. The gradient of the line returns a velocity of $(2.17 \pm 0.13) \times 10^7$ m s^{-1} with an R-squared value of 0.589. The standard error on the gradient of the fit line was found using the following formula:

$$\sigma_s = \sqrt{\frac{1}{(n-1)} \times \frac{\sum_{i=1}^{n} e_i^2}{\sum_{i=1}^{n} d_i^2}}, \tag{3}$$

where n is the number of data points, $e_i = t_i - \tilde{t}_i$ and $\tilde{t}_i$ is the time given by the best fitting line at distance d_i. If we assume the particle mass is equal to the neutron mass, we find a particle energy of 2.46 ± 0.3 MeV. Within error, this is in agreement with the energy of a DD fusion neutron.

UKAEA created a synthetic diagnostic model using the Monte Carlo neutron transport code MCNP. This was run 1000 times for a source yield of 100 neutrons. A random selection of eight of these runs was plotted in Figure 19 for comparison with the experimental data shown in Figure 17. A good qualitative agreement can be observed which highlights the spread in the time of flight data caused by the large detector geometry and neutron scattering effects.
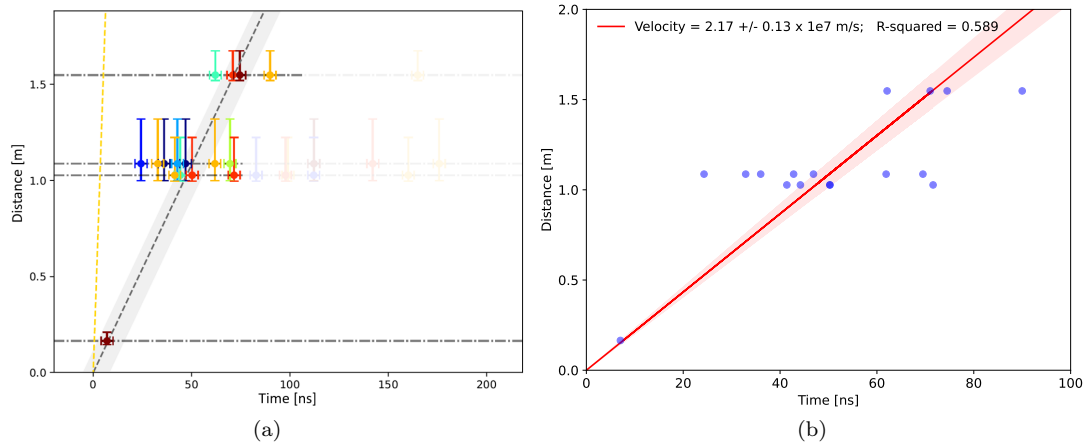
Figure 18.   Left: Subset of time-of-flight data used to determine average particle velocity. Right: Linear regression line forced through (0,0) returns a particle velocity of 2.17×10^7 m s^{-1}.
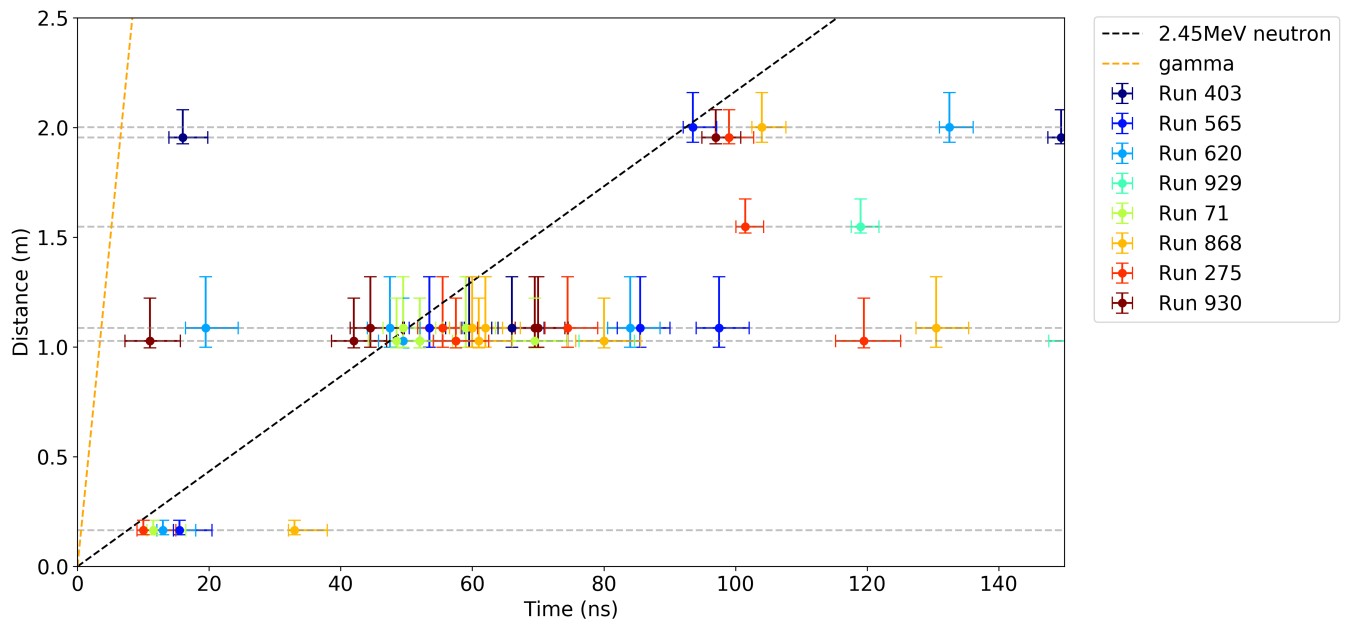

Figure 19. UKAEA ran 1000 MCNP simulations with a source yield of 100 neutrons using our scintillator geometry. Of these 8 simulations were randomly selected and plotted here for comparison with our experimental data. A numerical discrimination threshold of 10 scintillation photons per time bin was used to simulate low energy interactions not being detected. The data points represent the first time bin with signal and the scintillators have a dead time such that they can only detect one event. The time of flight spread caused by detector geometry, slow down as the neutrons are scattered and secondary gamma emission can be observed.

C. He-3 detector results

A summary of He-3 detector hits obtained during the campaign is presented in Table VI. Pulses were counted in pre-shot and shot data over the full duration of all oscilloscope acquisitions (± 2.5 ms from t_0). Oscilloscope data from all shots except s0097 (detectors not on) were interrogated. As previously mentioned, the expected signal time window extends 300 μs from t_0. 5 pulses were counted during DD shots, appearing 5–116 μs from t_0. One additional hit was observed in the whole dataset. This was seen 1.81 ms before t_0 during a H_2 null shot and is believed to be a random background count. A statistical analysis of the background contribution to the dataset is presented in Section IV D. From that analysis, the probability that a single background hit contributes to the time-gated (300 μs) dataset across all 13 DD shots is 0.058. No He-3 hits were observed within the expected time window during any test shots, null shots, or DD shots where no scintillator hits were observed. 3 out of the 5 hits observed during DD shots are correlated with hits on scintillators located immediately in front of the He-3 detectors. The locations of each scintillator and He-3 detector are detailed in Appendix D. Corresponding moderating scintillators are listed in the table. All 1 m scintillators with observed hits are listed for comparison. He-3 detectors have very good gamma discrimination and detections provide strong and complimentary evidence for the production of neutrons within targets.

Of the 9 operational shots, 4 had He-3 detections (44%). UKAEA used the MCNP code to build a synthetic diagnostic model and carried out 1000 runs with a source yield of 100 neutrons. The results shown in Figure 20 show this model predicts a detection on 39% of shots - a qualitatively good agreement.

Shot	He-3 detector with hit	Time from t_0 [us]	Moderating scintillator #	1 m scintillators with hits
0087	1	5.3	4,8	1, **8**, 9
0087	5	108	3,7	1, 8, 9
0089	12	-1810	5,9	n/a (H_2 null)
0102	11	7.4	5,9	1,4,**5**,6,8,**9**
0103	5	116	3,7	2,6,**7**,8,9
0104	4	88.9	3,7	1

Table VI. Summary of all He-3 detector TTL signals recorded. The expected signal time is within $+300$ μs from t_0. s0089 was a hydrogen null shot.
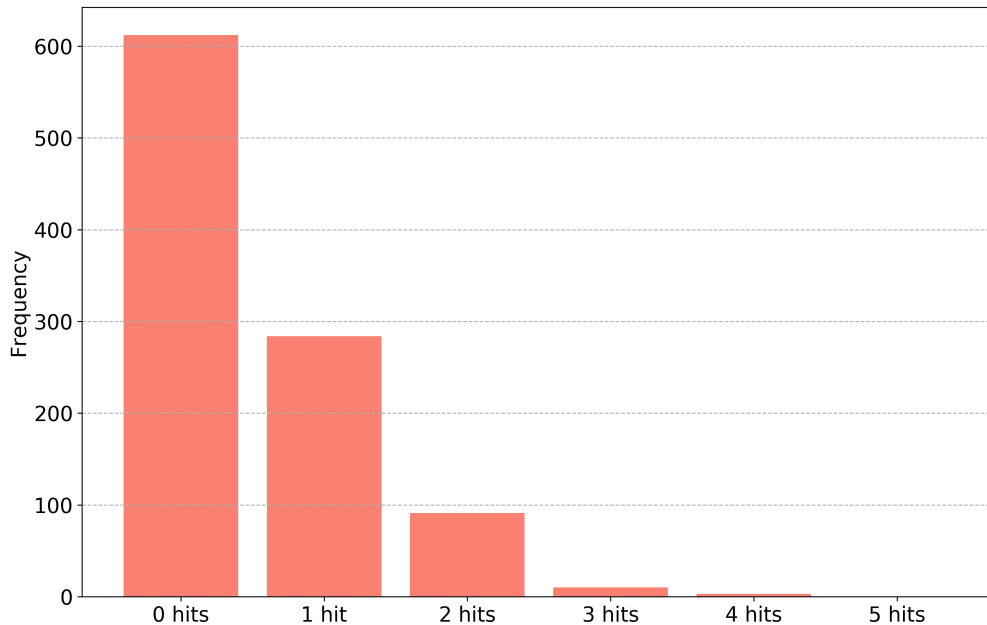
Figure 20. UKAEA ran 1000 MCNP simulations with a source yield of 100 neutrons using our He-3 detector geometry. This frequency distribution bar chart, displays the hit frequency over the full He-3 detector array. 39% of the simulations had at least one detection.

D. Statistical analysis of background contributions

We determine the likelihood of background radiation in the n-TOF dataset presented in Figure 17 by calculating the Poisson probability based on the measured average background rate of the scintillators (2.5 kHz, see Section III D 2). The dataset comprises 8 shots with 16 scintillators, each spanning a time window of 400 ns. The expected rate of background hits per 400 ns time window is 0.016. Because scintillator hits resulting from background radiation can be correlated (e.g. due to spallation), we adopt a very conservative approach by defining a false positive result as any shot with at least one background hit. The likelihood of background events as a function of the number of false positive shots is then shown in Figure 21. The likelihood that none of our positive shots contain background scintillator hits is 0.88 and that all 8 are contaminated is 4×10^{-15}. This gives us confidence that neutrons have been detected in this data set at 7.8 σ.
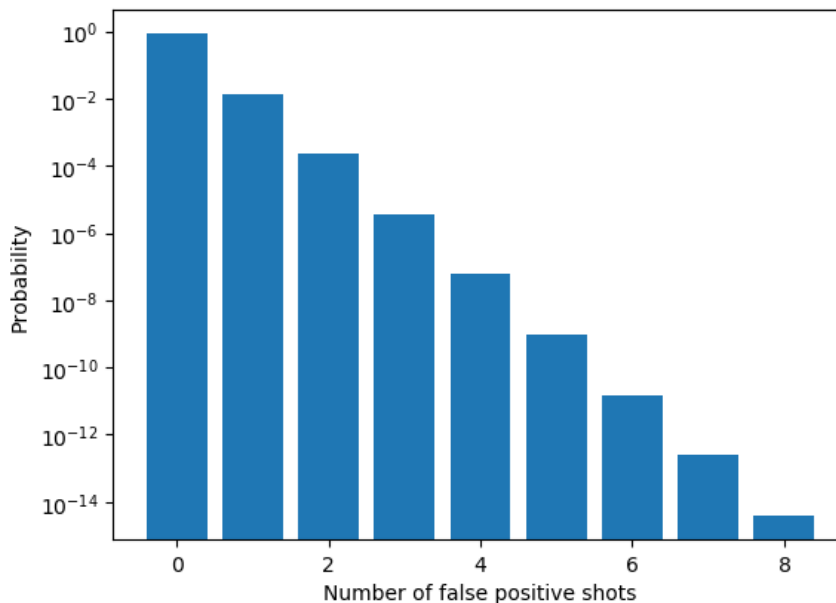
Figure 21. Probability that n out of 8 shots in the n-TOF data set shown in Figure 17 have at least one background scintillator hit.

In the case of the He-3 detectors, the combined TTL output background rate of a single detector (5 He-3 tubes combined) was measured offline at 1.38 Hz (see Section III E 2). Of the DD shots, 4 have at least one count on a He-3 detector and the expected rate of background counts per 300 μs time window is 5.0×10^{-3}. In Figure 22 we show the likelihood as a function of the number of false positive shots, where we again take the conservative view that one background count would mean that all counts in that shot are false. The likelihood that none of our positive shots contain background counts is 0.98 and that all four are contaminated is 6×10^{-10}.
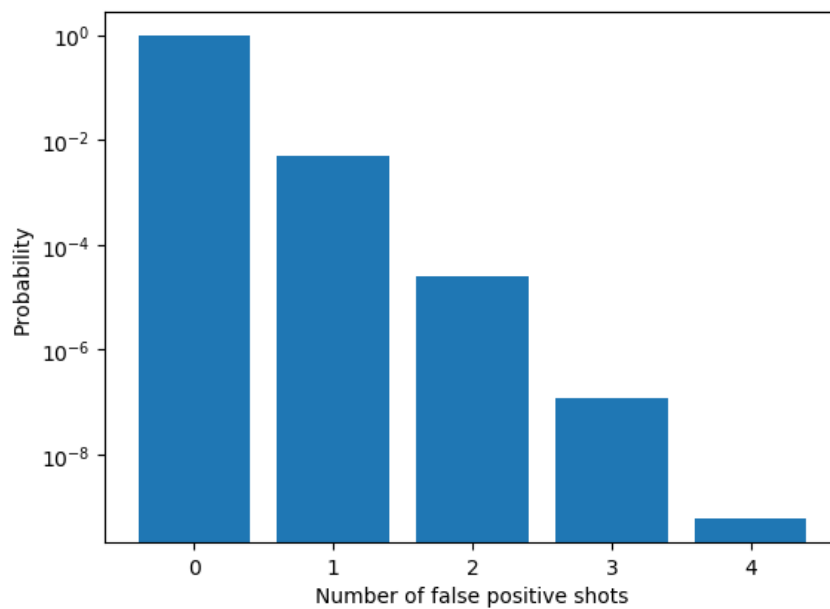
Figure 22. Probability that n out of 4 shots in He-3 data set have at least one background hit.

E.   Comparison of DD and null shots

Four hydrogen null shots (s0088, s0089, s0115 and s0116) were performed within the campaign. These were notionally identical to the DD shots in their setup, but with DD fuel substituted for hydrogen. These should behave identically to DD shots, but with no expectation of producing neutrons. During these experiments, no scintillator hits and no He-3 detector hits were observed within the expected signal time windows of the diagnostics. PMT data, n-TOF plots and He-3 data are given in Appendices A, B and C.

Within the remaining DD shots, s0092 had a very slow projectile which likely affected the target performance and s0094 was a design variant with unknown relative performance. This leaves 9 DD shots with notionally identical pre-shot configurations. Of these, one shot (s0095) recorded no scintillator hits. If we take a conservative approach and assume that this result was unrelated to the low projectile velocity, we find a success rate for recording hits during DD shots of $8/9 = 0.89$. The failure rate for recording hits is $1 - (8/9) = 0.11$. We can use the binomial distribution to answer the question 'what is the probability of getting k false negative events in n successive null shots, given a false negative probability, p, of 0.11?'. Or, in other words, 'what is the chance that the null results are false?'. Binomial distribution results are presented in Table VII for $p = 0.11$ and $n = 4$. From the cumulative probabilities, we can be over 90% sure that not more than 1 of the null results was a false negative. This strongly supports our assertion that scintillator hits are caused by events related to dynamics occurring within DD fuel targets.

Binomial PDF	Binomial CDF
P($k = 0$) = 0.6274	0.6274
P($k = 1$) = 0.3102	0.9376
P($k = 2$) = 0.0575	0.9951
P($k = 3$) = 0.0047	0.9999
P($k = 4$) = 0.0001	1.0000

Table VII. Scintillator null shot analysis. Probability of recording k false negatives in $n = 4$ null shots, given a false negative probability of 0.11.

The null shots are less powerful for the He-3 diagnostic because the failure rate is $5/9 = 0.56$. Binomial distribution results are presented in Table VIII for $p = 0.56$ and $n = 4$. From the cumulative probabilities, we can be over 90% sure that one of the null shots was not a false negative.

Binomial PDF	Binomial CDF
P($k = 0$) = 0.0375	0.0375
P($k = 1$) = 0.1908	0.2283
P($k = 2$) = 0.3643	0.5926
P($k = 3$) = 0.3091	0.9017
P($k = 4$) = 0.0983	1.0000

Table VIII. He-3 detector null shot analysis. Probability of recording k false negatives in $n = 4$ null shots, given a false negative probability of 0.56.

F. Detailed examination of a single DD fusion shot

Within this section, the full dataset from shot s0103 is presented and discussed as an example. Images of the projectile in flight were recorded in optical self-emission with a Shimadzu HPV-X2 fast framing camera (50 ns exposure, 100 ns inter-frame). The self-emission comes from gas compressed ahead of the projectile. The image is spatially calibrated using a pre-shot image of a resolution slide in the image plane. The velocity of the projectile is calculated by tracking its emitting front surface. Shimadzu data from s0103 are shown in Figure 23. In this experiment, the projectile velocity was 6.7 ± 0.2 km s^{-1} and the tilt with respect to the target was within the imaging resolution ($< 0.1°$).
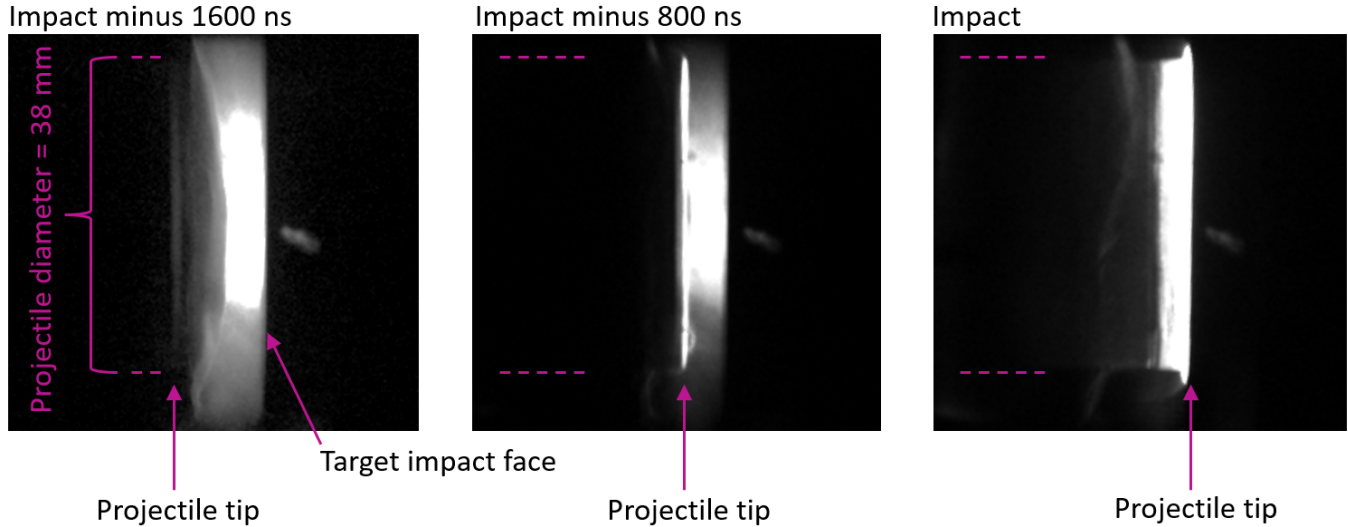
Figure 23. s0103: Optical self-emission images of the projectile in flight, recorded with a Shimadzu HPV-X2. 50 ns exposures. Projectile propagates to the right.

The timing data from the primary oscilloscope is presented in the top panel of Figure 24. The data have been referenced to the fusion event time, t_0, using the ionisation pin fusion timing fiducial (see Section III B). The data are replotted in the centre panel, on individual timescales appropriate for each diagnostic. The primary oscilloscope was triggered by the signal from an optical fibre impact fiducial (see Section III B). There are two signals (plotted in green) for redundancy. The dark green signal rises from approximately 1400 ns before t_0. This offset is related to the hydrodynamic crossing time of the target. The light green signal appears to rise much later. This is believed to be an artefact of poor optical coupling efficiency through the vacuum chamber fibre feed though used for this channel. The impact signal times do not affect the time referencing of any of the data: they are only used to trigger the primary scope. The variability of the impact fiducial rise times necessitated the development of the ionisation pin t_0 fiducial. The ionisation pin signal is shown in orange. A signal level of 1 V is the reference level used across all shots. The rise-time of the probe to 1 V is ~1 ns. The ionisation pin signal begins to rise ~20 ns from $t = 0$ in the figure. This time delay is the temporal offset of the fusion event to the pin signal, obtained from simulations (see Sections III B and III G. The blue trace monitors the auxiliary scope output, which is used to synchronise all 7 oscilloscopes. This has a rise-time of 2–3 ns.

The bottom panel in Figure 24 shows the signal from the avalanche photodiode that monitors the ambient optical intensity in the laboratory during a shot. The data is shown on the timebase of the full oscilloscope acquisition. From -50 µs to $t = 0$, there is a gradual ramp in intensity (to ~5 mV here) which is consistent with the build up of hydrogen gas from the gun at the target impact face, before the appearance of the projectile. This is observed consistently across all shots in the SHIM imaging data. At $t = 0$, there is a small (~5 mV) and transient (~1 µs) increase in the light level, which is related to the impact of the projectile onto the target. The optical light level does not increase significantly until much later, as the hot hydrogen that propelled the projectile releases into the vacuum chamber. Peak intensity on this shot is observed 80 µs after target impact. The qualitative structure of this light pulse is very reproducible across shots. The absolute intensity varies by a factor of approximately 2.

Oscilloscope traces from all scintillator/PMTs fielded on the experiment are presented in Figure 25. These plots are generated automatically following a shot. The data are time referenced to the fusion event time. 6 pulses can be seen in the data. The PMT data are presented on an (x, t) plot in Figure 26. This plot takes a similar form
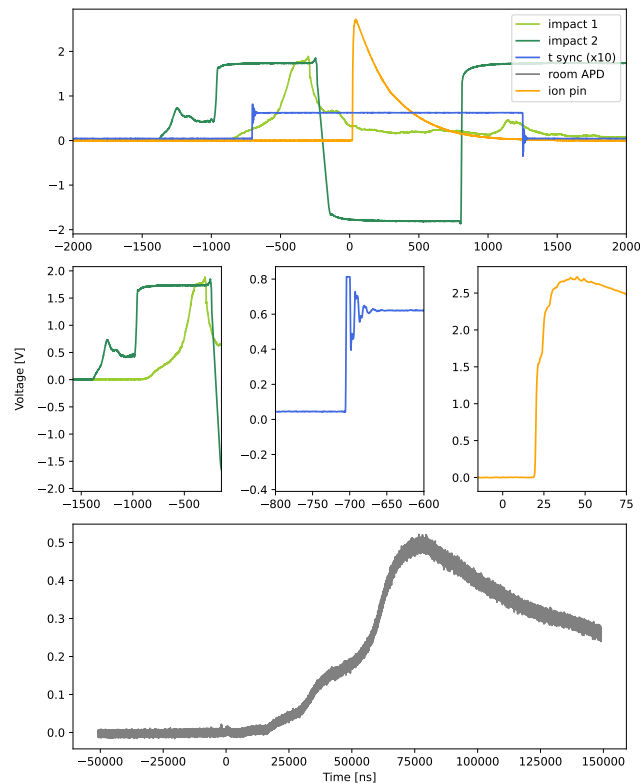
Figure 24. Overview of oscilloscope data data from s0103. Top and centre panels: Triggering and timing signals. Impact fiducials (green) are used to trigger the scope. Scope auxiliary output (blue) is monitored on all scopes for synchronisation. Ionisation pin (orange) is used to reference all data to the fusion event time, t_0. Bottom panel: An avalanche photodiode (grey) monitors the ambient optical intensity profile in the laboratory during a shot.

to the aggregated n-TOF data shown in Figure 17. The raw oscilloscope data is presented in the figure, with 0 V on each detector aligned on the y-axis with the distance from the detector to the target. The PMT manufacturers (Hamamatsu and ET) specify a PMT electron transit time of 17 ns and 40 ns for the small and large detector PMTs, respectively, which is defined (by the manufactures) to the peak of the pulse. These delays are accounted for in time referencing of the data. A peak finding algorithm finds the first peak in a given oscilloscope trace and marks that time as a hit. A discrimination threshold is set above the noise floor at 30 mV. A hit is plotted at the associated distance from the target. Error bounds were discussed in Section IV B. On this experiment, hits on detectors 5, 6 and 7 lie on the DD n-TOF line within error bounds. This provides strong evidence that the observed signals are produced by unscattered neutrons originating in the target.

Scintillator PMT traces spanning the full oscilloscope recording timebase (200 µs) are shown in Figure 27. The plot highlights the sparsity of background signals, which were analysed thoroughly in Section IV D. The signal from the APD measuring the ambient optical intensity in the laboratory is also plotted. There is no increase in the scintillator count rate as the ambient optical intensity increases. This demonstrates that the scintillators are optically light tight, removing a potential source of spurious hits on the detectors.

He-3 detector data from shot s0103 are presented in Figure 28. The pre-shot data is featureless, with no background counts observed in the acquisition window. The shot data has a 1.8 V TTL pulse on Detector 5. This occurs 116 µs after t_0, within the 300 µs expected signal time. TTL pulses are output for analogue proportional counter pulses above a threshold total charge value. This threshold rejects gamma induced signals and passes ^{3}He(n,p) reaction induced signals. Later in time there is kHz noise in the shot data. This is common on shots though not always observed (see data in Appendix C). The cause of this noise is not currently understood. We were not able to reproduce any signals by mechanically stressing the detectors. A plausible explanation is a transient voltage on the earth of the local power distribution.
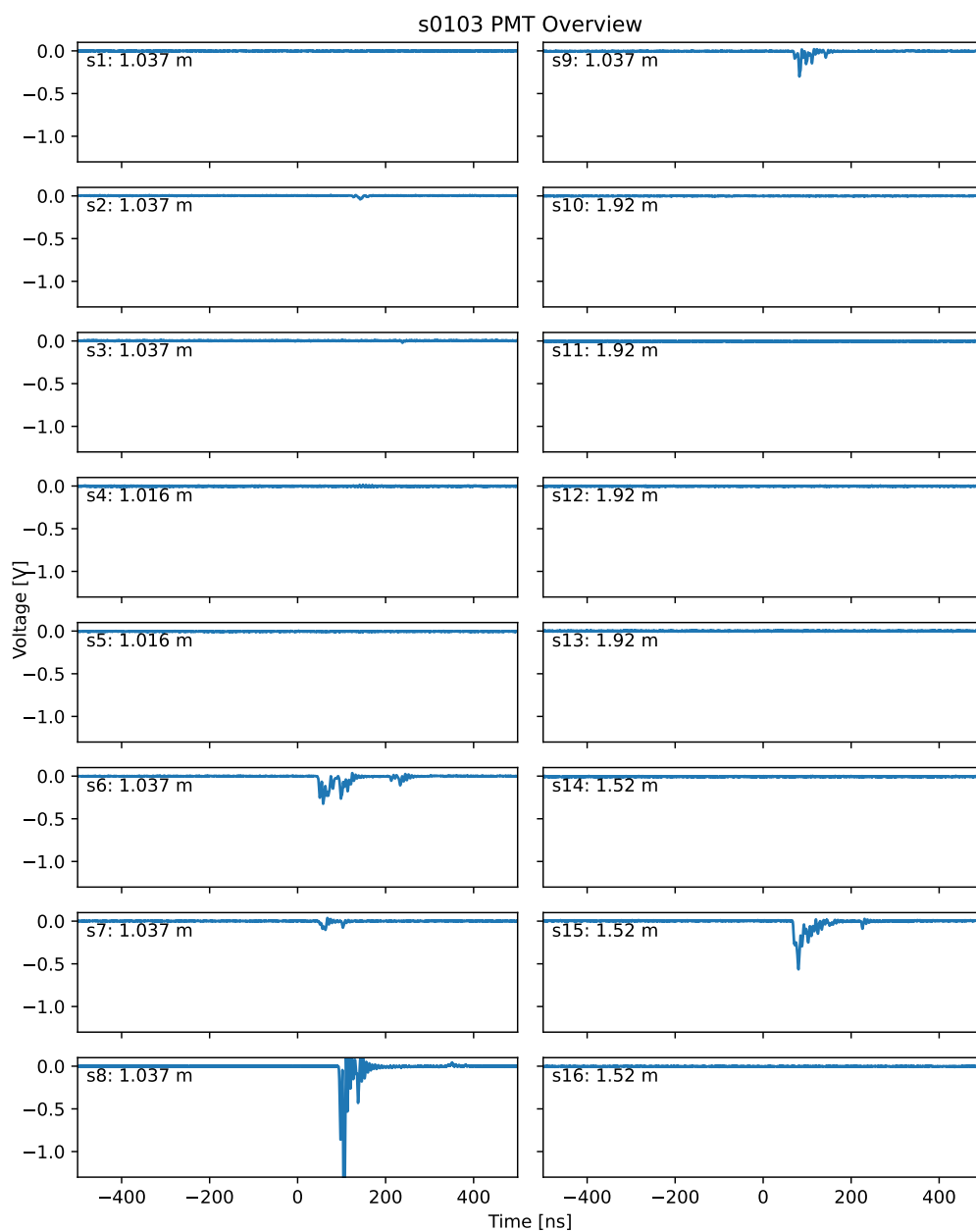
Figure 25. Oscilloscope data from 16 scintillator PMTs fielded on shot s0103. The timebase spans ±500 ns from the fusion event time.
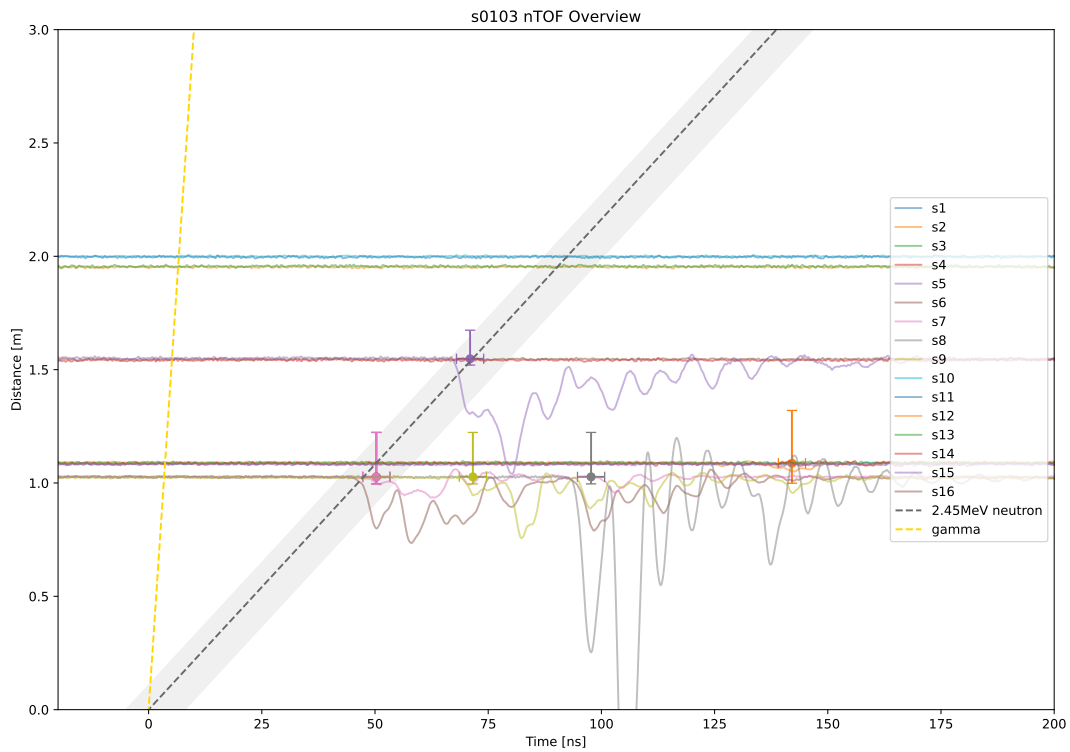
Figure 26. n-TOF $(x - t)$ plot for s0103. Scintillator PMT data plotted from $t = 0$ (fusion event time) to 200 ns. Oscilloscope traces are vertically offset according to the distance from the target to the detector. Oscilloscope peaks are located, defining the time of a 'hit'. These hits are plotted at the corresponding detector distance. The trajectory of an unscattered DD neutron is shown as a diagonal dashed grey line. The trajectory of an unscattered prompt gamma ray is shown as a diagonal dashed yellow line. The time error bar on each data point represents the transit time spread of the scintillator PMTs. The position error bar on each data point represents the maximum and minimum distance of the scintillator slabs to the source. The error band on the 2.45 MeV neutron line represents the notional uncertainty in the temporal offset of the ionisation pin signal from the fusion event. Channel 6 data point not visible behind channel 7 data point.
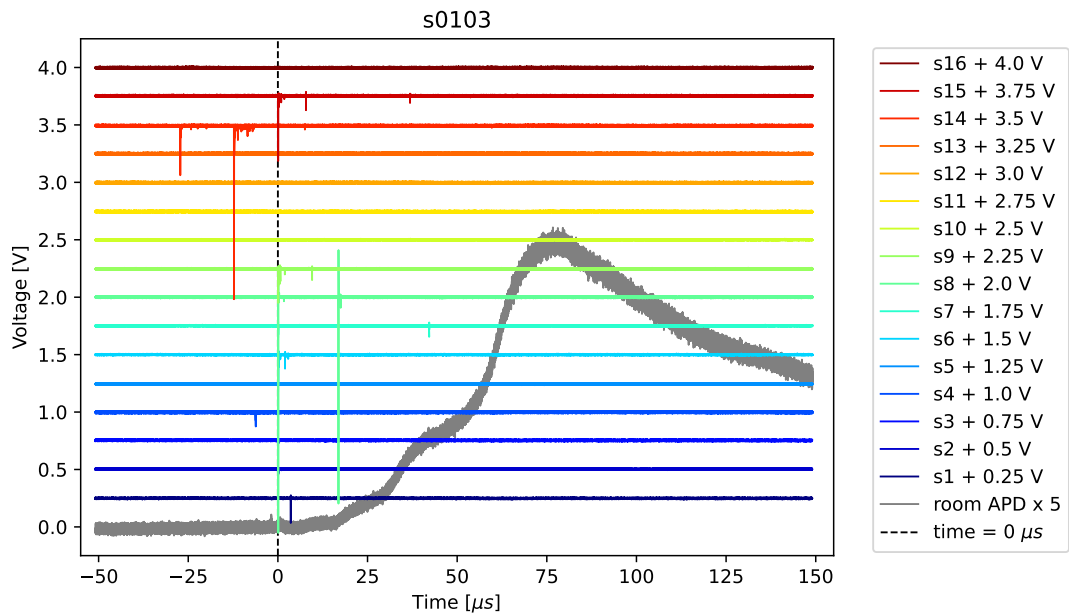
Figure 27. Full timebase oscilloscope traces from the scintillator array during shot s0103 show the sparsity of background hits. An avalanche photodiode signal (grey) shows the temporal profile of the ambient optical intensity in the laboratory during the shot.
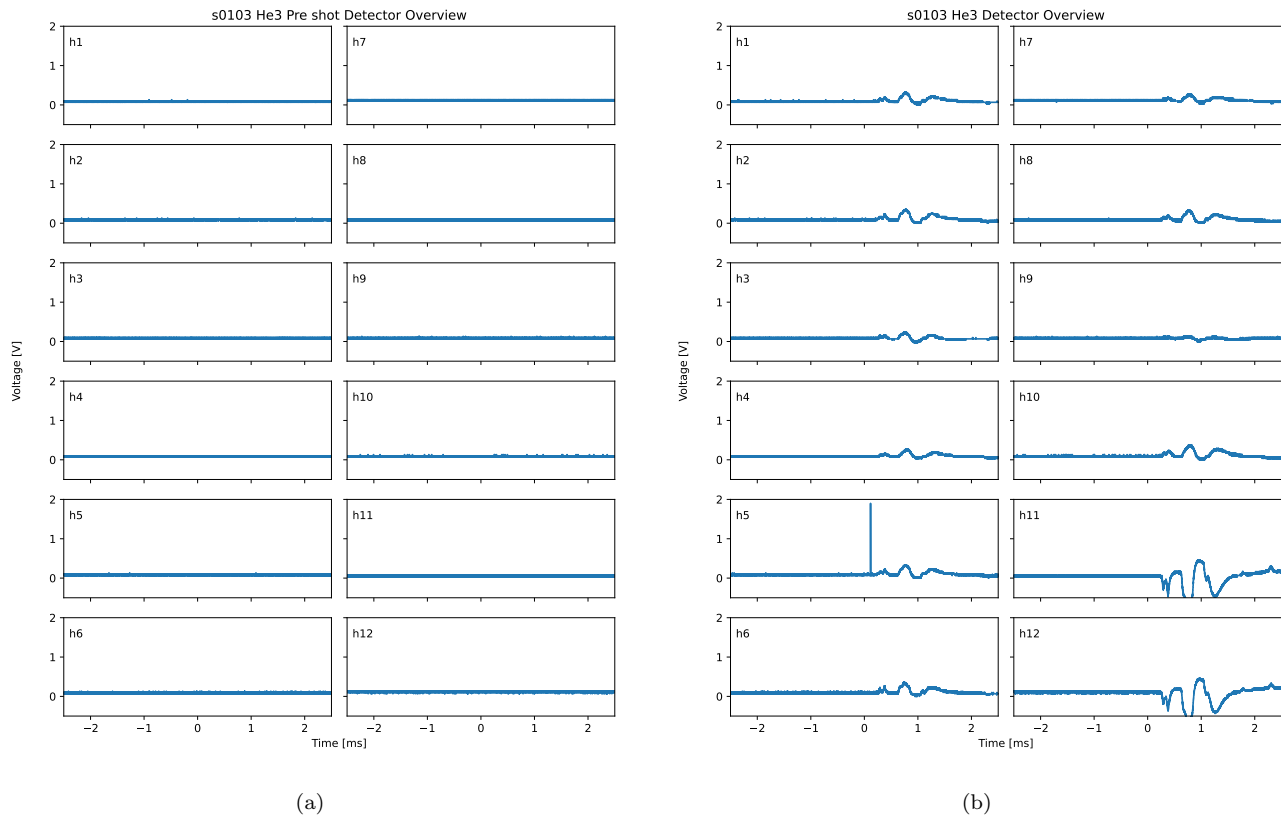
Figure 28. Oscilloscope data from the 12 He-3 detectors fielded on shot s0103. Oscilloscope channels monitor the combined TTL output from the 5 proportional counters within each detector. Pre-shot and shot data are shown.

G. Yield calculations

The neutron yield in experiments can be inferred from the observed number of counts on detectors. This is because both detector types are operating in a single hit counting regime (i.e. there is no pulse pileup expected). Shots s0102, s0103 and s0104 were chosen for analysis because of their consistent, relatively high projectile velocity. Bayesian inference was used to obtain a posterior distribution for the yield in these shots given the number of hits detected. A binomial likelihood function for the number of detected neutrons was developed based on our knowledge of the detector solid angles and 2.5 MeV neutron counting efficiencies (see Section III F). A non-informative uniform prior was used for the yield. Note that the effect of neutron scattering is not included in these calculations. The yield probability density functions from the three shots were combined to produce the distributions shown in Fig. 29. Most likely credible yields according to the scintillator and He-3 measurements are $24 - 68$ and $12 - 124$, respectively. This 95% credible interval is indicated with vertical dashed lines and noted in the plot titles. The yield uncertainty in the He-3 data is larger compared to the scintillator results because fewer counts were recorded. The good agreement in yield between two distinct detector types is further evidence that observed counts were induced by a common source of DD fusion neutrons.
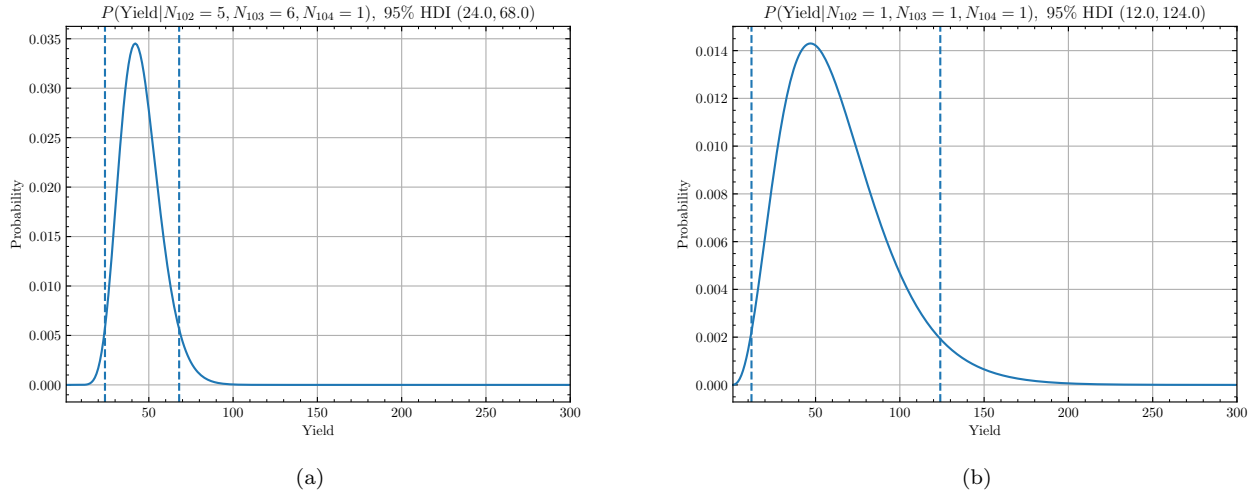
Figure 29. Posterior distributions for the neutron yield according to the number of hits observed on scintillators (left) and He-3 detectors (right) on shots s0102, s0103 and s0104. 95% credible intervals are indicated with vertical dashed lines and noted in the plot titles. Most likely yields according to scintillator and He-3 data are 42 and 47, respectively.

V.   SUMMARY AND CONCLUSIONS

In summary, 21 experiments were performed during the validation campaign, of which 9 were notionally operational DD fusion targets. In these 9 shots, 29 scintillator hits were recorded within the anticipated detection time window, distributed over 8 of the operational targets. The absence of hits from one of these targets is likely due to the relatively low projectile velocity during that shot. Additionally, 5 hits were recorded on He-3 detectors within the anticipated detection time window, distributed across 4 of the operational targets. The results qualitatively agree with the synthetic detector modelling carried out by UKAEA using the code MCNP.

Repeatable coincident detection of particles on multiple scintillator detectors has been demonstrated, with a negligible background contribution. Hits were recorded within a 400 ns window extending from the anticipated neutron emission time. An absence of detections during null shots was observed. The average background count in the measurement time window was extremely small. We have demonstrated through measurements of background count rates and statistical analysis that there is an 88% likelihood that none of our shots with detections contain background scintillator hits. Furthermore, the probability that all 8 shots have signal due to background radiation is 4×10^{-15}, or 7.8 σ. This effectively rules out the possibility of background radiation as a source of spurious results on the scintillator detectors. Additionally, we have shown that the detectors did not respond to changes in the ambient laboratory light levels produced by optical emission from within the experimental chamber.

The above results strongly indicate that dynamics within a DD target result in the generation of energetic particles. The number of scintillator hits recorded dropped off according to the solid angle subtended by detector groups at different distances, consistent with a particle source at the target location. The nature of the energetic particles was determined using an alternate detector type and time-of-flight measurements. Unlike the scintillators, the He-3 detectors have a very low sensitivity to energetic particles other than (moderated) neutrons. The observation of 5 counts on He-3 detectors over the course of the campaign is very strong evidence for the detection and production of neutrons during an experiment. Whilst the production time of the neutrons cannot be localised precisely from He-3 data, the aggregated He-3 detector dataset demonstrates that neutron levels within the detection time window (300 µs) are well above the background. From measurements of the background count rate and statistical analysis, there is a 98% likelihood that none of our shots with detections have a contribution from random background radiation. Furthermore, the chance that all 4 shots are due to background radiation is 6×10^{-10}. Given the purely hydrodynamic nature of the experiment, there are no mechanisms for the generation of energetic particles other than fusion neutrons and x-rays. Thermal x-rays at anticipated target temperatures would not have sufficient energy to penetrate the wall of the vacuum vessel.

The particle arrival time at scintillators positioned different distances from the source was used to determine the particle velocity. On multiple shots, time-of-flight data was recorded that is consistent with the propagation of 2.45 MeV DD fusion neutrons. No data was recorded that is consistent with the propagation of target generated photons (optical/x-rays/gamma rays). The observation of a hit on a small scintillator detector positioned close to the target validated the operation of the fusion event (t_0) timing fiducial inserted into each target. The t_0 diagnostic provided an additional point (at $x = 0$) for assessing particle time-of-flight. The average particle velocity from time-of-flight measurements was found to be $(2.17 \pm 0.13) \times 10^7$ m s^{-1}. Assuming the mass of a neutron, this corresponds to a particle energy of 2.46 ± 0.3 MeV. Within error, this is in agreement with the energy of an unscattered DD fusion neutron.

Estimates of neutron yield from the detected number of hits on both detector types are in agreement. The scintillators and He-3 proportional counters operate on fundamentally different principles and were independently, absolutely calibrated for their 2.5 MeV counting efficiency. Consistency between the two detector types therefore provides further evidence that observed counts were induced by a common source of DD fusion neutrons.

The collective strength of evidence presented leads to the conclusion that DD fusion neutrons have been observed and that they were produced within targets driven by FLF's large two-stage gas gun. UKAEA have verified the experimental setup, modelled the detector responses and witnessed two experiments. They have also reviewed the full campaign dataset, analysis and interpretation of the results.

VI.   ACKNOWLEDGEMENTS

Appendix A: Individual shot data: PMTs

Scintillator PMT oscilloscope data for all DD and H_2 experiments. Data are delay corrected and time referenced to the ionisation pin t_0 diagnostic. The timebase spans ± 500 ns from the fusion event time. Test shot data are not included because there is no relevent time reference on these timescales.
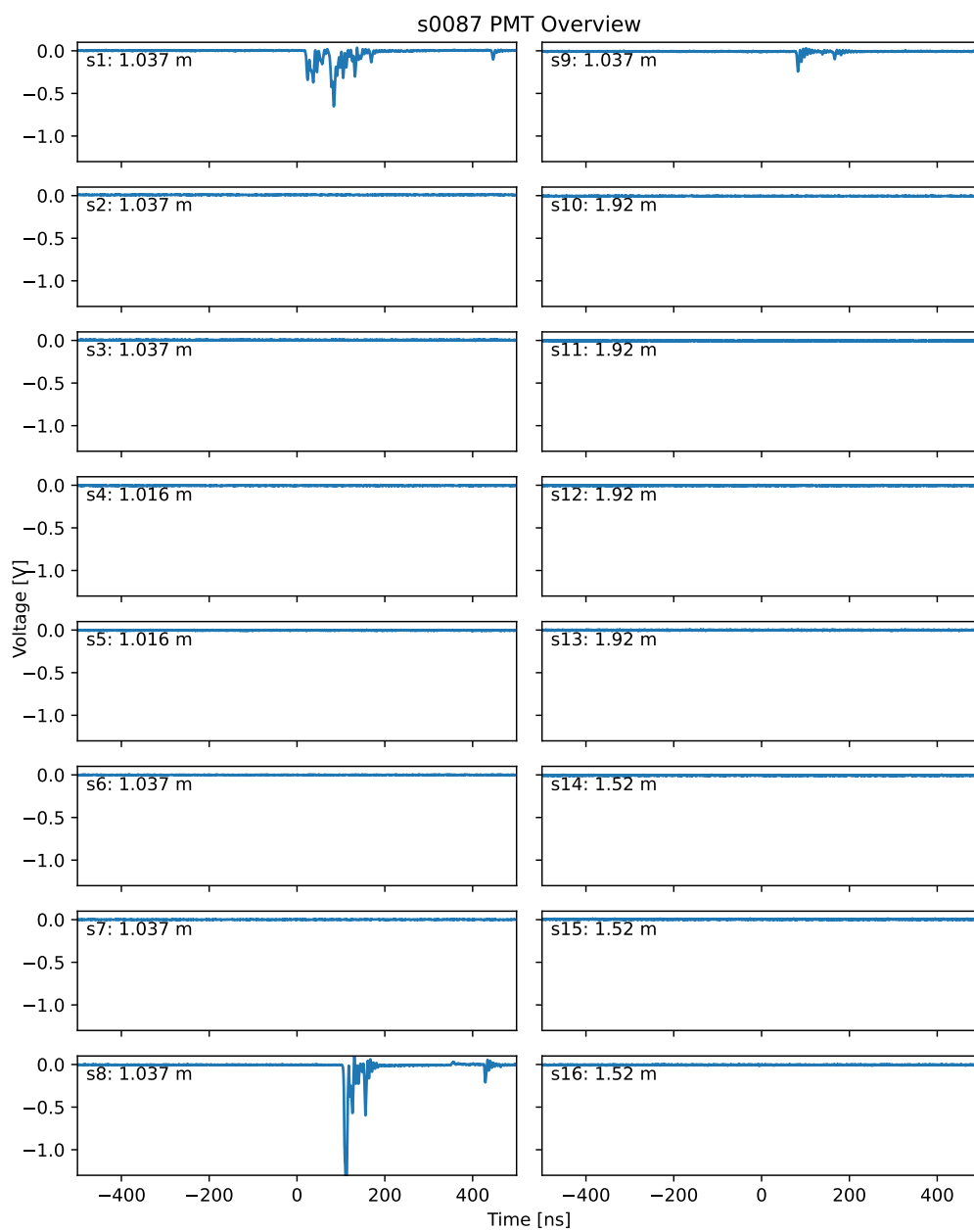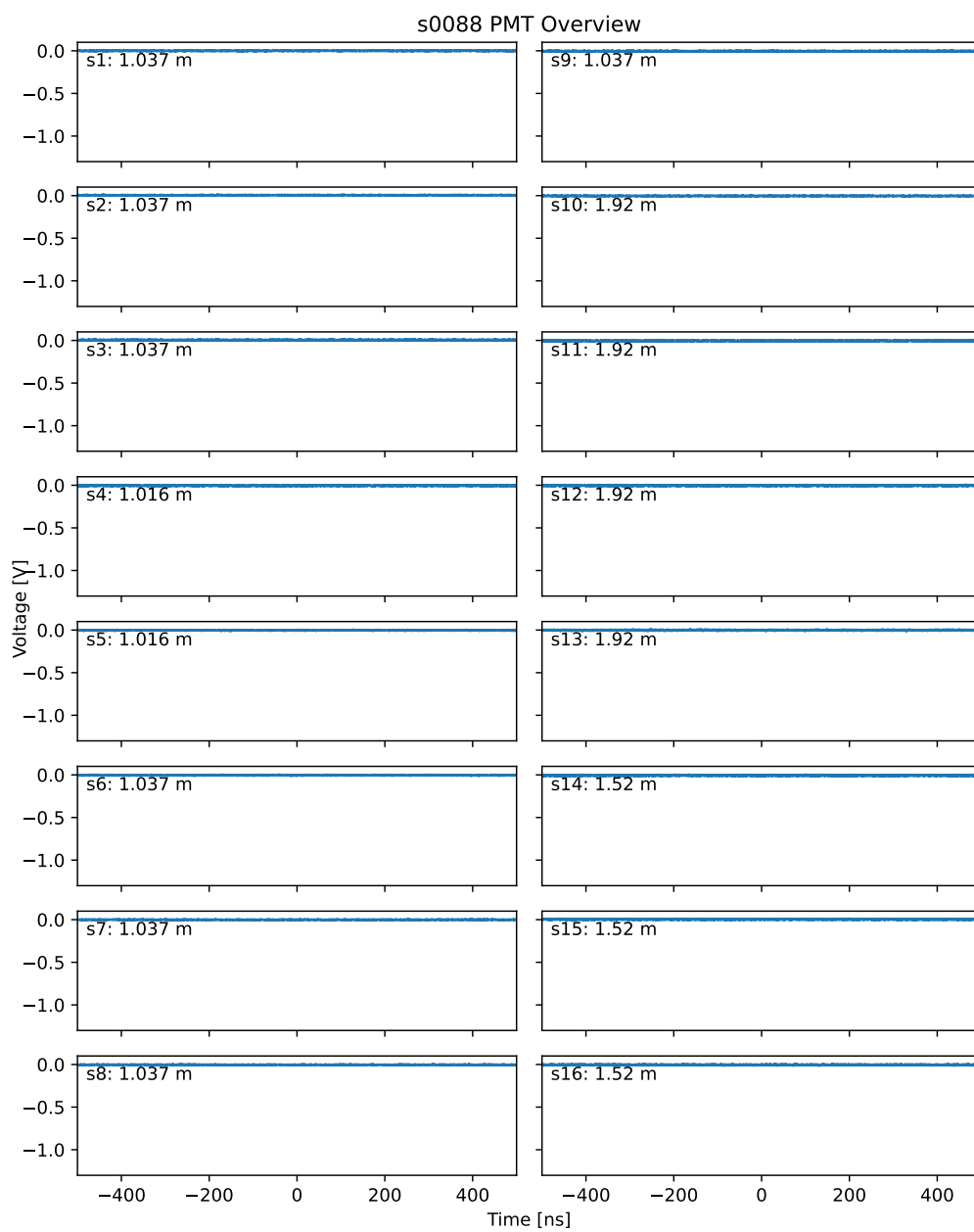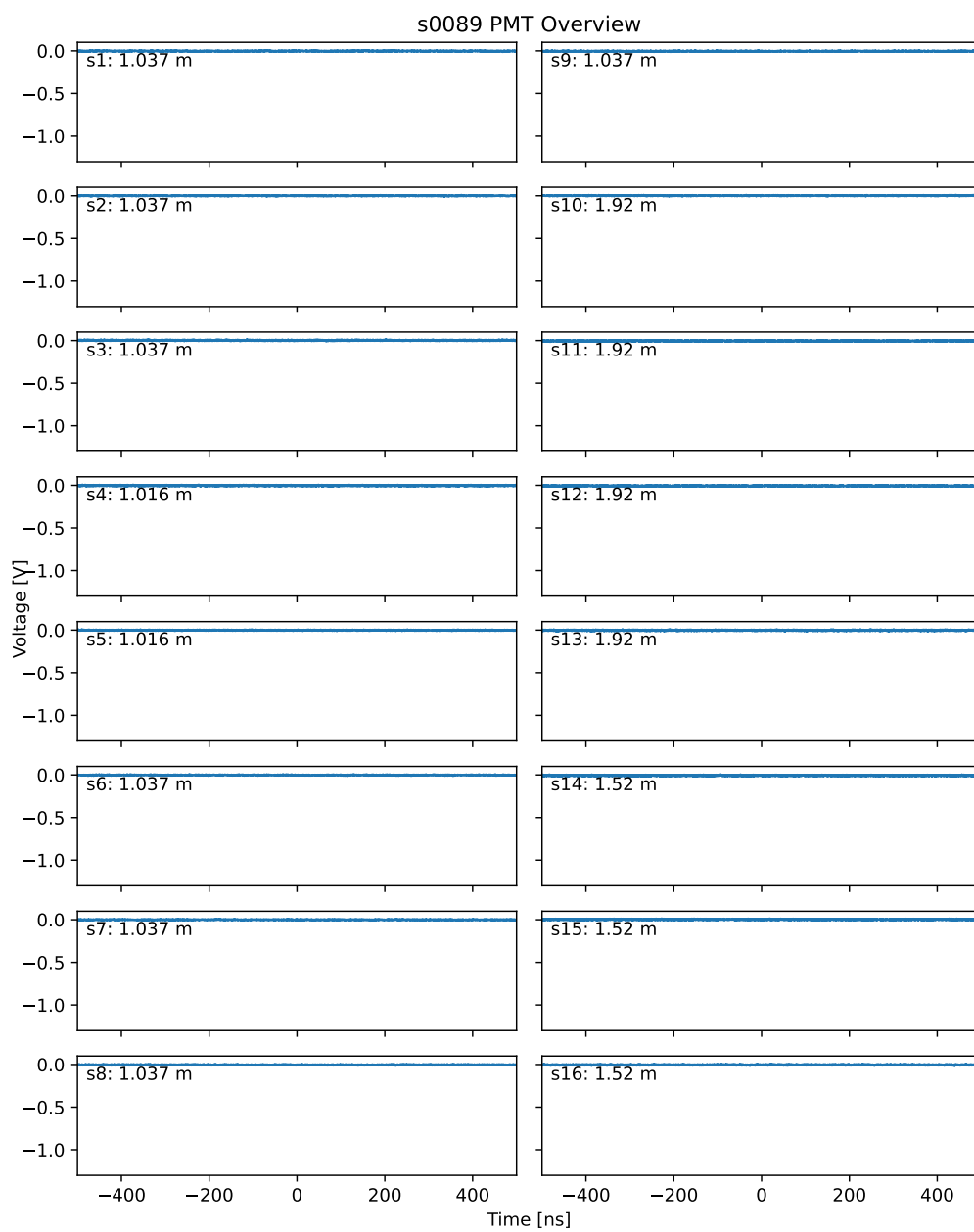

Figure 30. s0086: DD shot.

Figure 31. s0087: DD shot.

s0088 PMT Overview

s1: 1.037 m

s2: 1.037 m

s3: 1.037 m

s4: 1.016 m

s5: 1.016 m

s6: 1.037 m

s7: 1.037 m

s8: 1.037 m

s9: 1.037 m

s10: 1.92 m

s11: 1.92 m

s12: 1.92 m

s13: 1.92 m

s14: 1.52 m

s15: 1.52 m

s16: 1.52 m

Voltage [V]

Time [ns]

Figure 32. s0088: H_2 null shot.

Figure 33. s0089: H_2 null shot.

s0090 PMT Overview

ss1: 0.125 m

s1: 1.037 m

s9: 1.037 m

s2: 1.037 m

s10: 1.92 m

s3: 1.037 m

s11: 1.92 m

s4: 1.016 m

s12: 1.92 m

s5: 1.016 m

s13: 1.92 m

s6: 1.037 m

s14: 1.52 m

s7: 1.037 m

s15: 1.52 m

s8: 1.037 m

s16: 1.52 m

Voltage [V]

Time [ns]
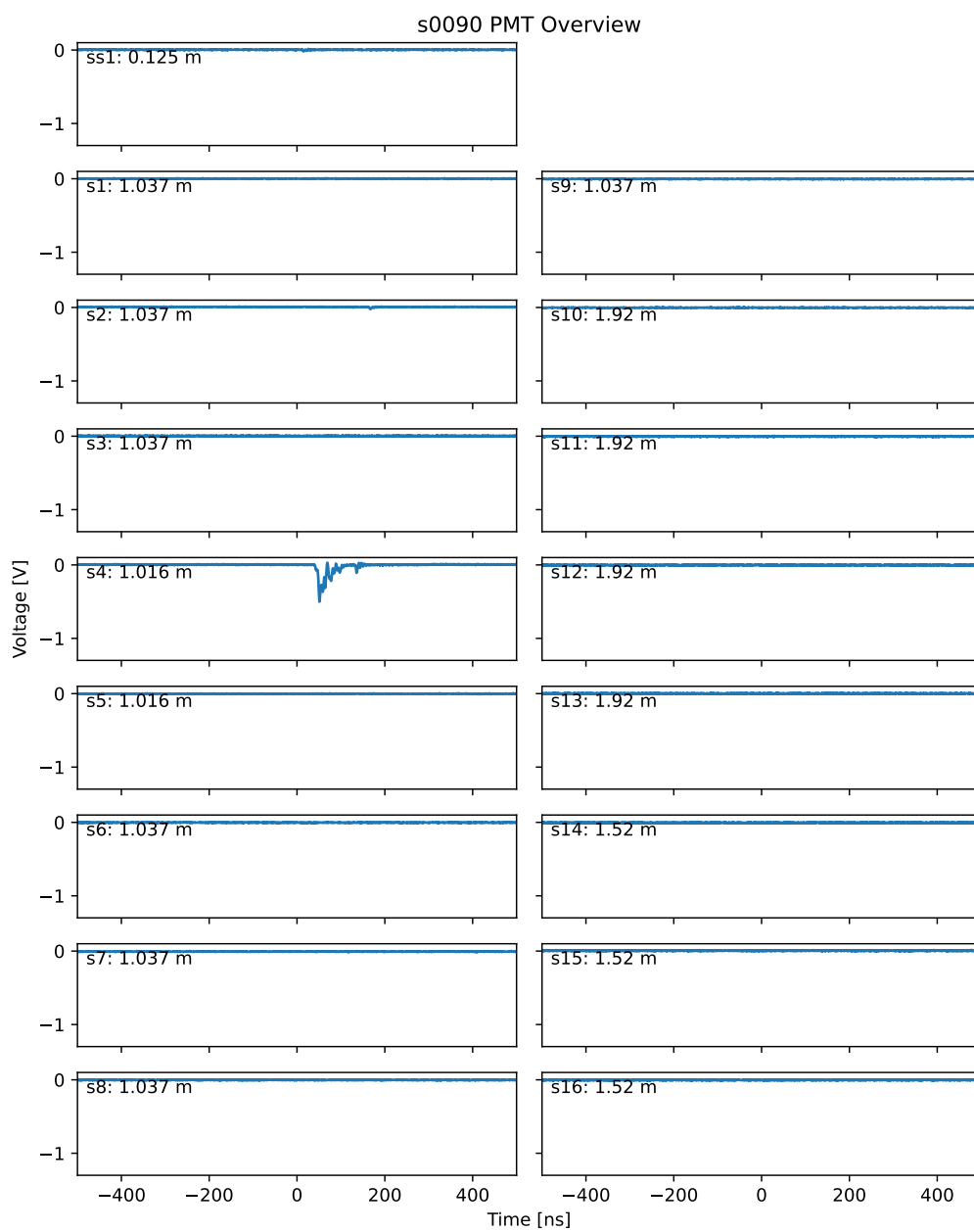
Figure 34. s0090: DD shot.
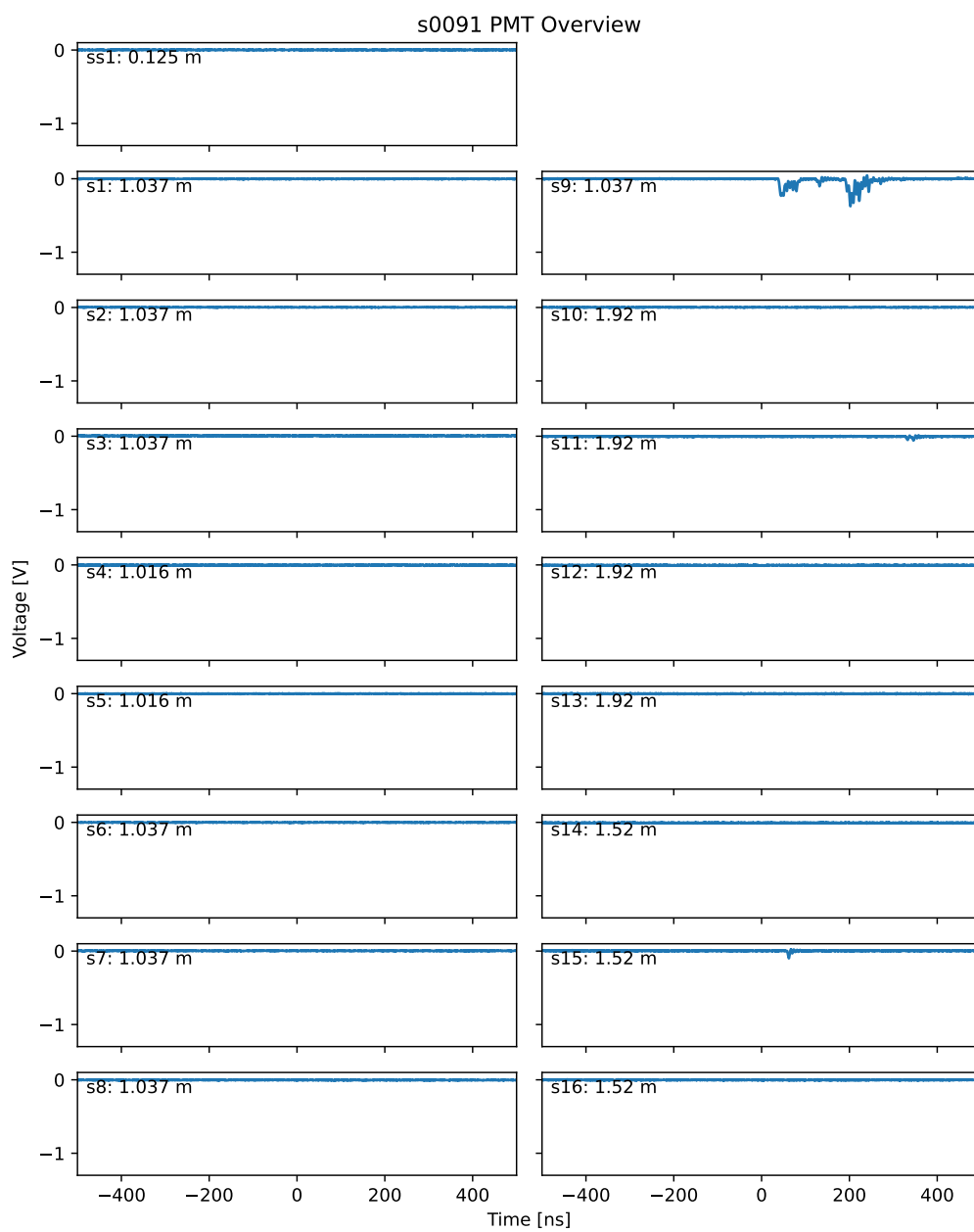
Figure 35. s0091: DD shot.
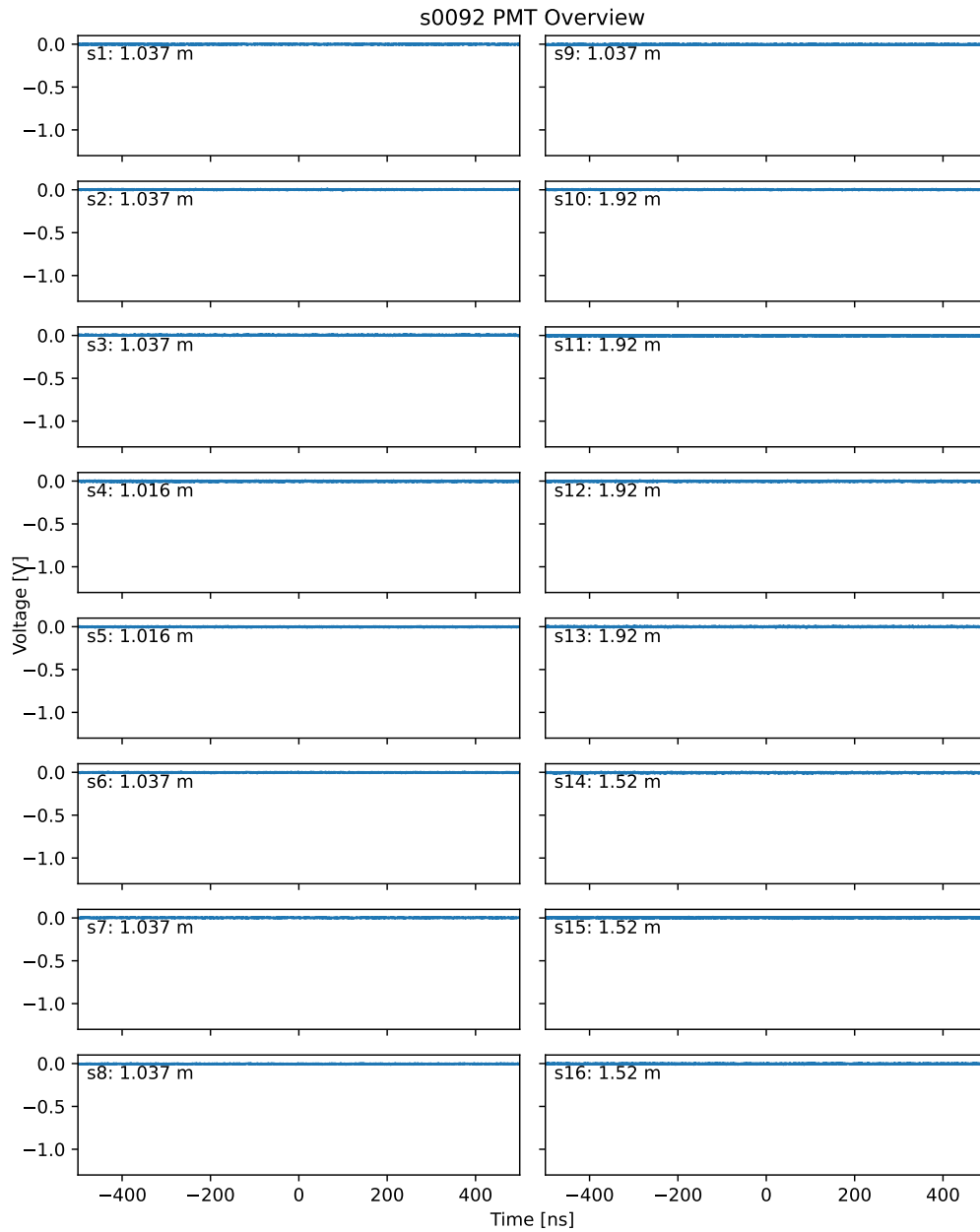
Figure 36. s0092: DD shot (projectile failure).
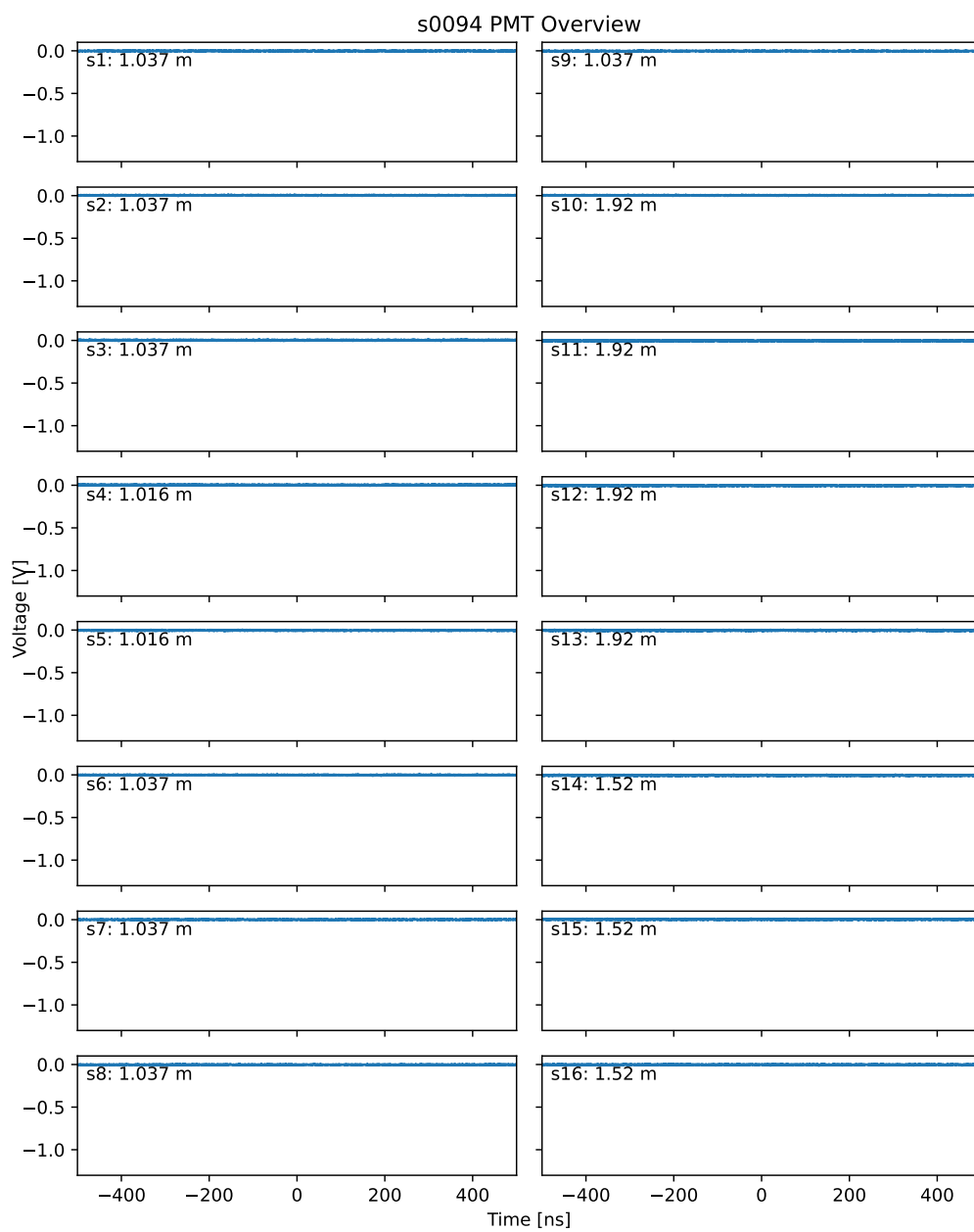
Figure 37. s0094: DD variant shot.
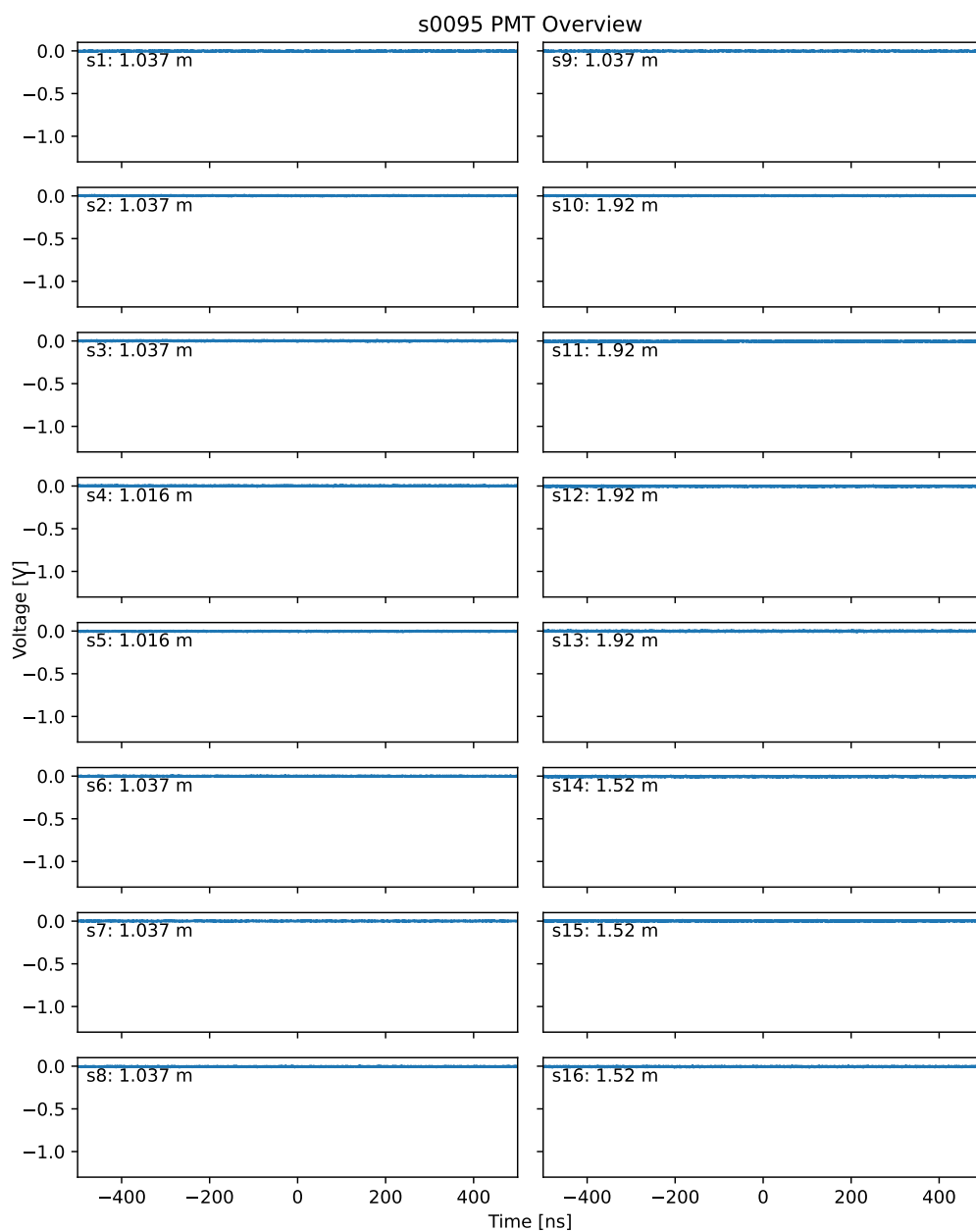
Figure 38. s0095: DD shot.
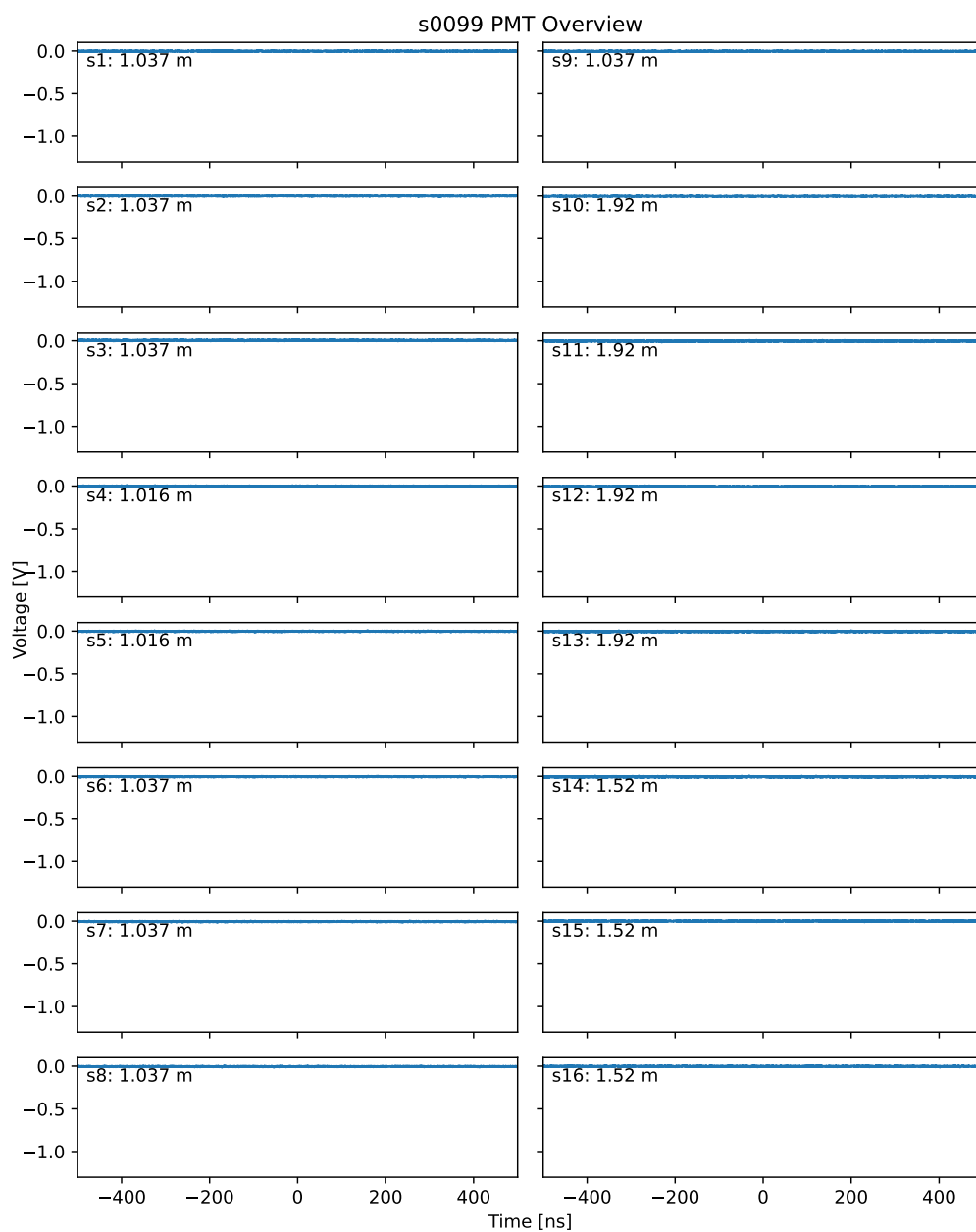
Figure 39. s0099: DD shot (mechanical target failure).

s0100 PMT Overview

s1: 1.037 m

s2: 1.037 m

s3: 1.037 m

s4: 1.016 m

s5: 1.016 m

s6: 1.037 m

s7: 1.037 m

s8: 1.037 m

s9: 1.037 m

s10: 1.92 m

s11: 1.92 m

s12: 1.92 m

s13: 1.92 m

s14: 1.52 m

s15: 1.52 m

s16: 1.52 m

Voltage [V]

Time [ns]
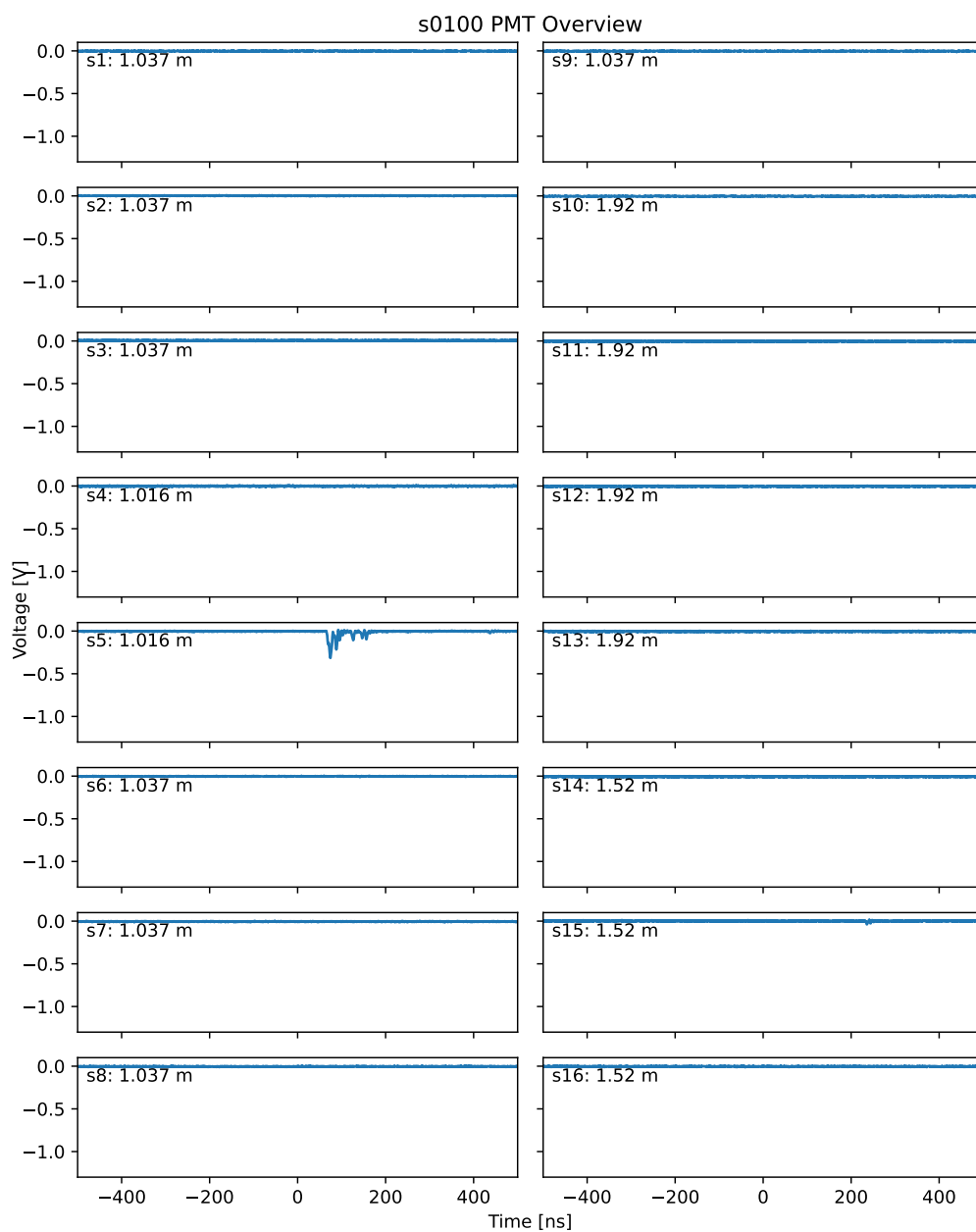
Figure 40. s0100: DD shot.

s0101 PMT Overview
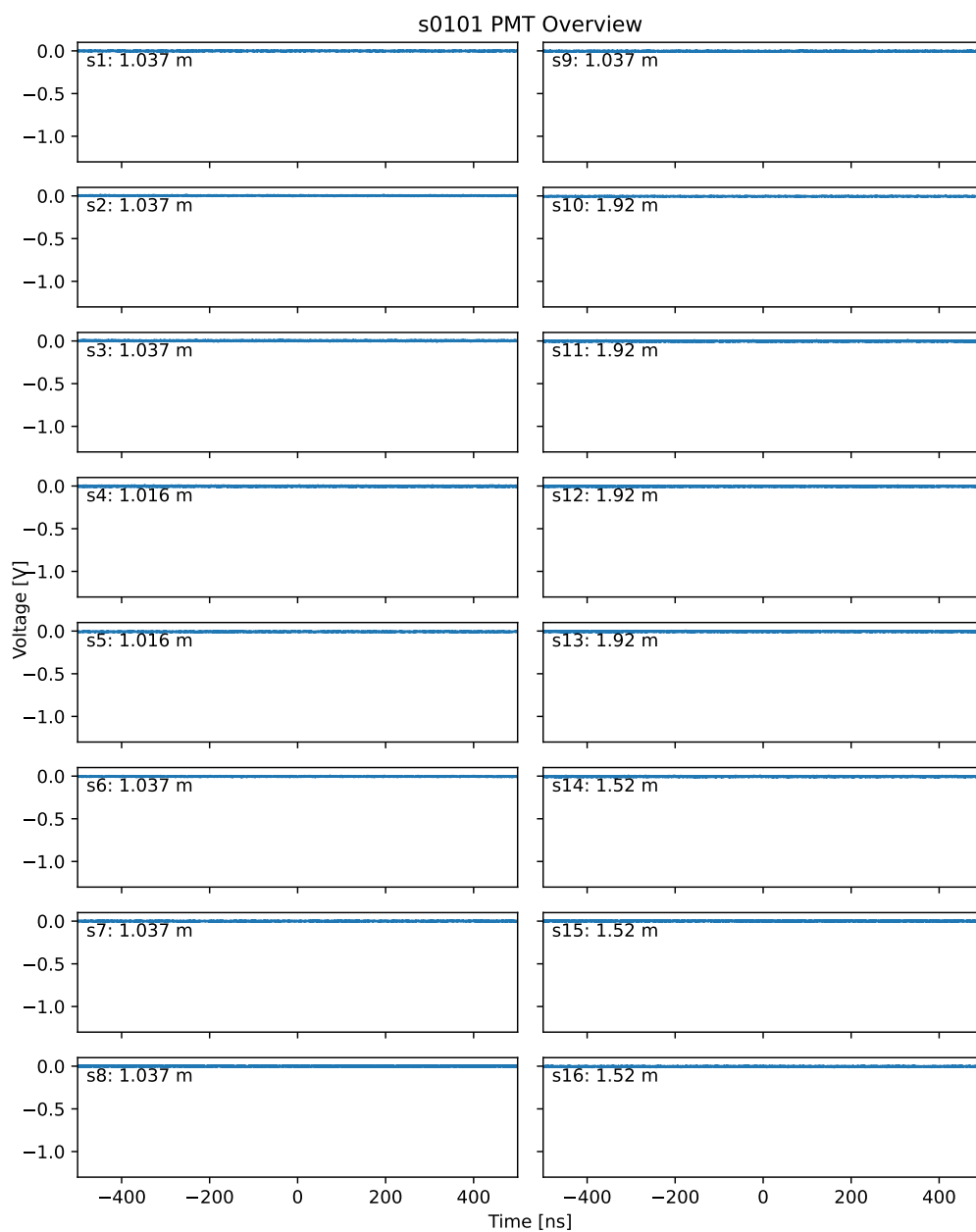

Figure 41. s0101: DD shot (mechanical target failure).
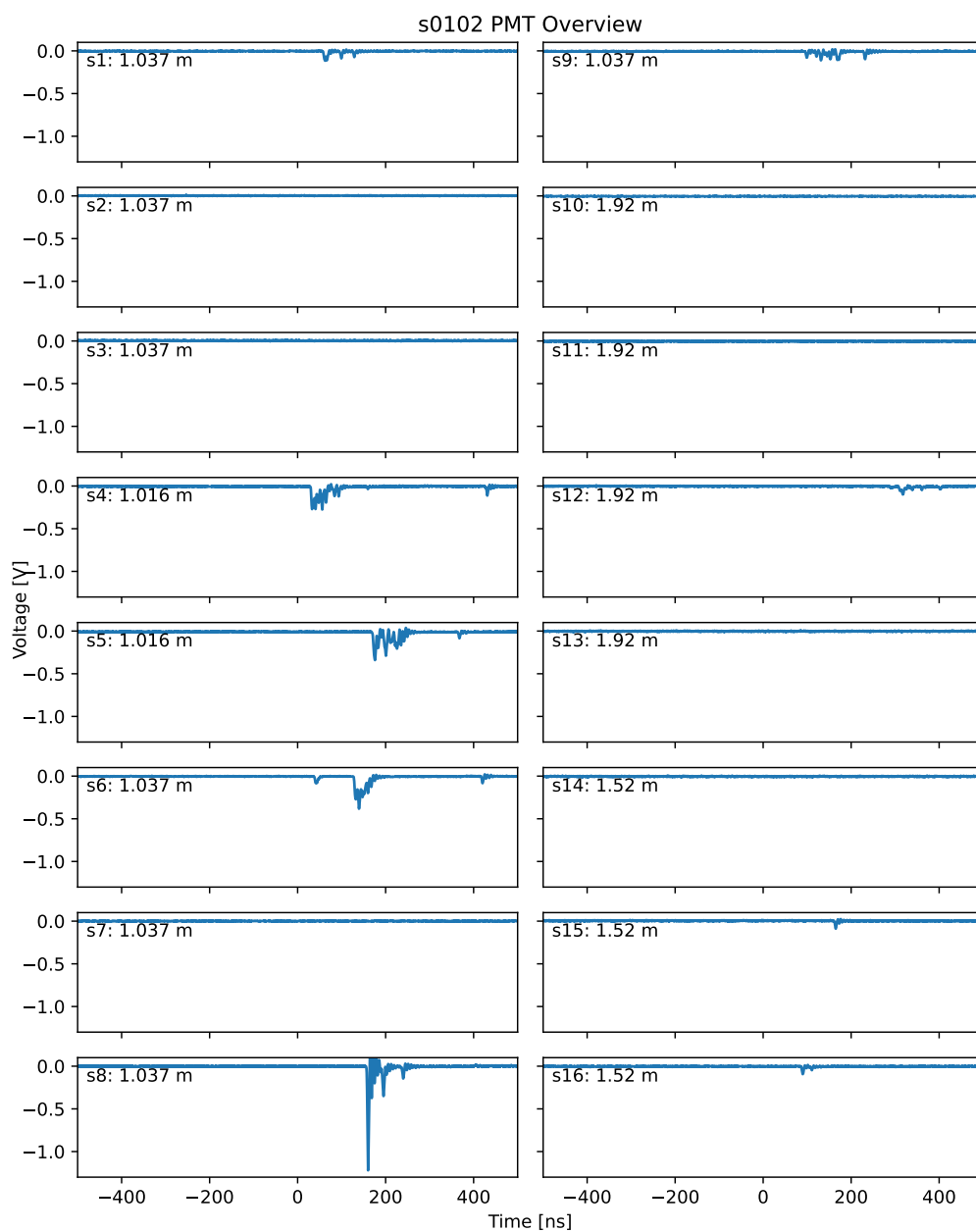
Figure 42. s0102: DD shot.
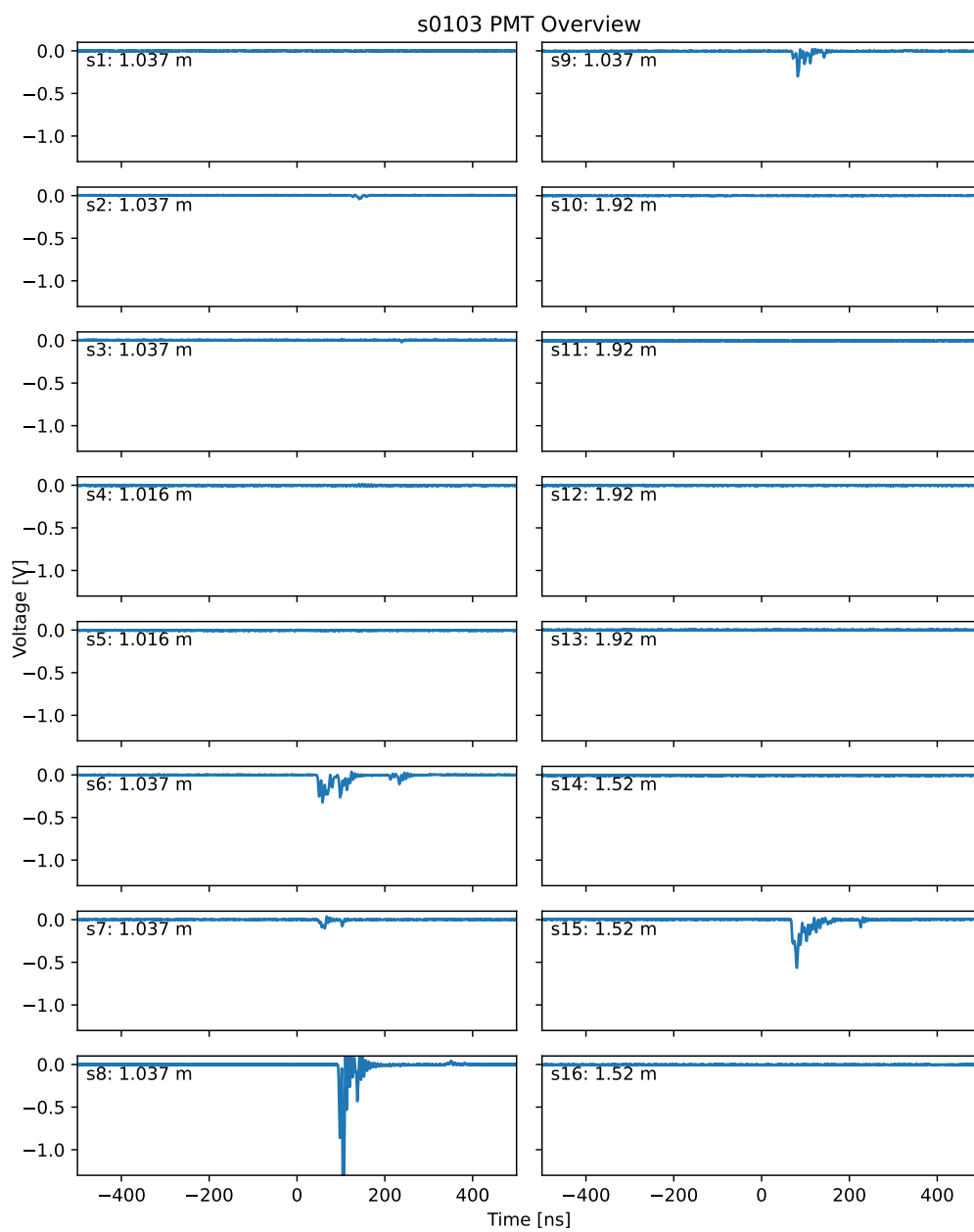
Figure 43. s0103: DD shot.
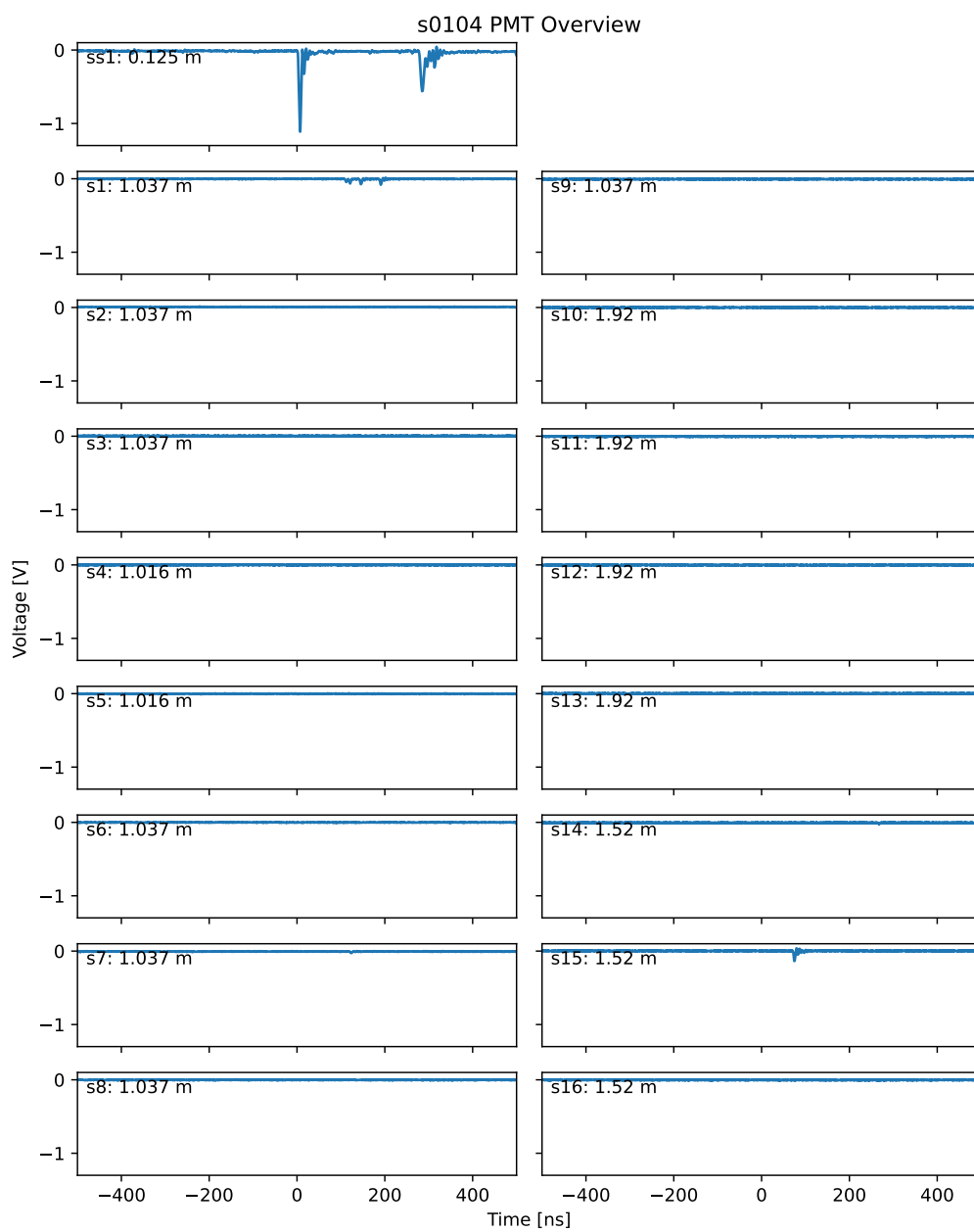
Figure 44. s0104: DD shot.

s0115 PMT Overview
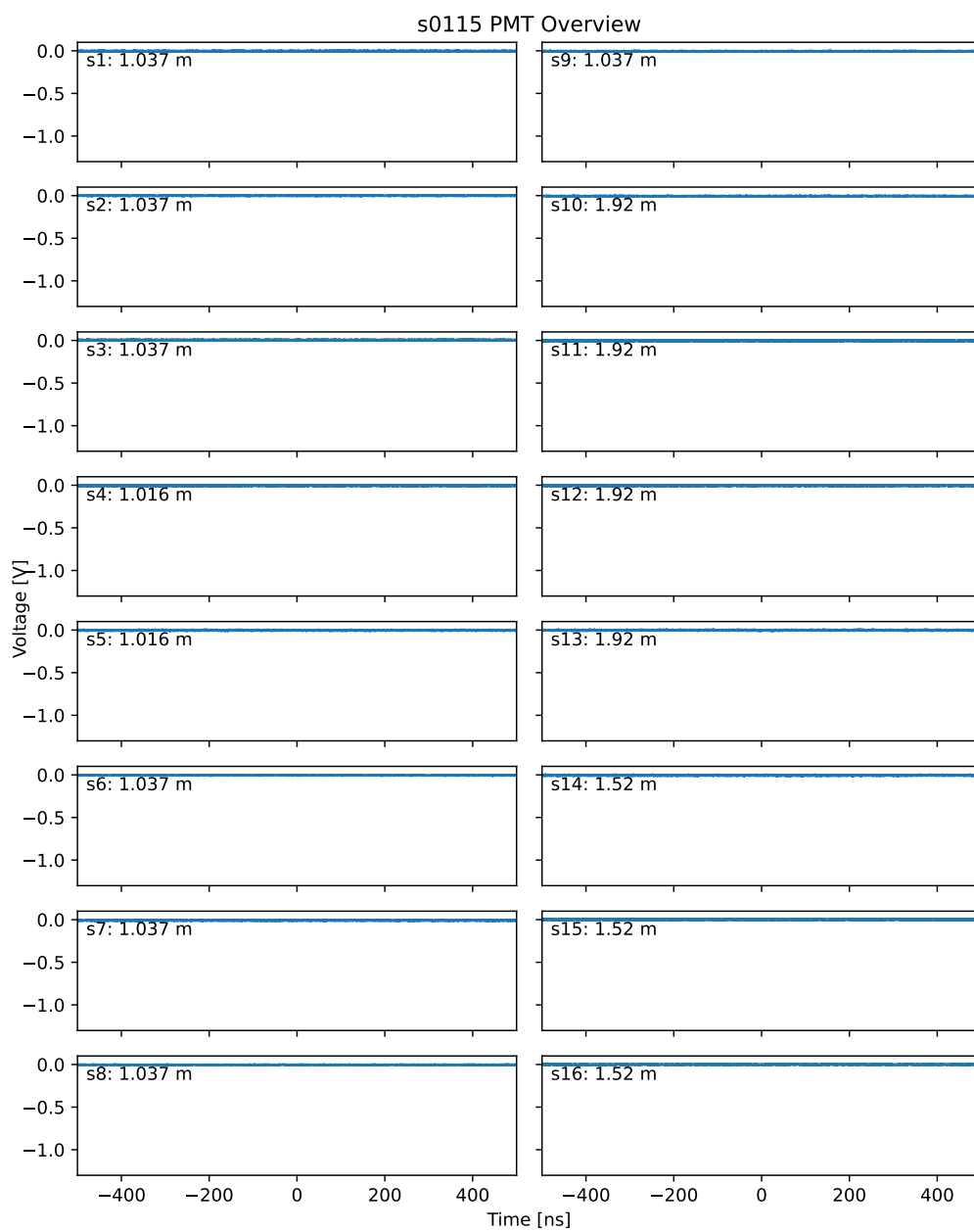
Figure 45. s0114: H$_2$ null shot.

s0116 PMT Overview

s1: 1.037 m

s2: 1.037 m

s3: 1.037 m

s4: 1.016 m

s5: 1.016 m

s6: 1.037 m

s7: 1.037 m

s8: 1.037 m

s9: 1.037 m

s10: 1.92 m

s11: 1.92 m

s12: 1.92 m

s13: 1.92 m

s14: 1.52 m

s15: 1.52 m

s16: 1.52 m

Voltage [V]

Time [ns]
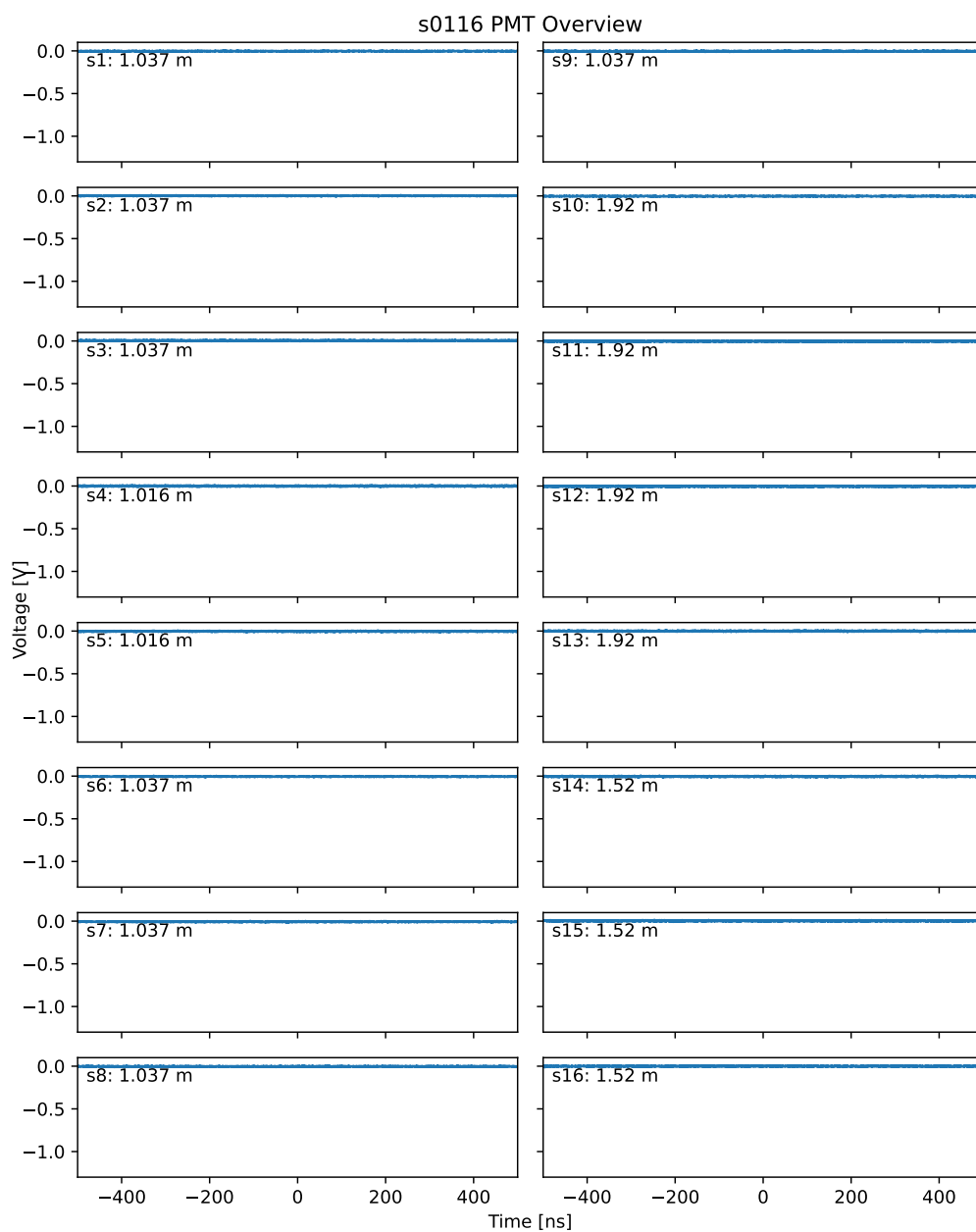
Figure 46. s0115: H$_2$ null shot.

Appendix B: Individual shot data: n-TOF

n-TOF $(x - t)$ plot for all DD and H$_2$ null shots. Test shot data are not included because there is no relevant time reference on these timescales. Scintillator PMT data are plotted from $t = 0$ (fusion event time) to 200 ns. Oscilloscope traces are vertically offset according to the distance from the target to the detector. Oscilloscope peaks are located, defining the time of a 'hit'. These hits are plotted at the corresponding detector distance. The trajectory of an unscattered DD neutron is shown as a diagonal dashed grey line. The trajectory of an unscattered prompt gamma ray is shown as a diagonal dashed yellow line. The time errorbar on each datapoint represents the transit time spread of the scintillator PMTs. The position errorbar on each datapoint represents the maximum and minimum distance of the scintillator slabs to the source. The error band on the 2.45 MeV neutron line represents the notional uncertainty in the temporal offset of the ionisation pin signal from the fusion event.
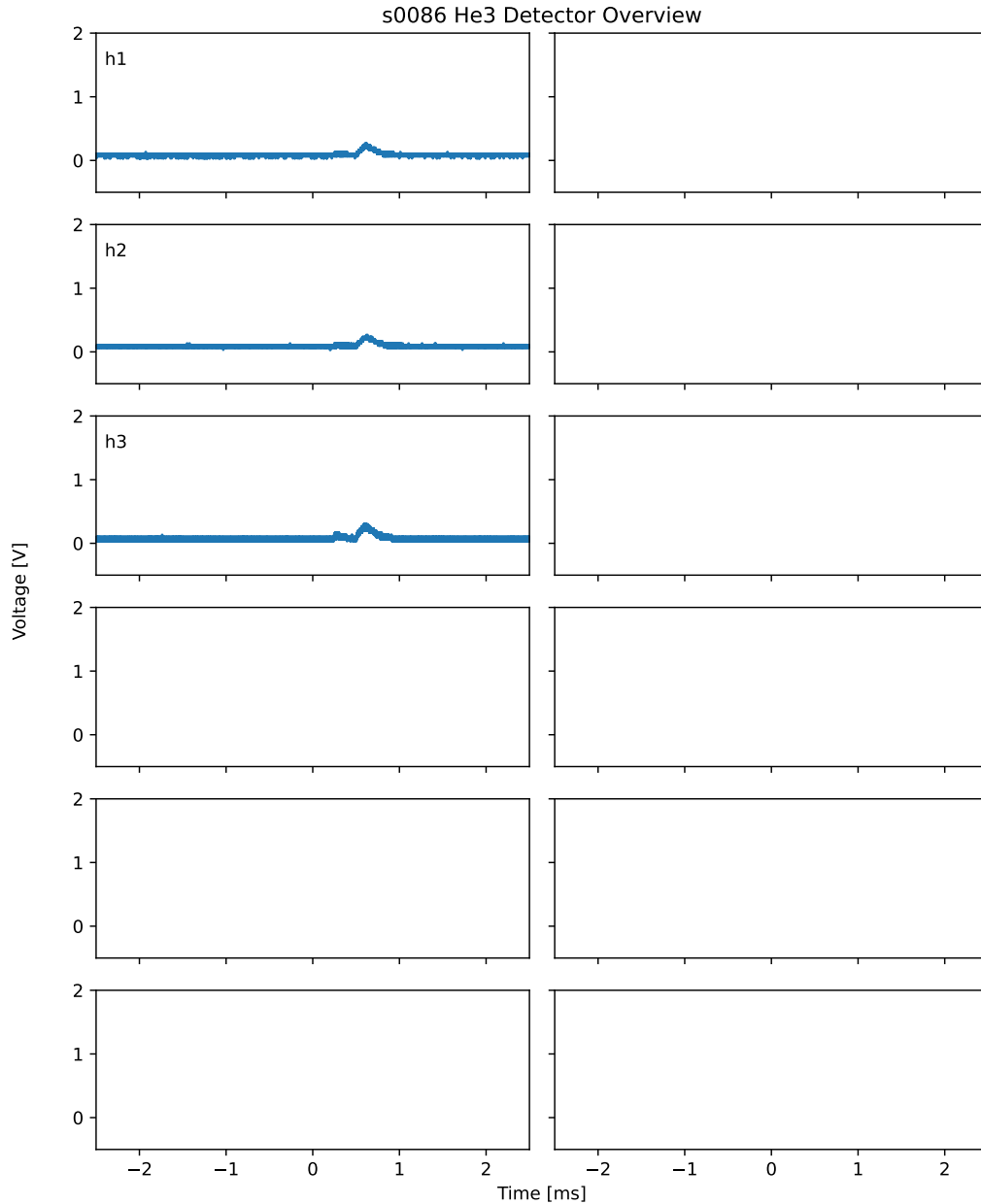

Figure 47. s0086: DD shot.
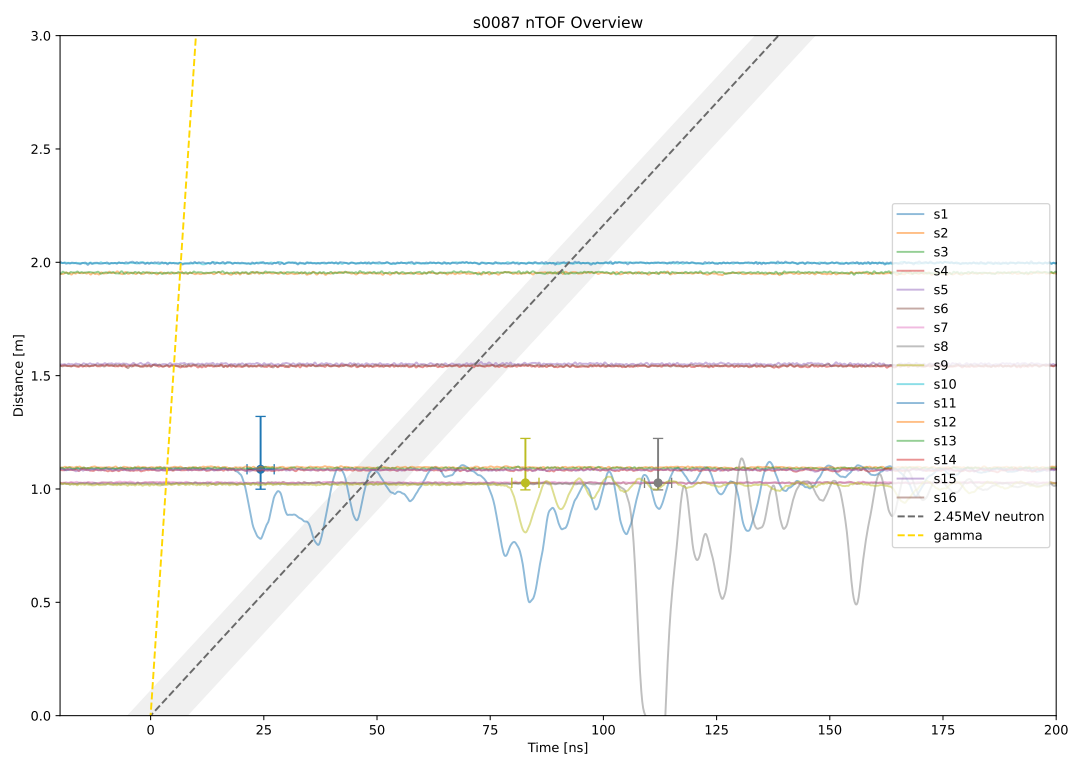
Figure 48. s0087: DD shot.
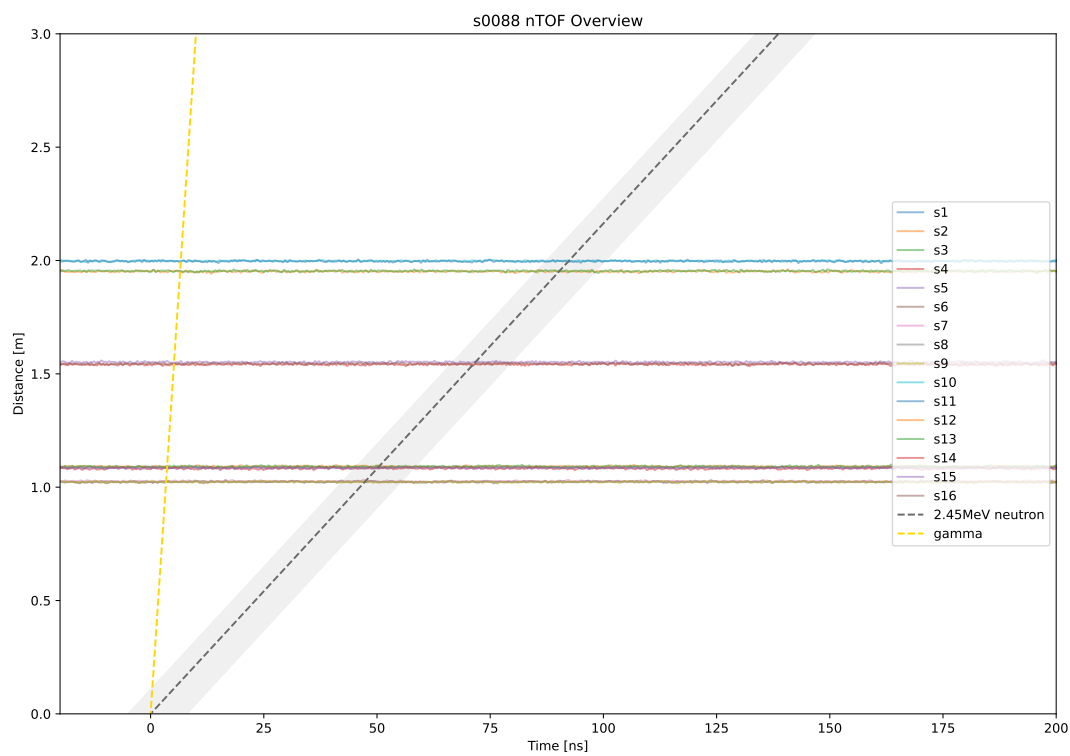
Figure 49. s0088: H$_2$ null shot.
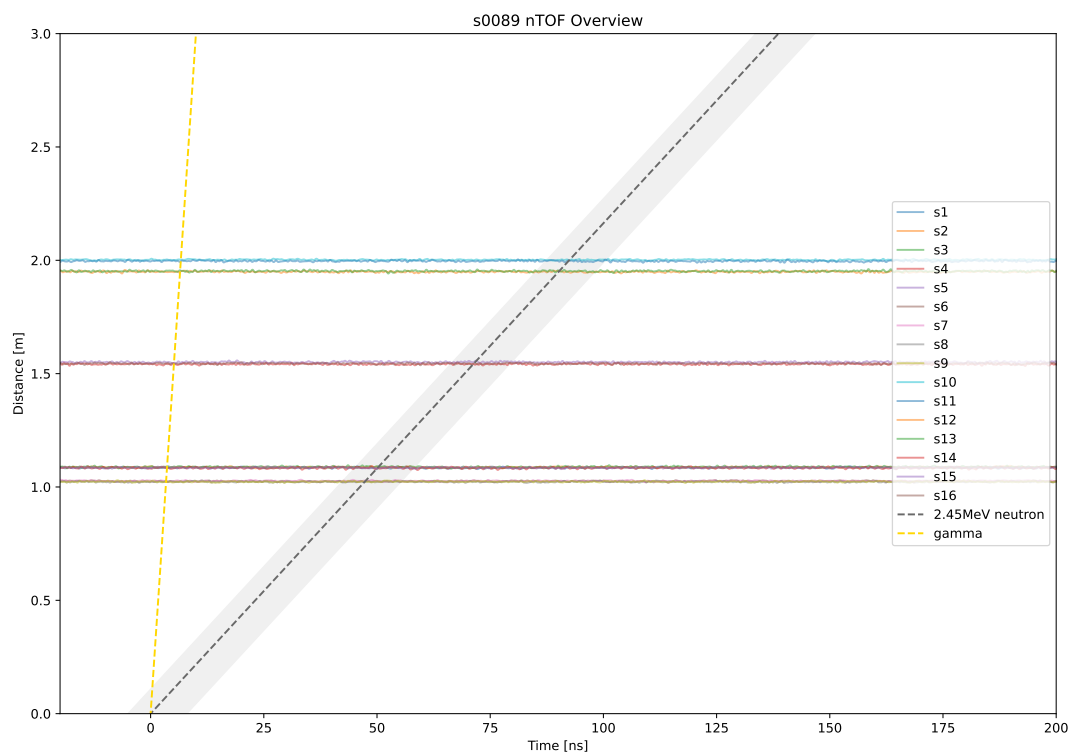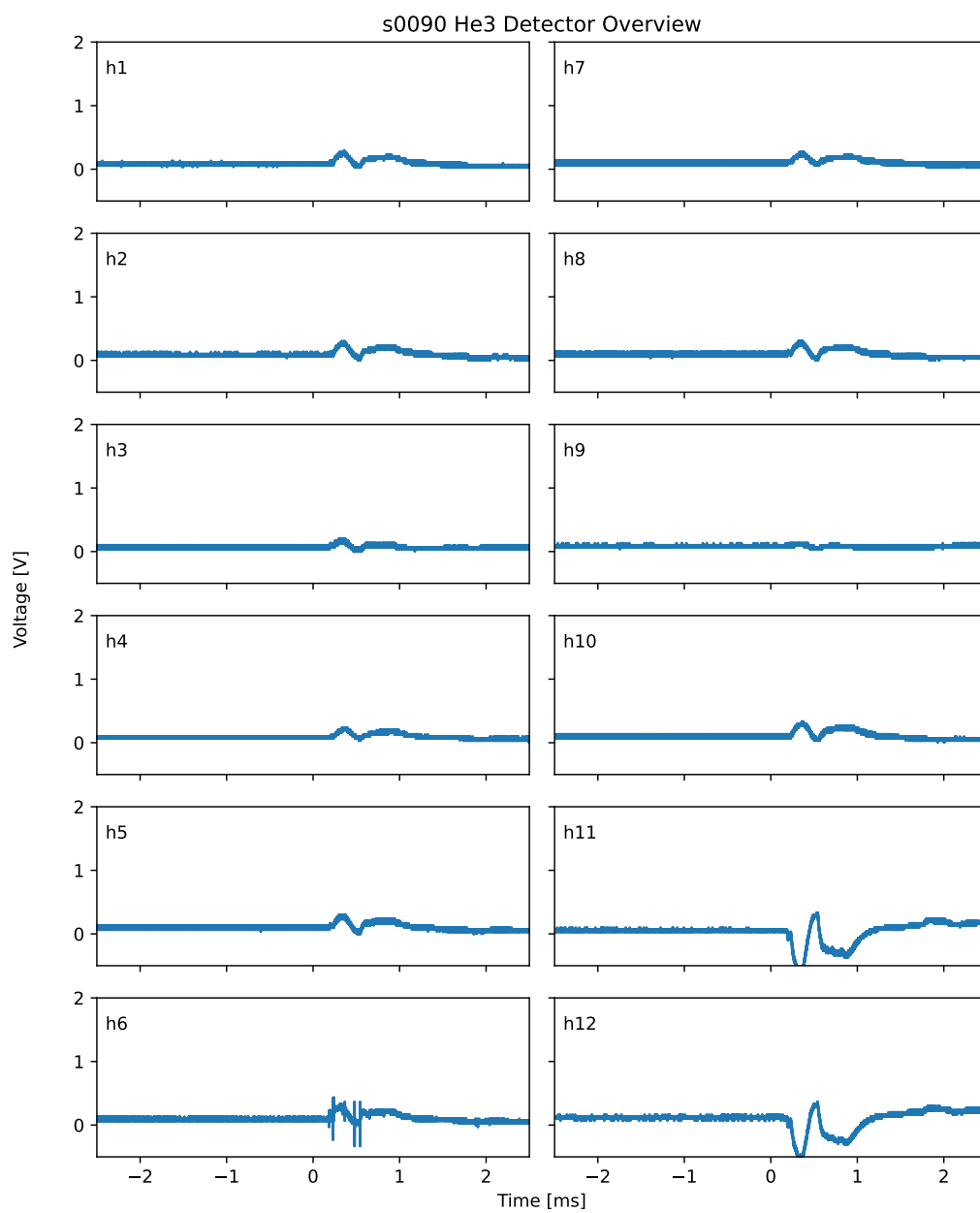
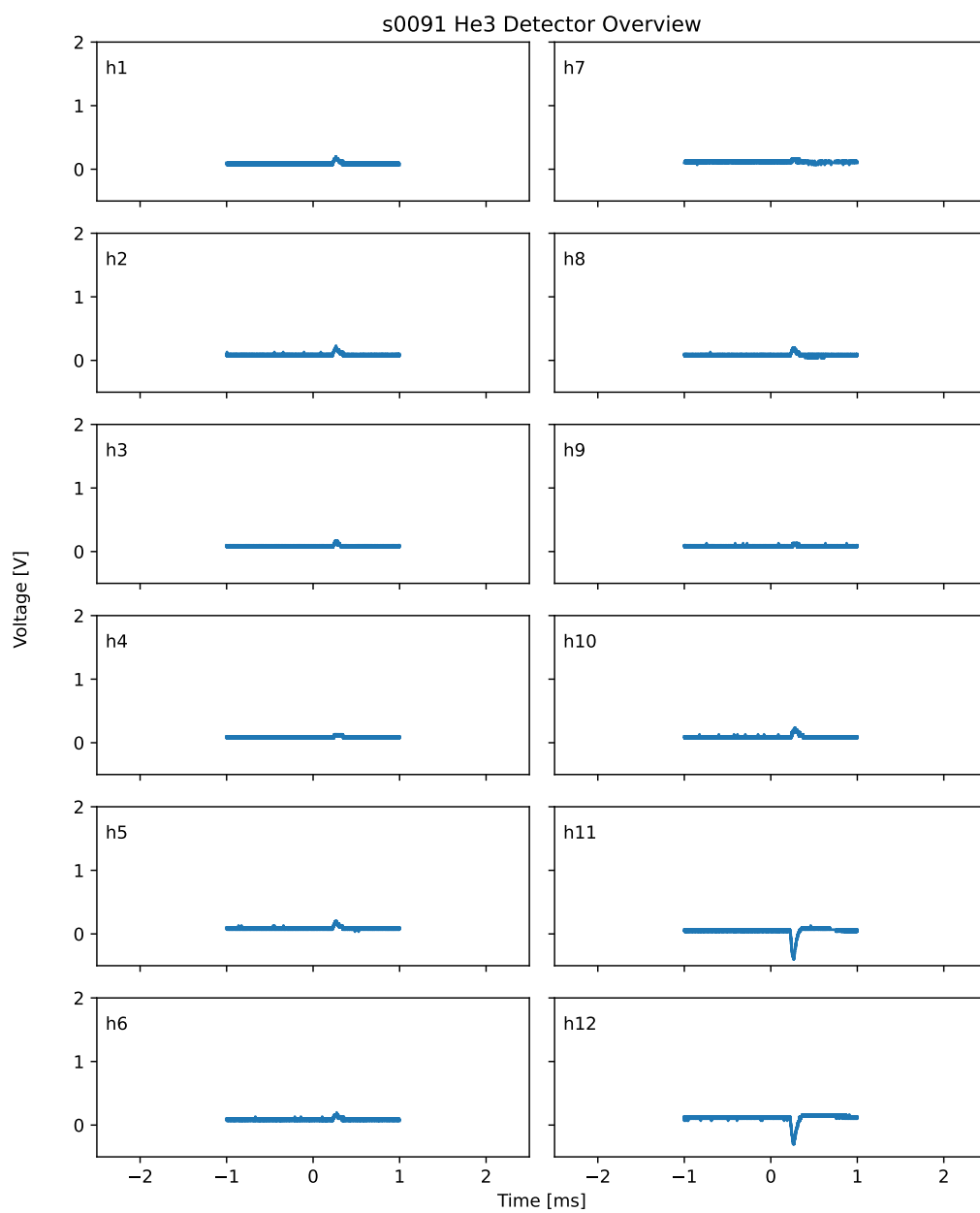Figure 50. s0089: H_2 null shot.
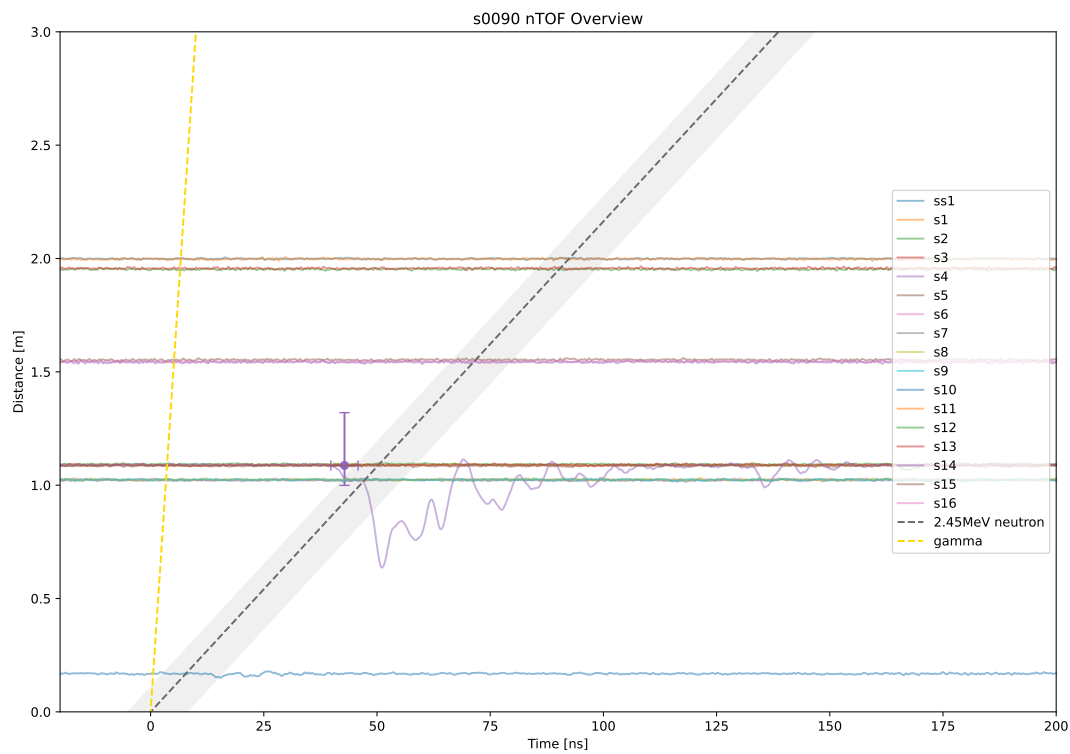
Figure 51. s0090: DD shot.
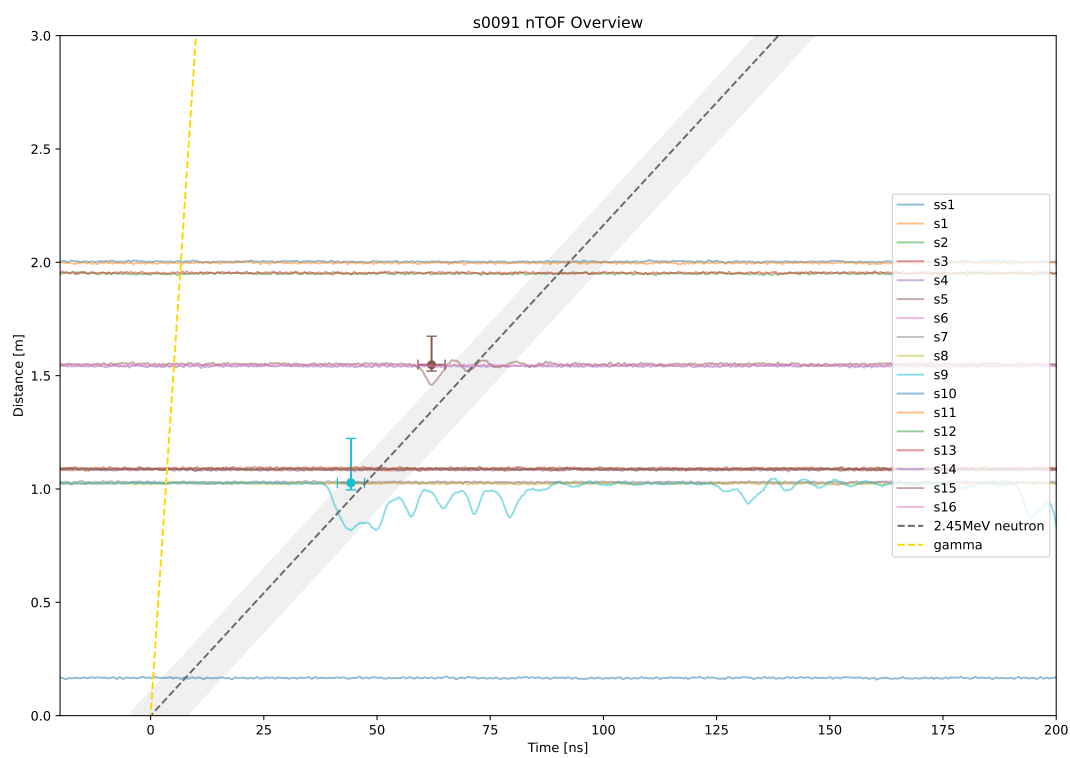
Figure 52. s0091: DD shot.
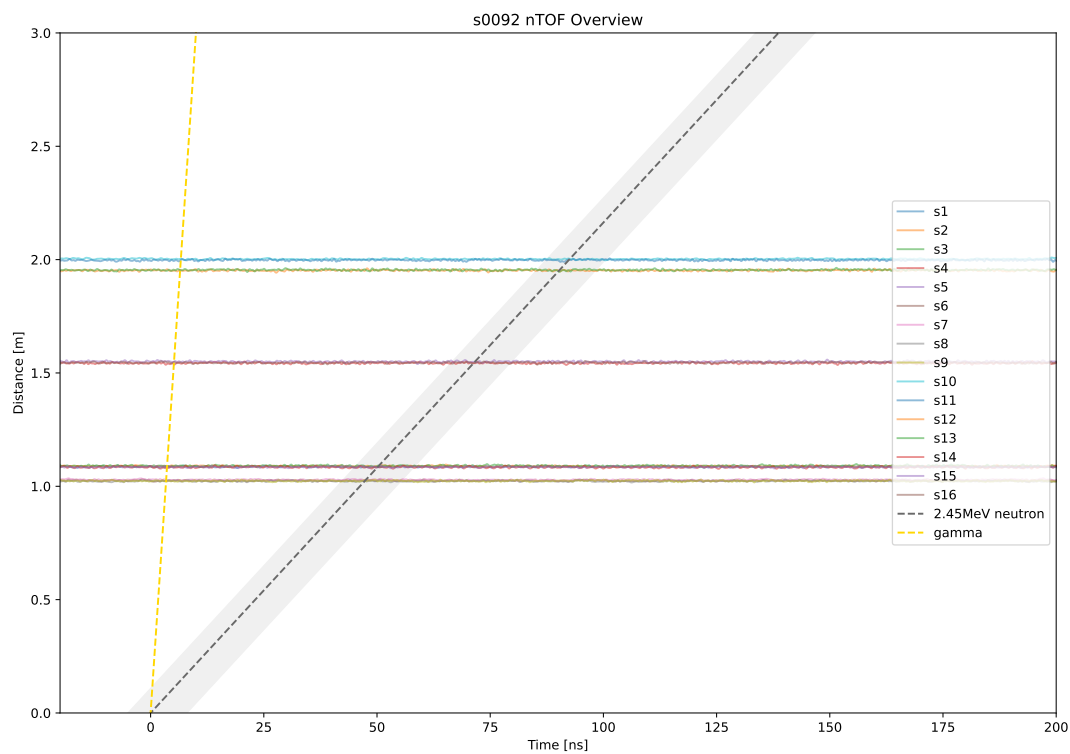
Figure 53. s0092: DD shot (projectile failure).
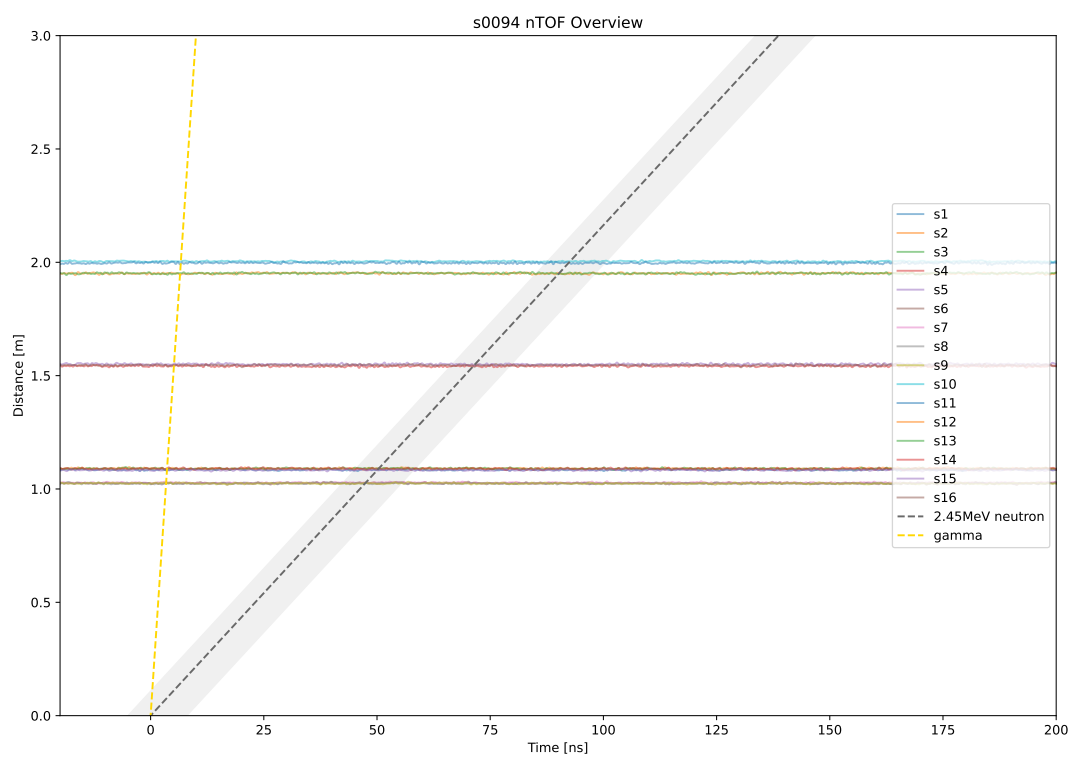
Figure 54. s0094: DD variant shot.
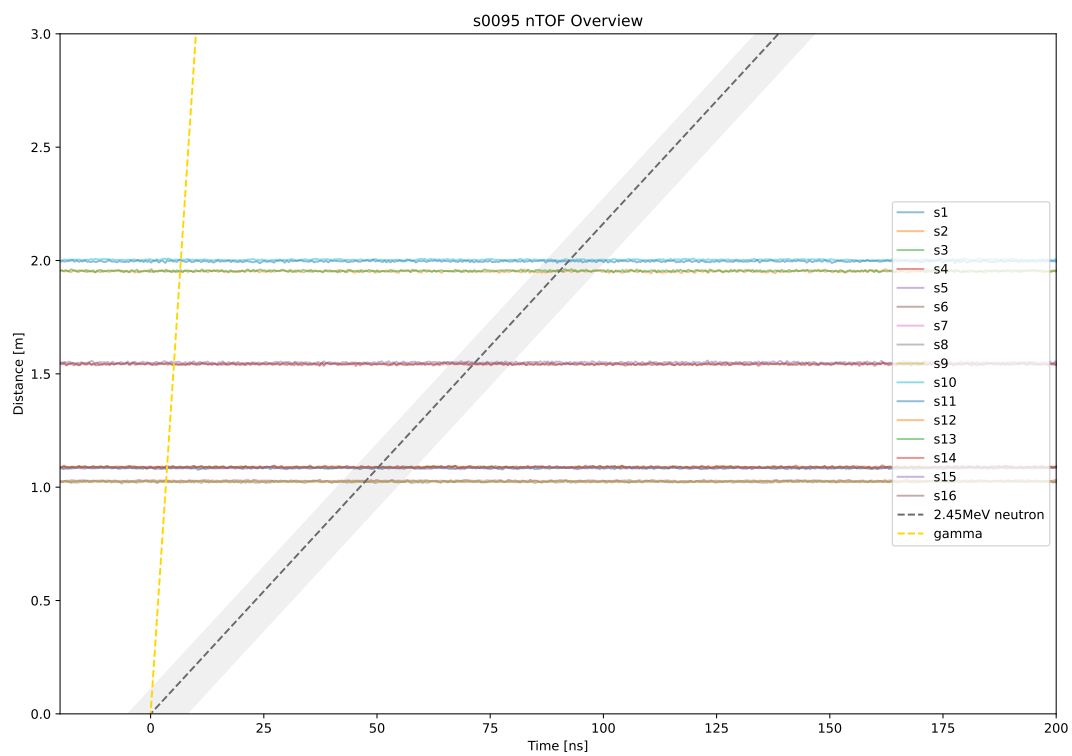
Figure 55. s0095: DD shot.
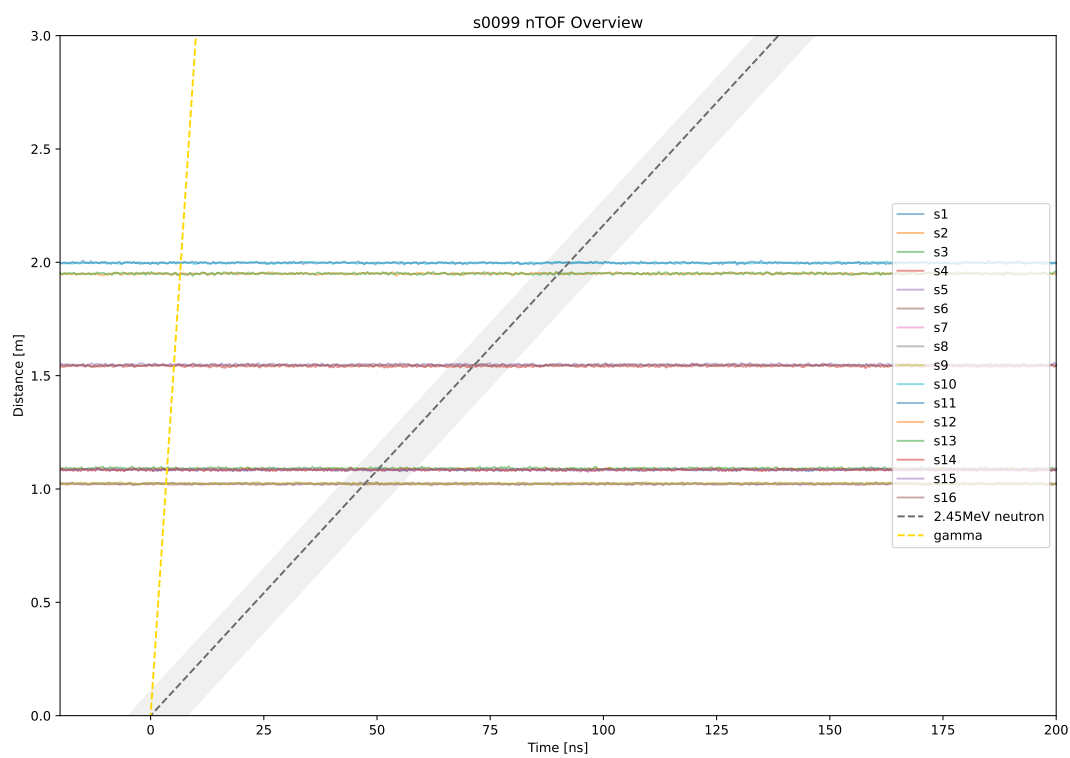
Figure 56. s0099: DD shot (mechanical target failure).
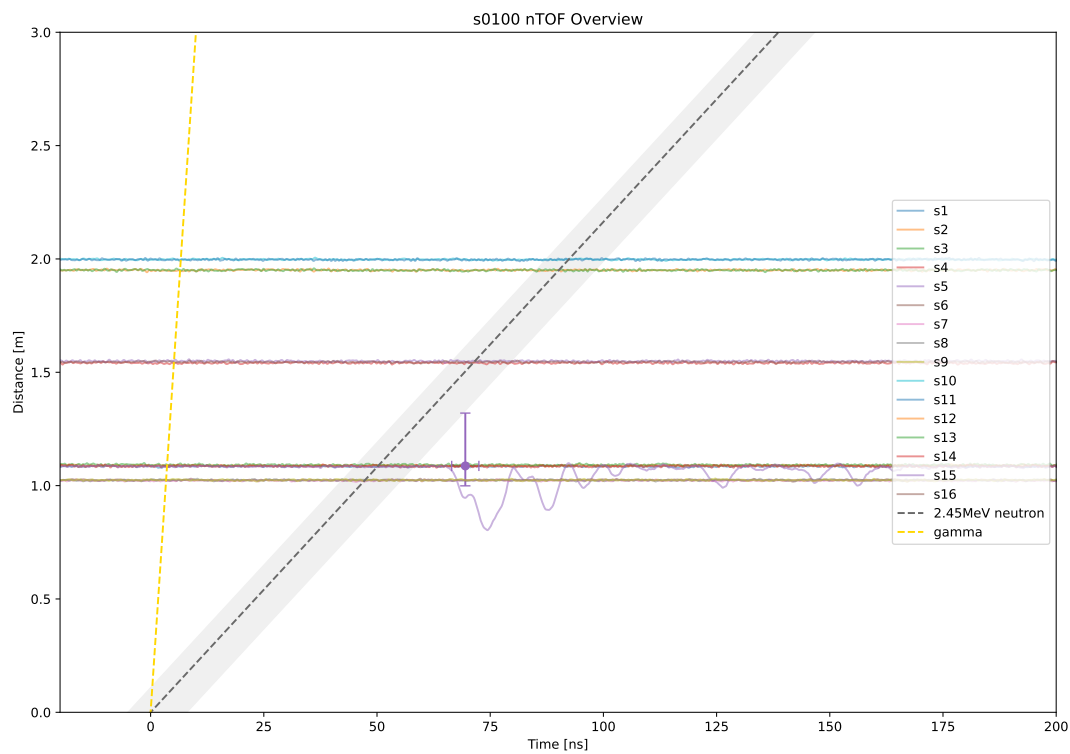
Figure 57. s0100: DD shot.
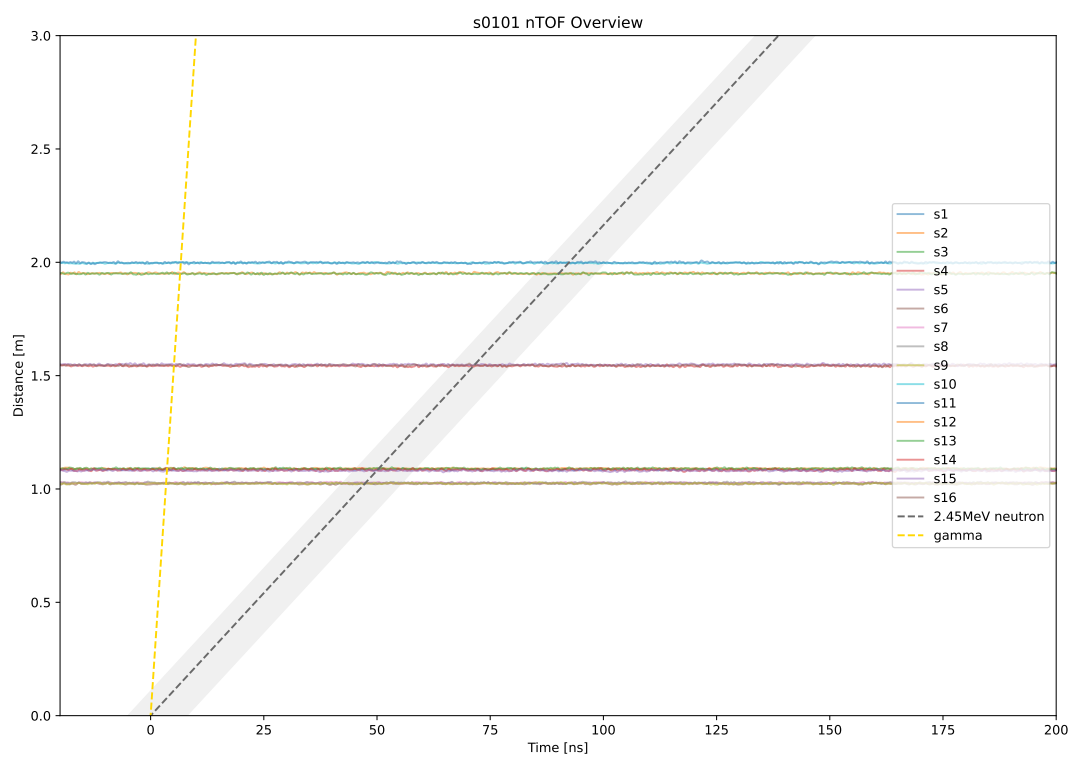
Figure 58. s0101: DD shot (mechanical target failure).
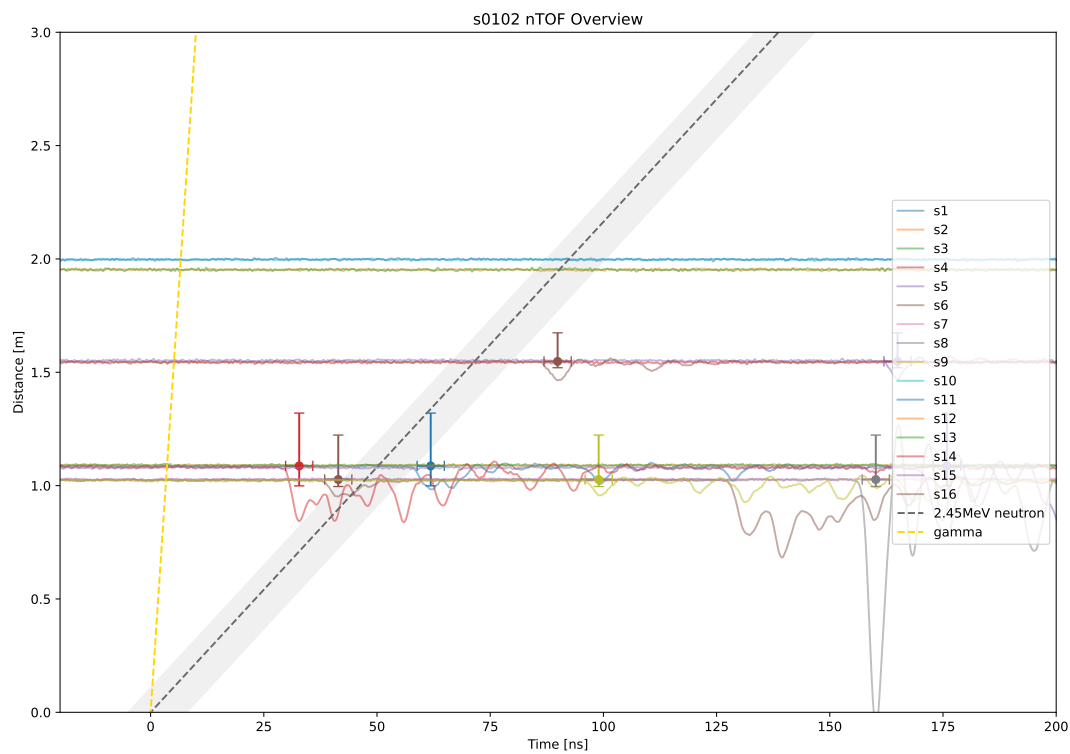
Figure 59. s0102: DD shot.
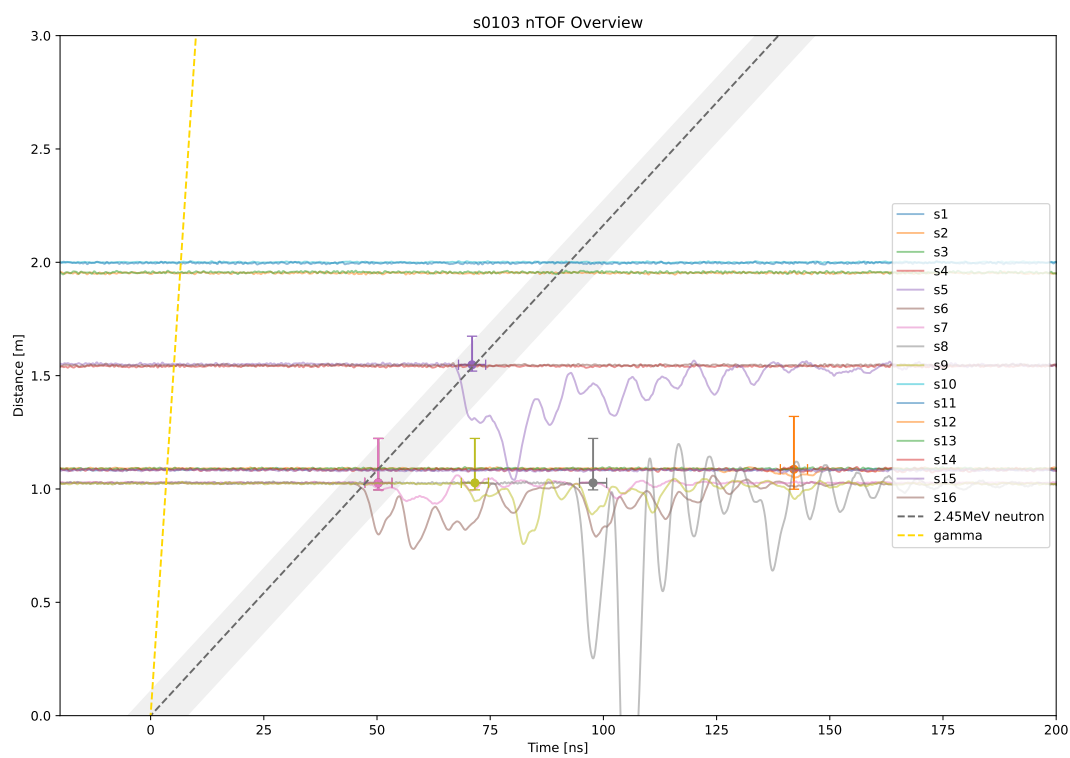
Figure 60. s0103: DD shot.
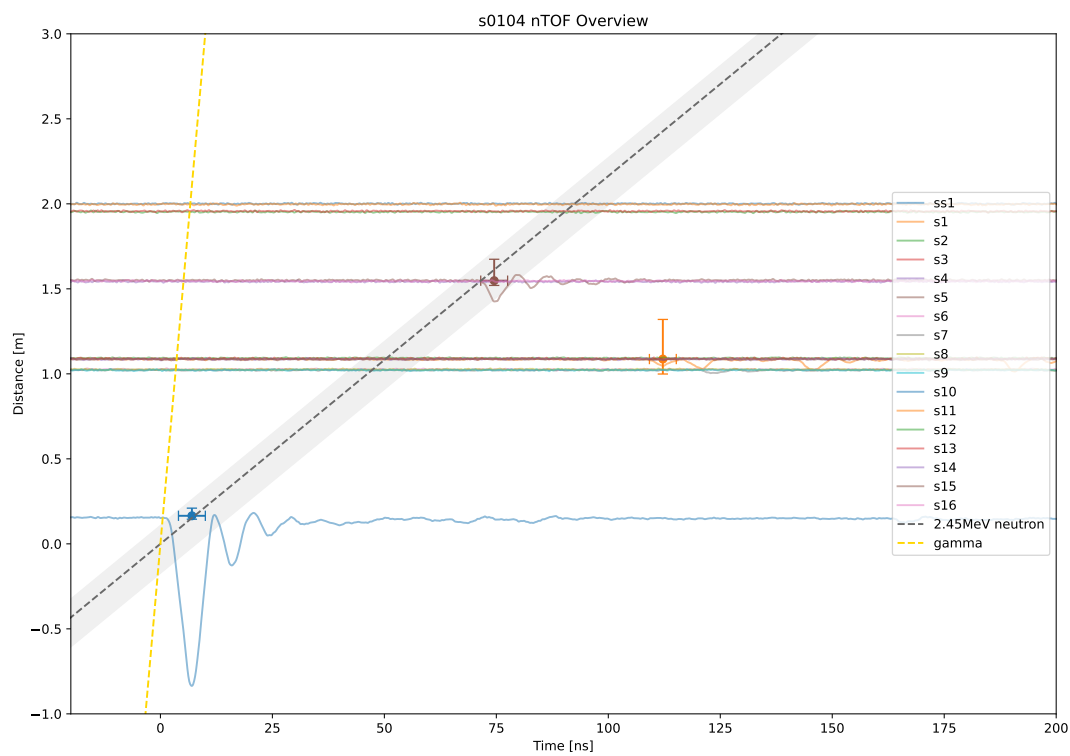
Figure 61. s0104: DD shot.
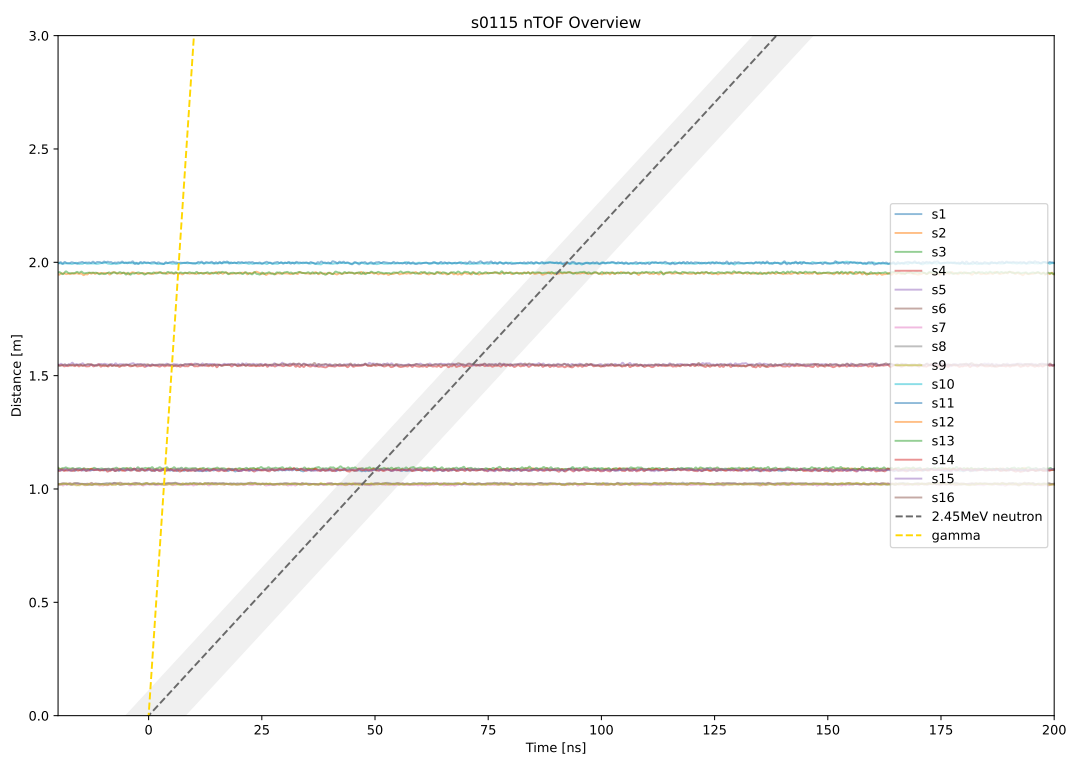
Figure 62. s0115: H_2 null shot.
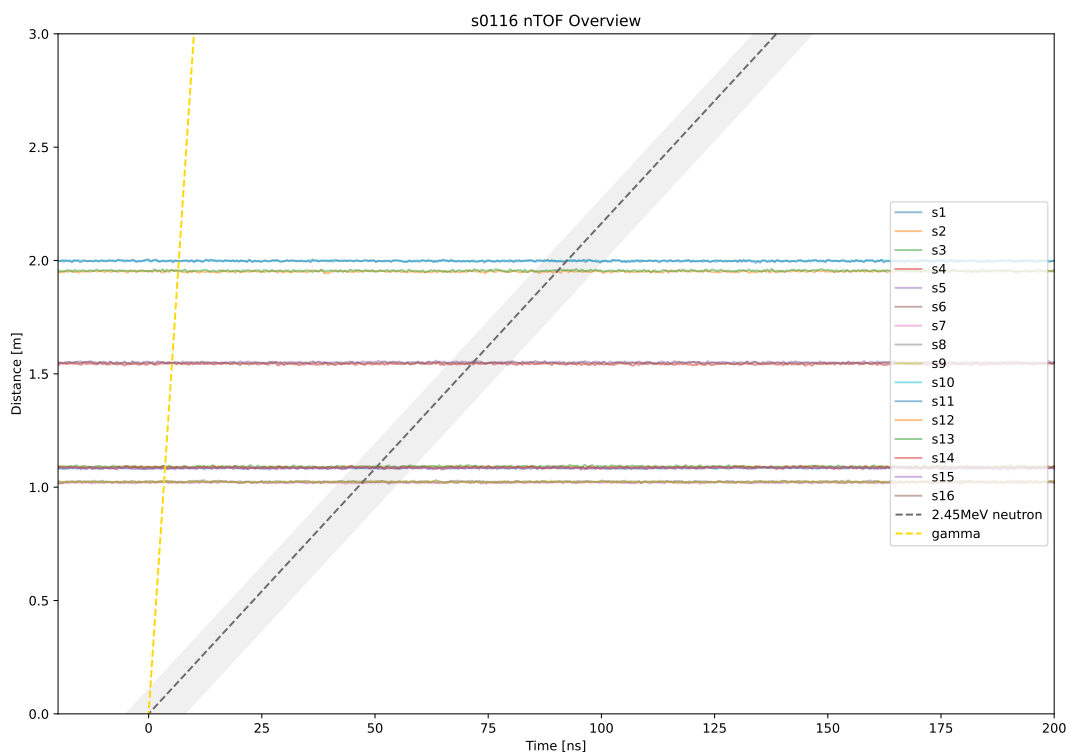
Figure 63. s0116: H_2 null shot.

Appendix C: Individual shot data: He-3 detectors

He-3 detector oscilloscope data for all experiments except s0097 (detectors not on). Oscilloscope channels monitor the combined TTL output from the 5 proportional counters within each detector. The timebase spans ±2.5 ms from the fusion event time. Test shot data are included because the uncertainty in the definition of t_0 is not relevant on these relatively long timescales. Note that on the time scale plotted the TTL pulse appears as a vertical straight line. Some of the shots exhibit a low voltage time varying signal at late time - this is caused by electrical noise in the mains ground following a gun shot.

Figure 64. s0086: DD shot.
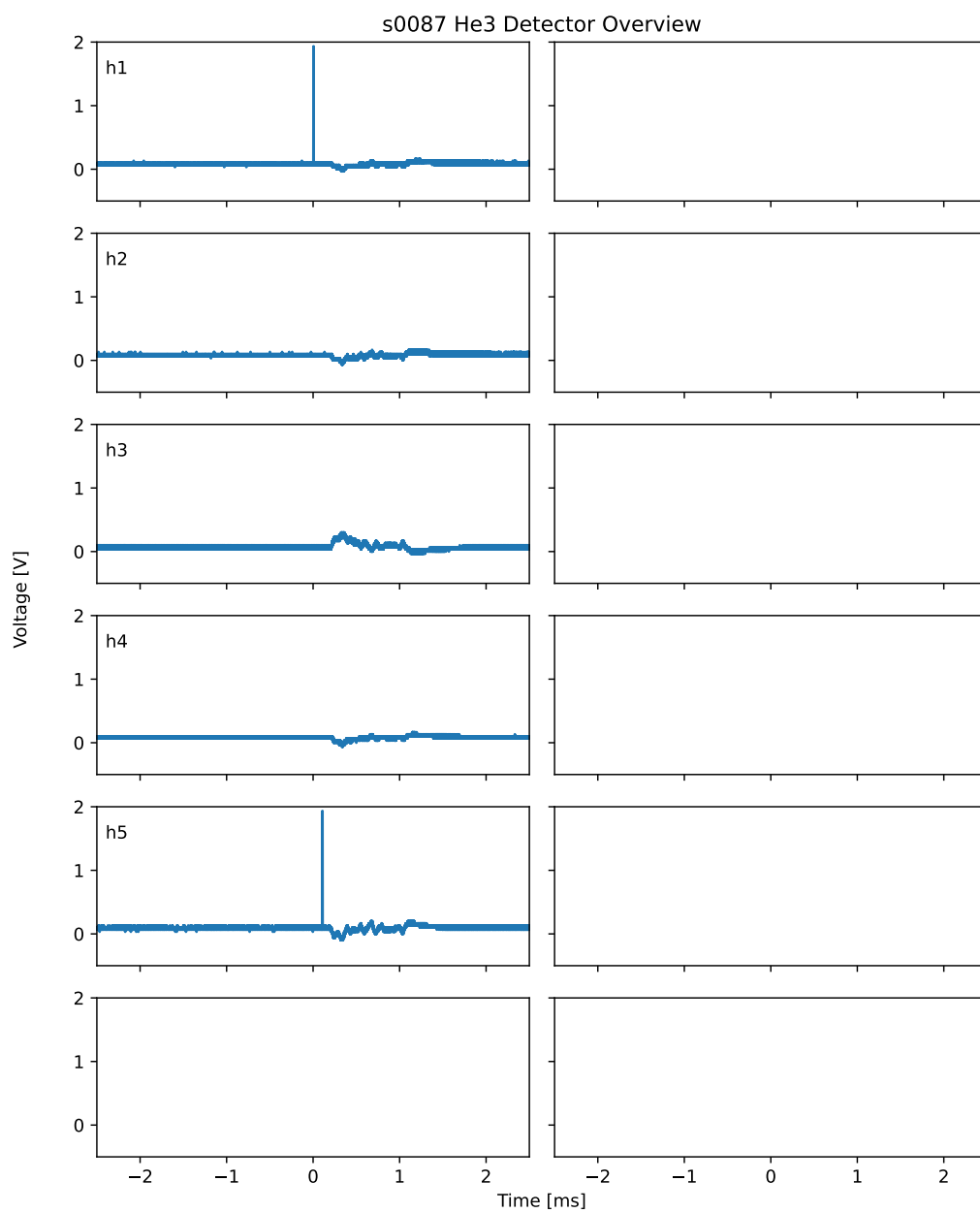
Figure 65. s0087: DD shot
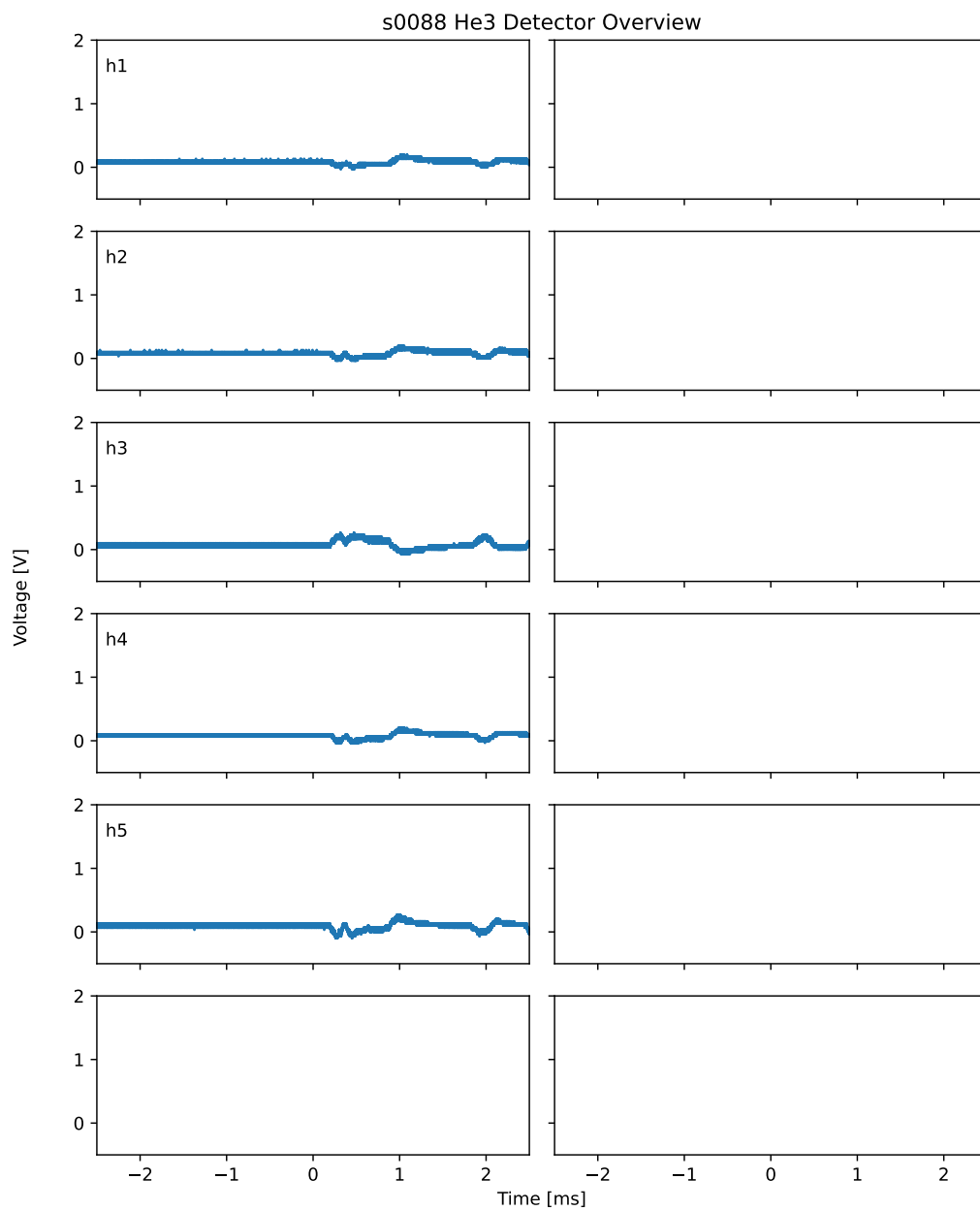
Figure 66. s0088: H$_2$ null shot
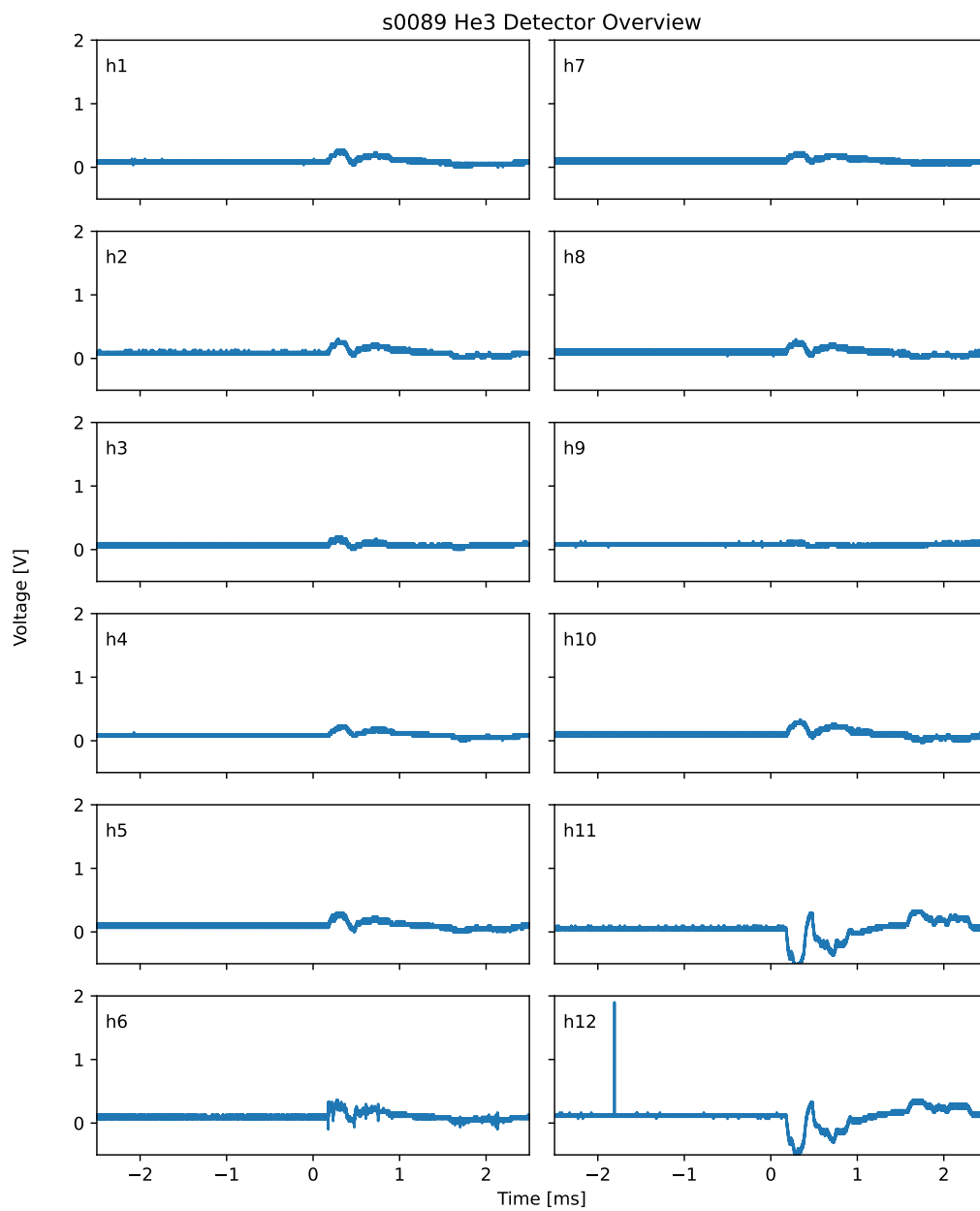
Figure 67. s0089: H$_2$ null shot.

Figure 68. s0090: DD shot.

s0091 He3 Detector Overview

Voltage [V]

Time [ms]

Figure 69. s0091: DD shot.
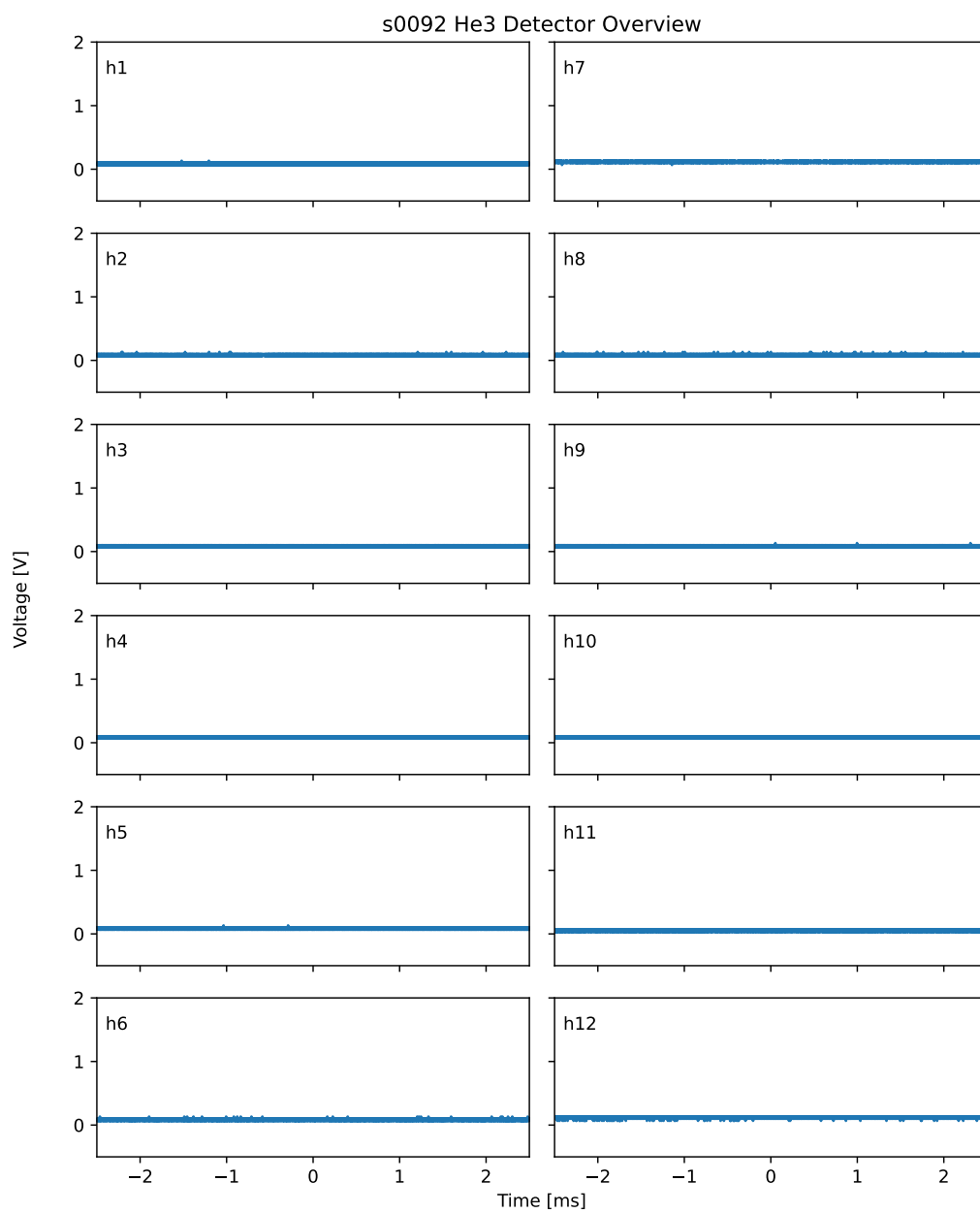
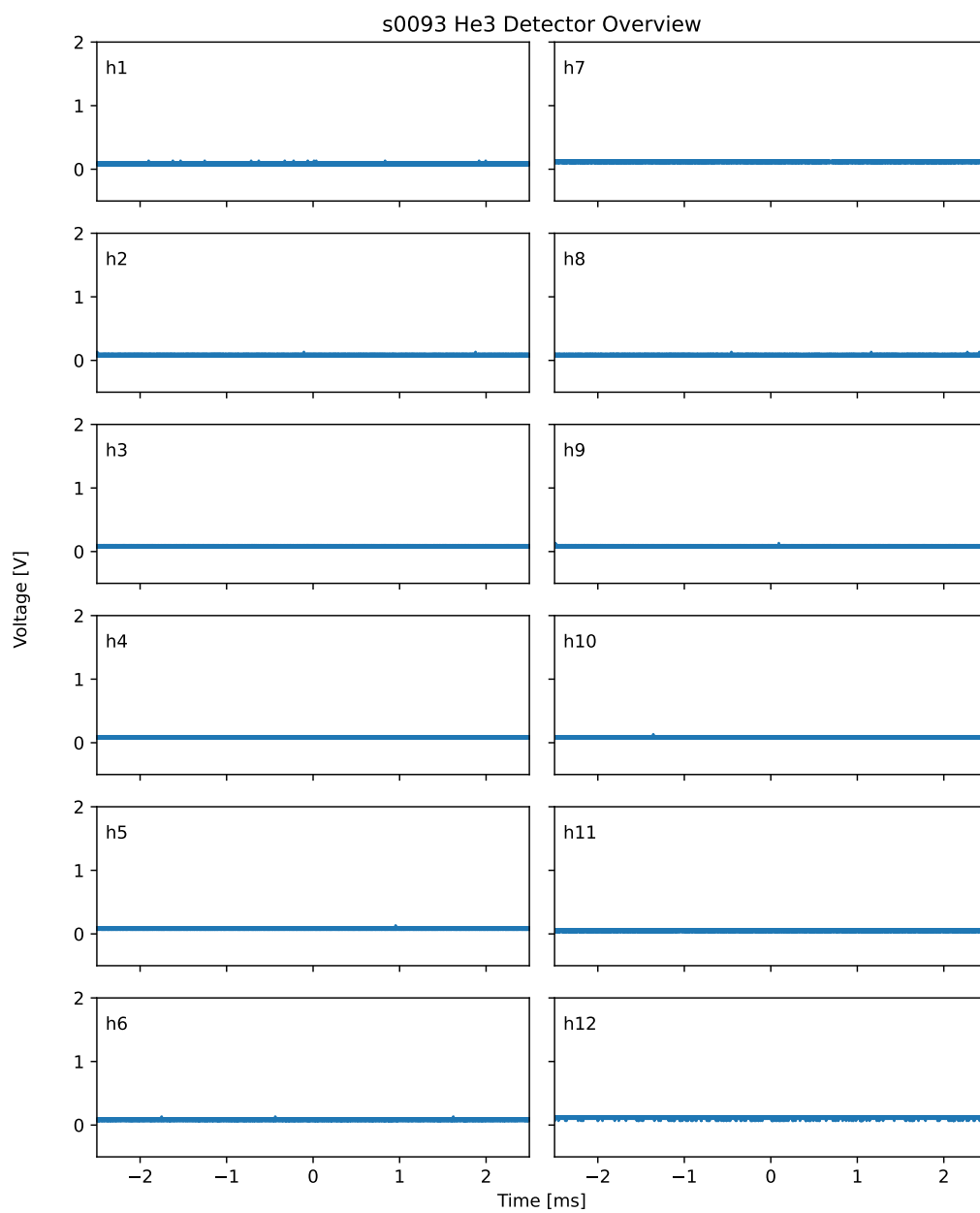Figure 70. s0092: DD shot (projectile failure).
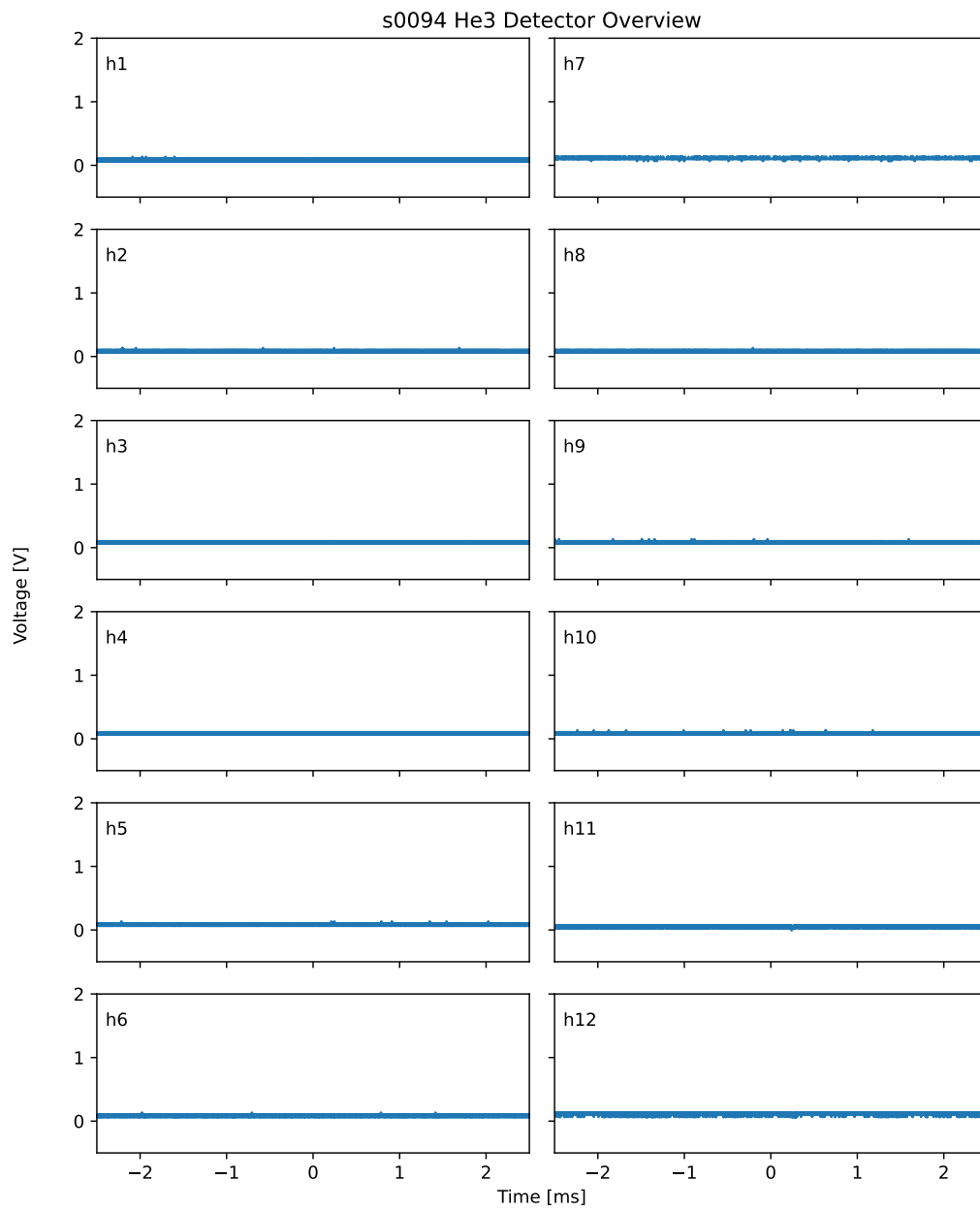
Figure 71. s0093: test shot.
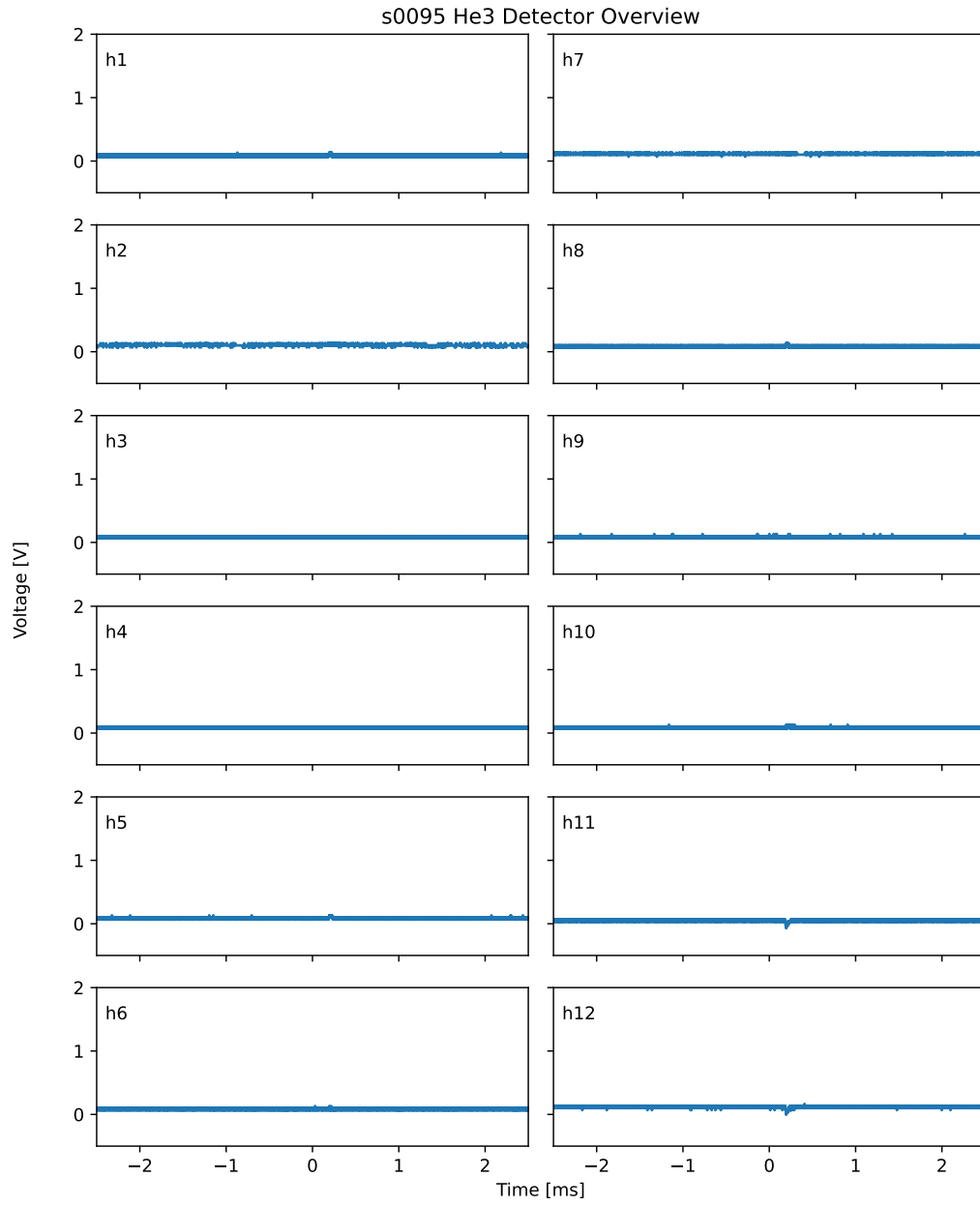
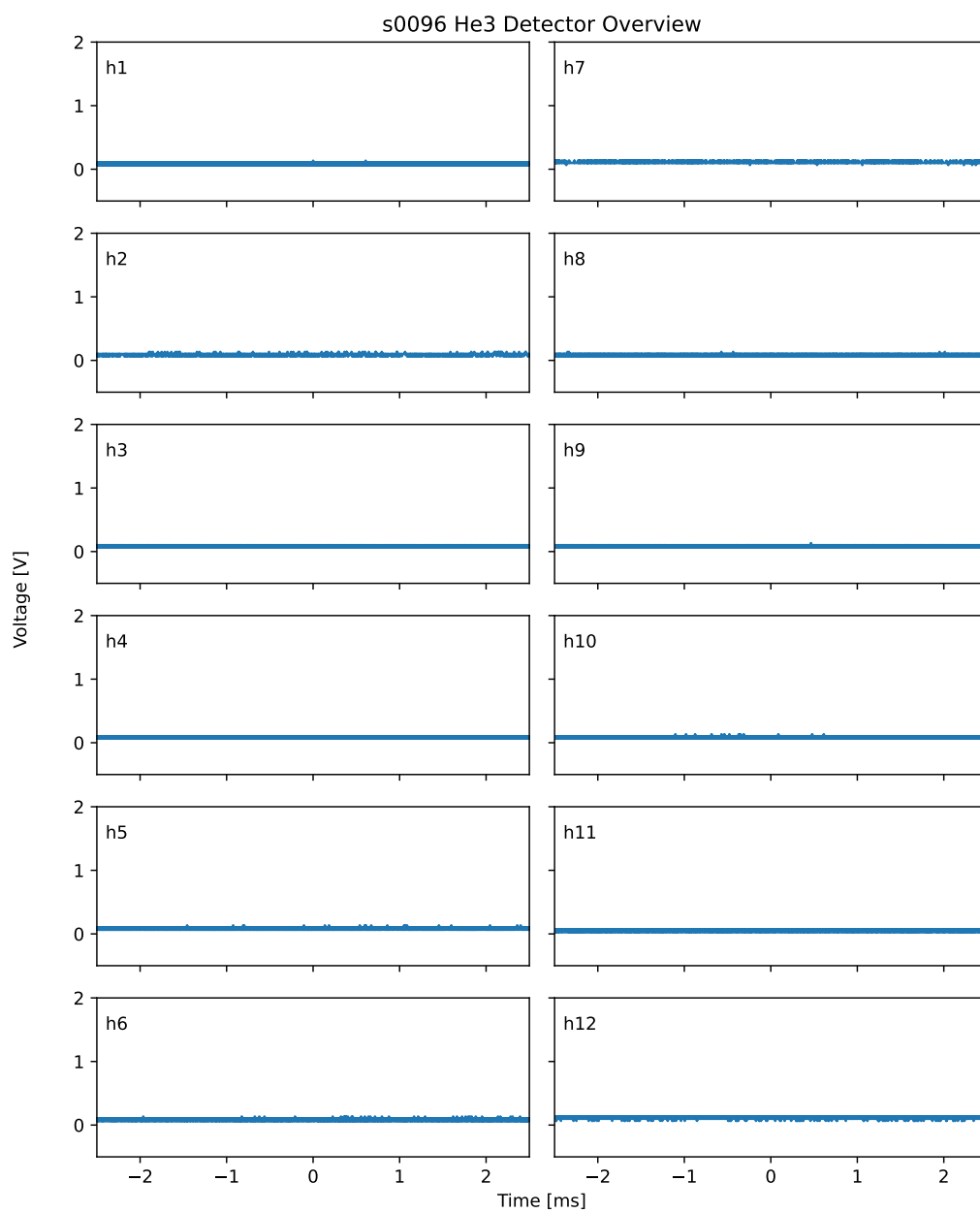Figure 72. s0094: DD variant shot.

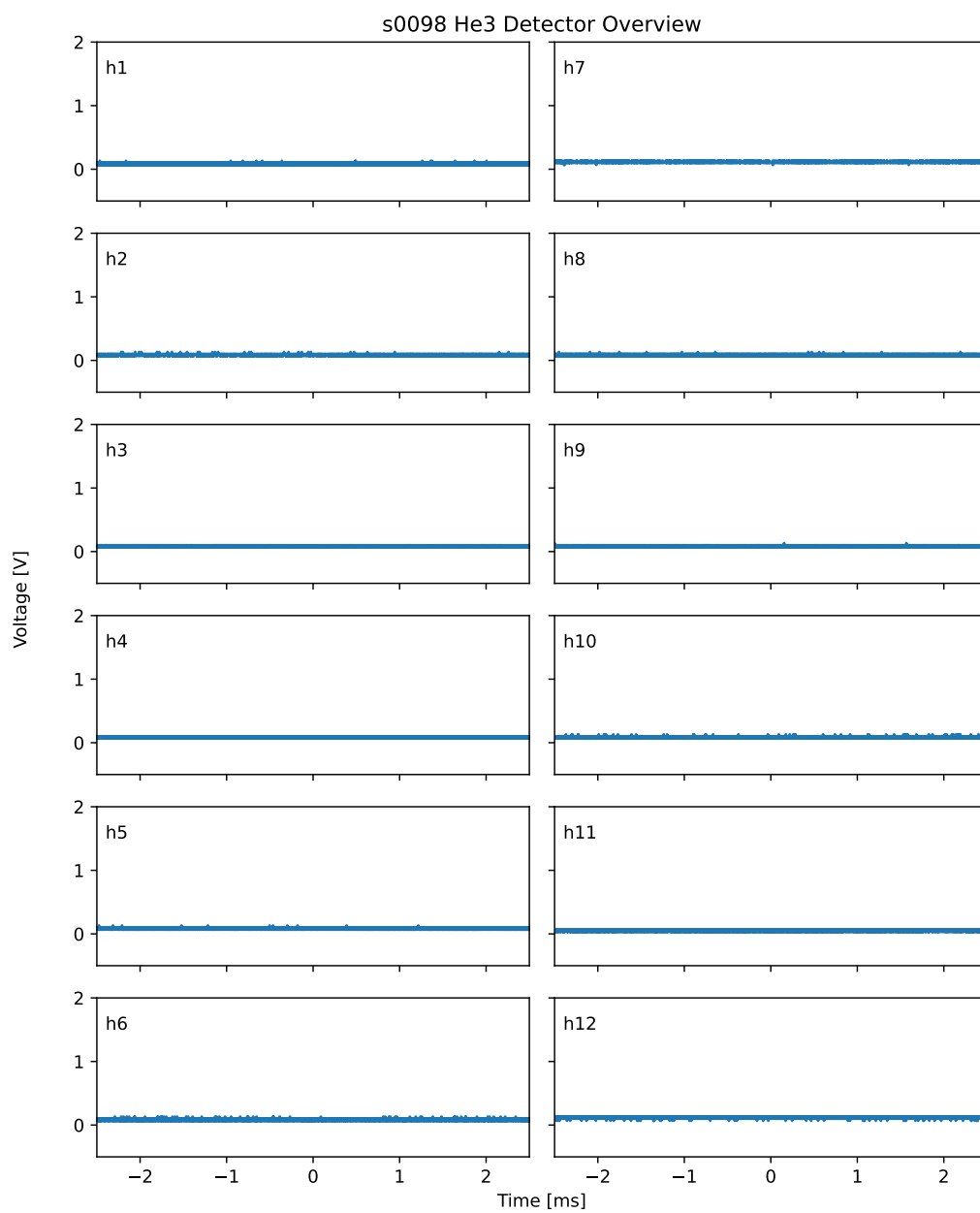Figure 73. s0095: DD shot

Figure 74. s0096: test shot.
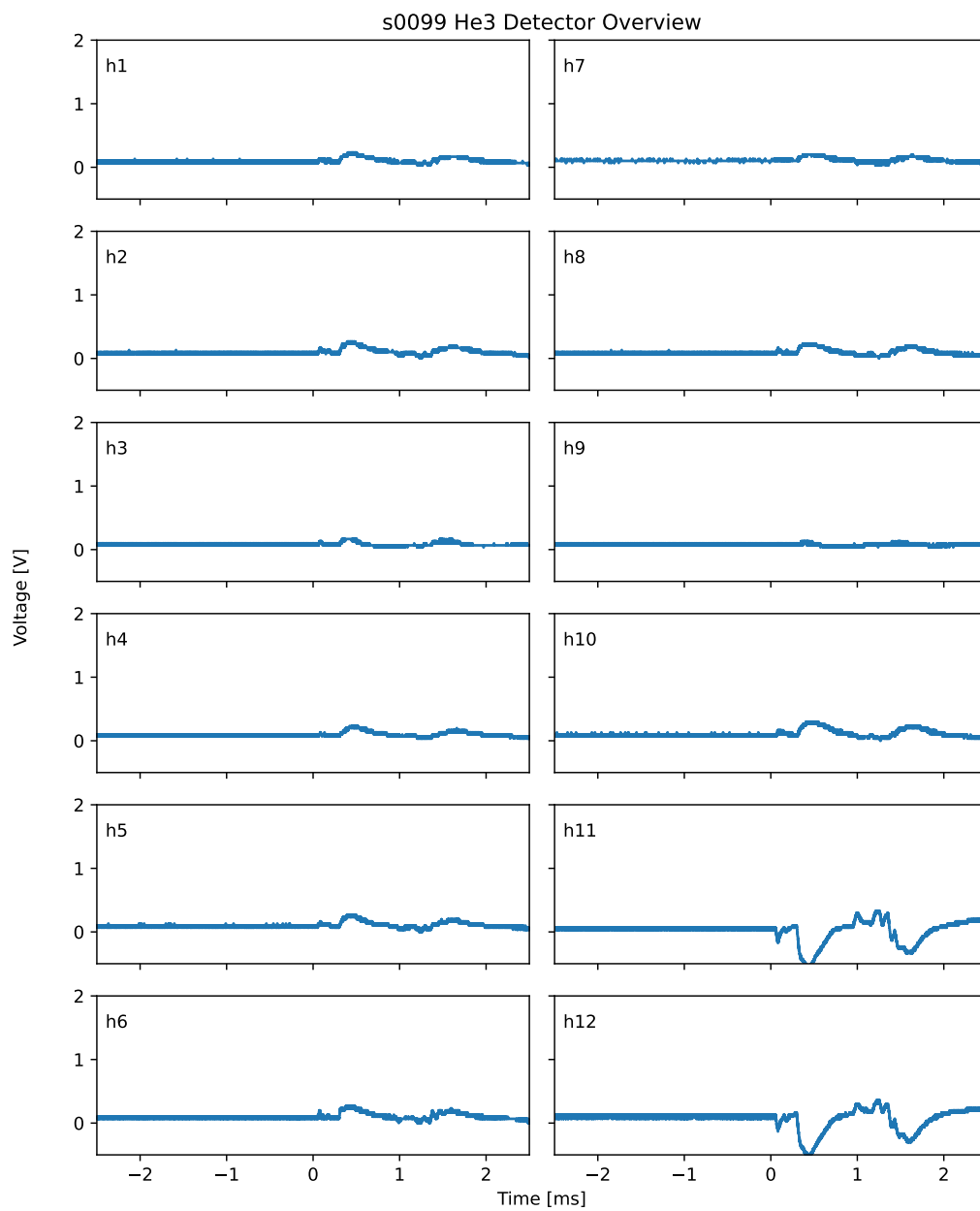
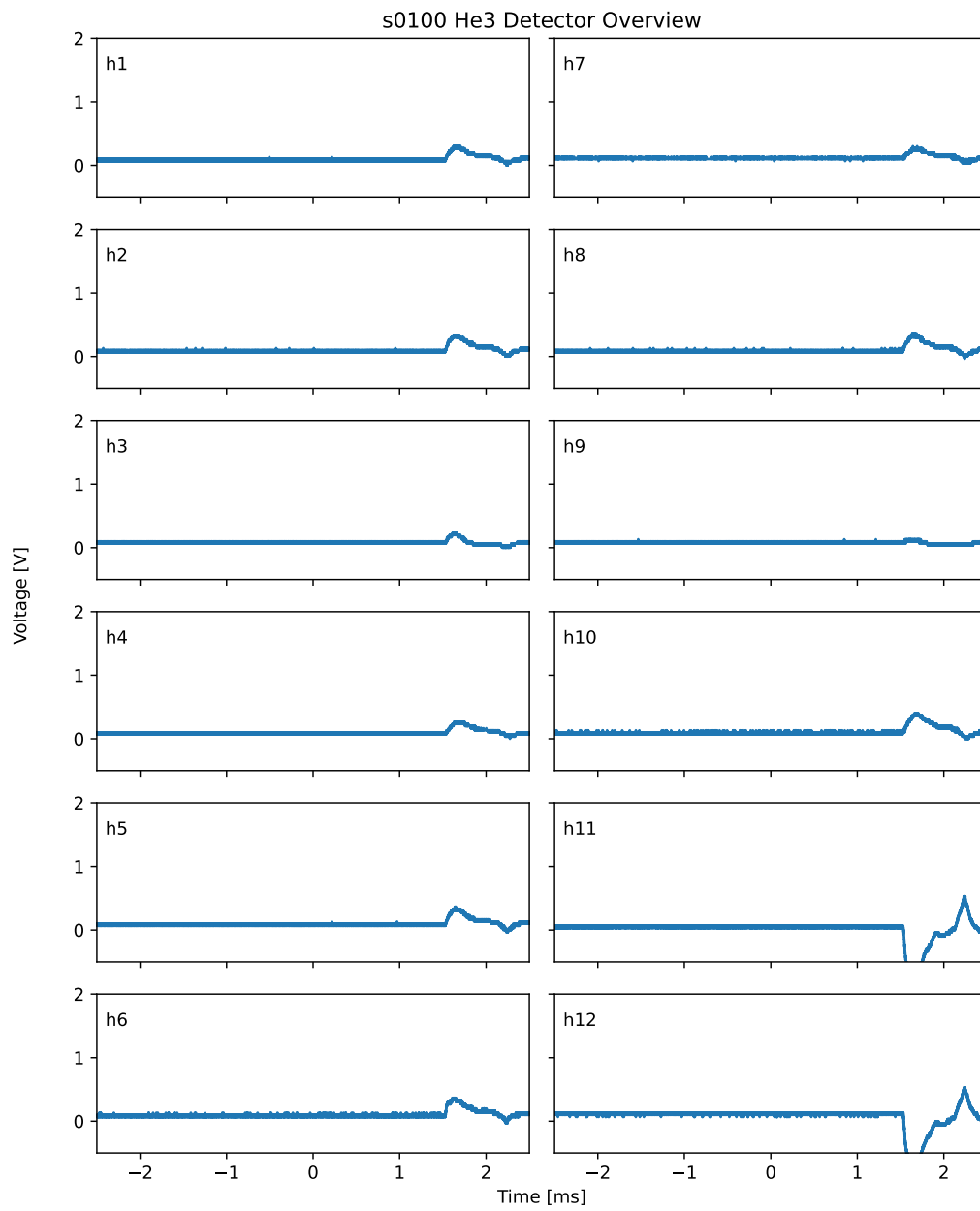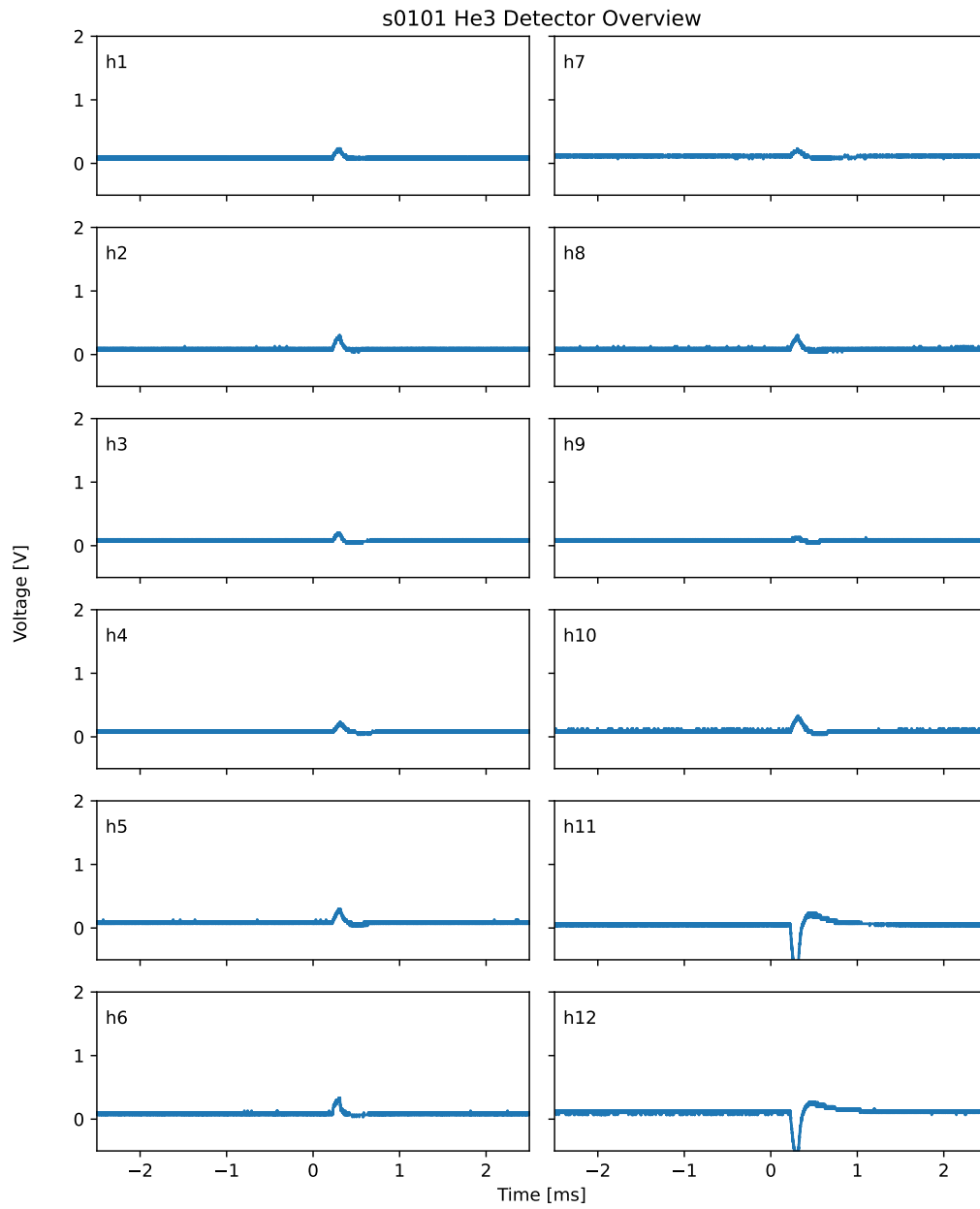Figure 75. s0098: test shot.

Figure 76. s0099: DD shot (mechanical target failure).

Figure 77. s0100: DD shot.

Figure 78. s0101: DD shot (mechanical target failure).

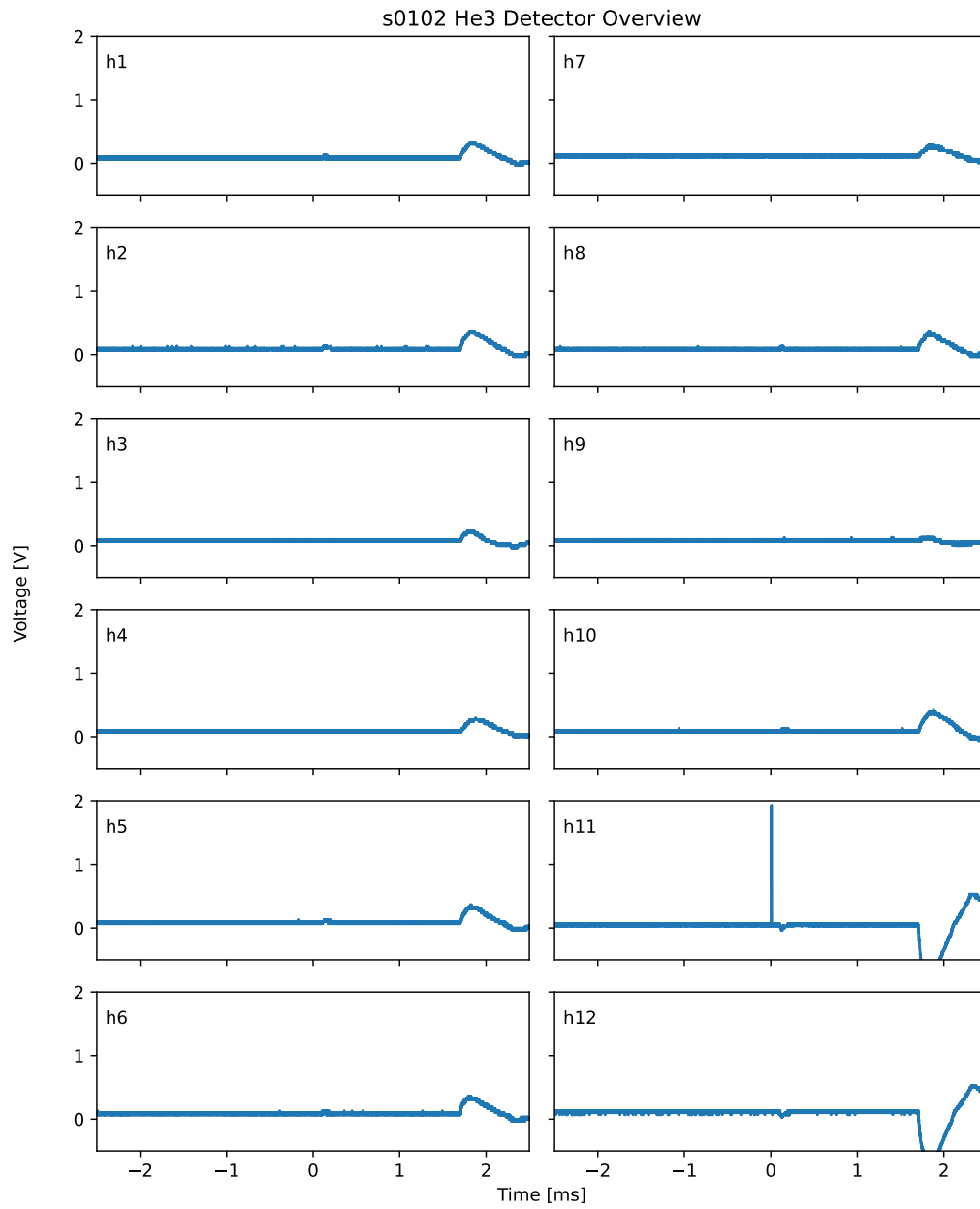s0102 He3 Detector Overview

h1

h7

h2

h8

h3

h9

h4

h10

h5

h11

h6

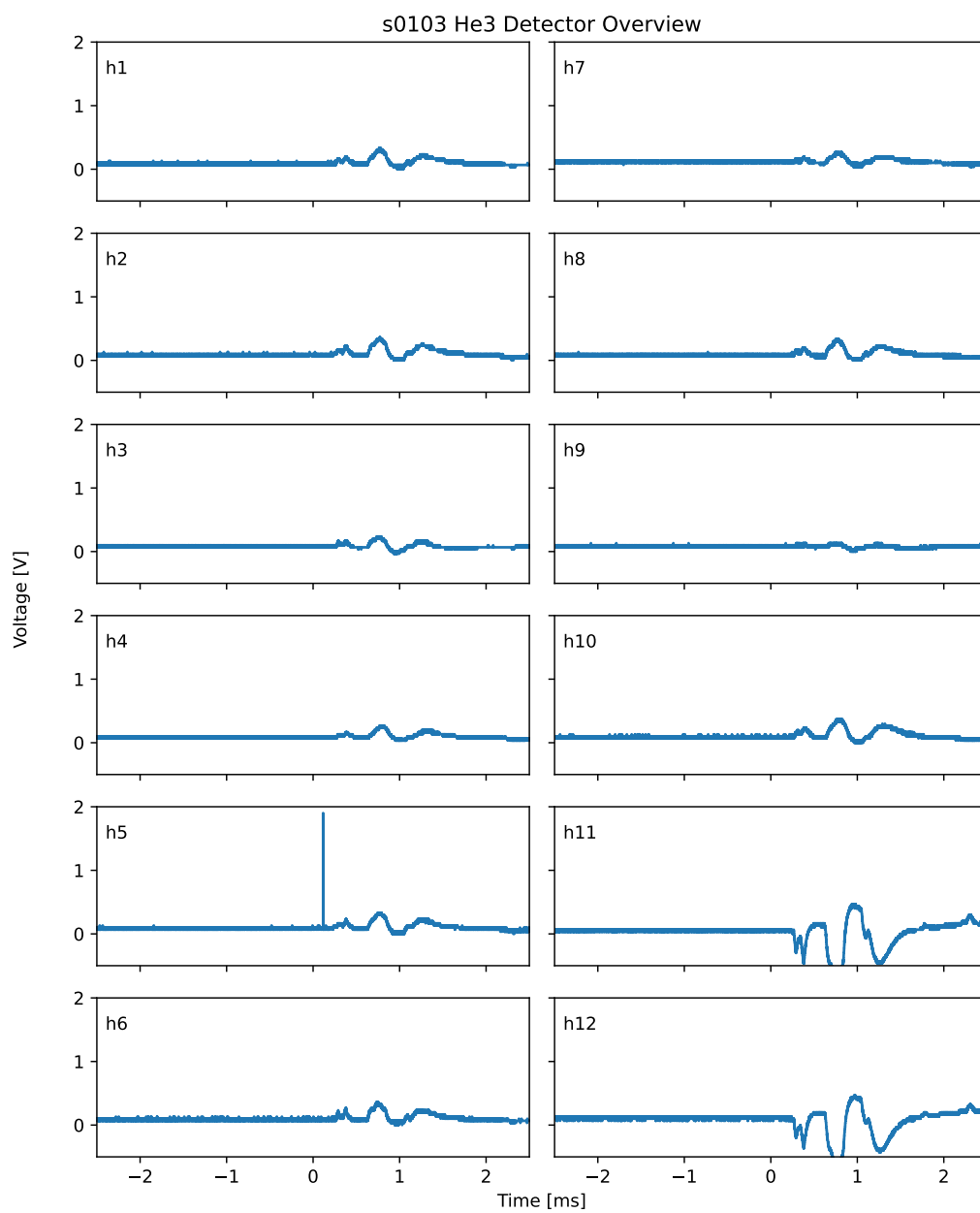h12

Voltage [V]

Time [ms]

Figure 79. s0102: DD shot.

Figure 80. s0103: DD shot.
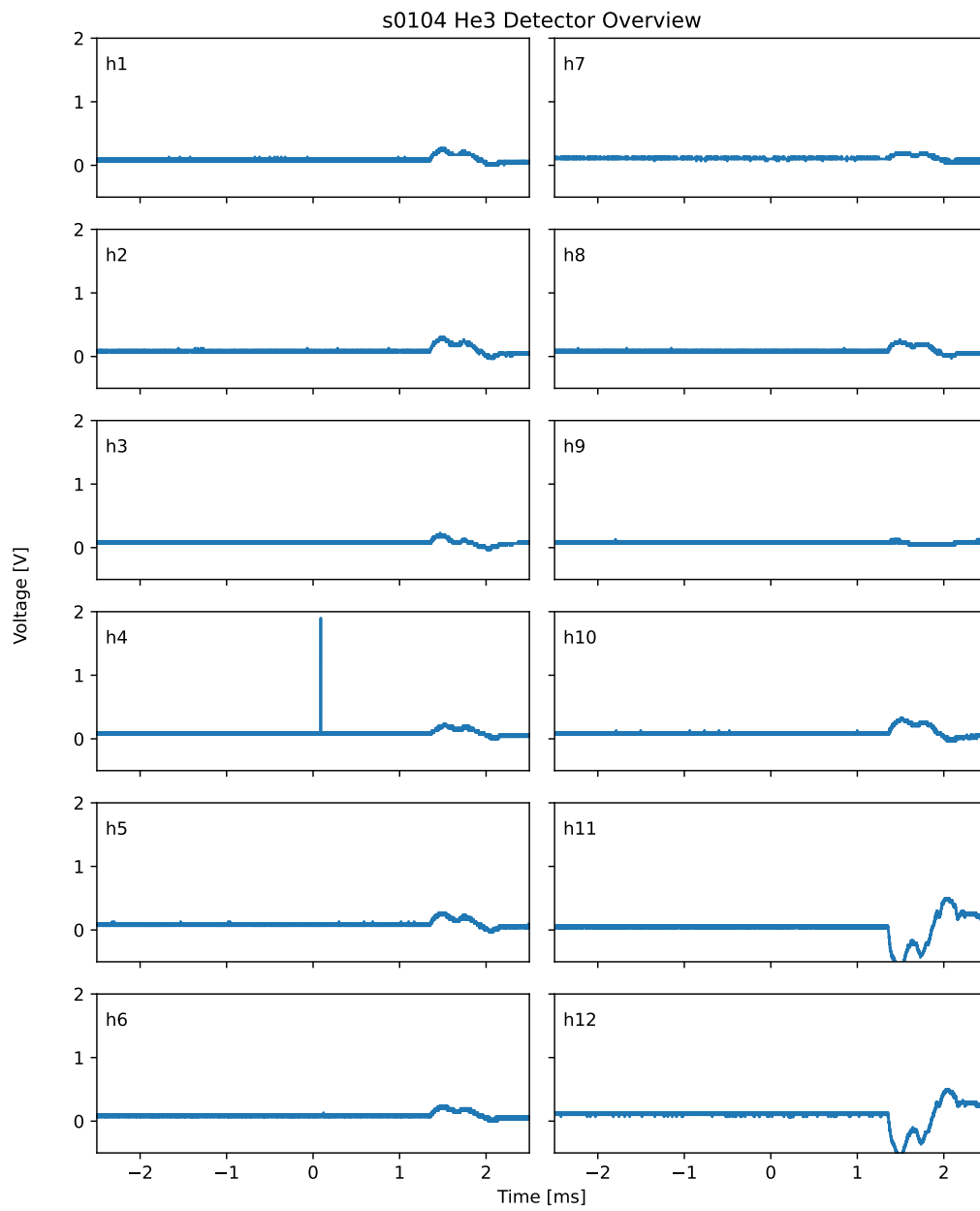
Figure 81. s0104: DD shot.
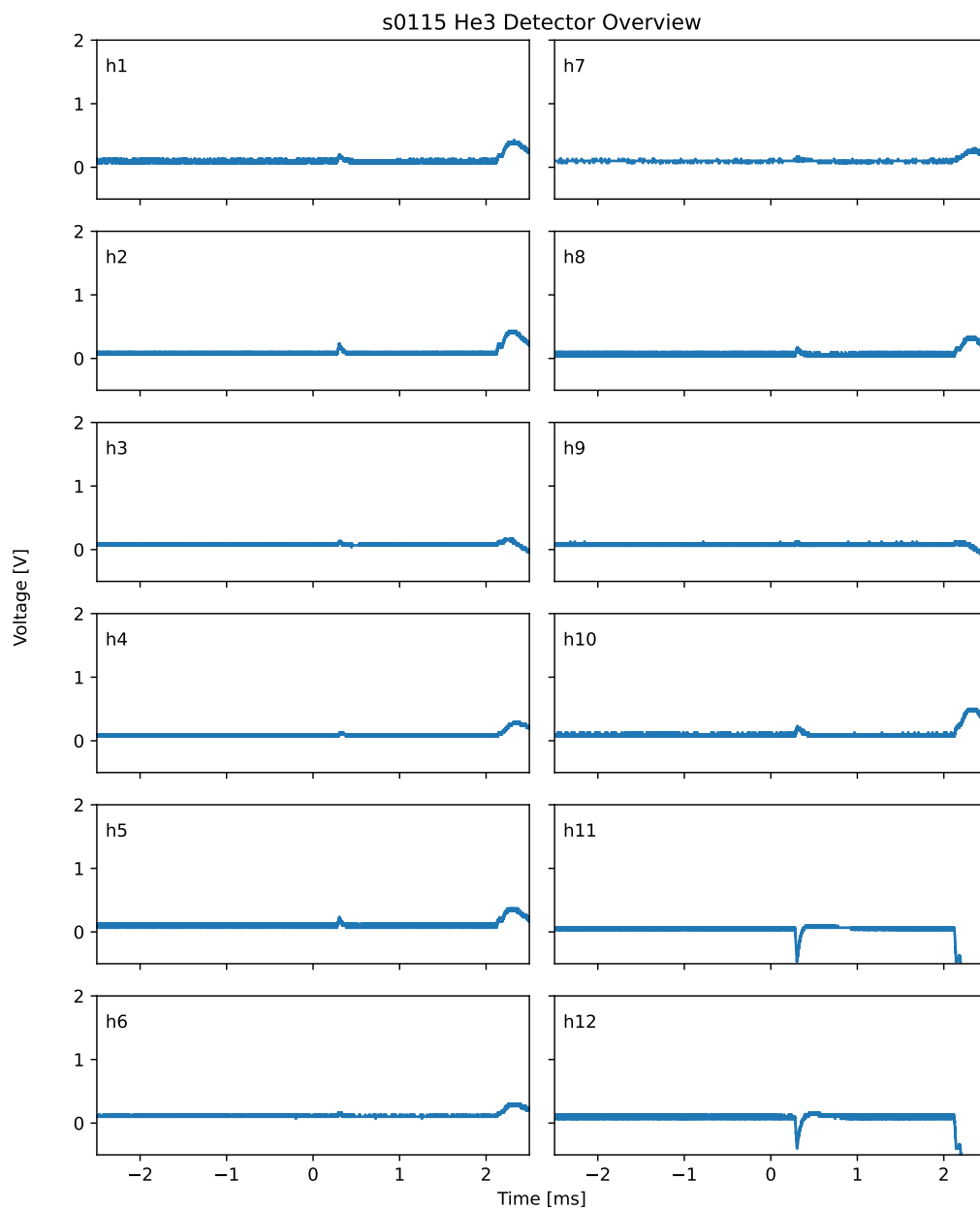
Figure 82. s0115: H$_2$ null shot
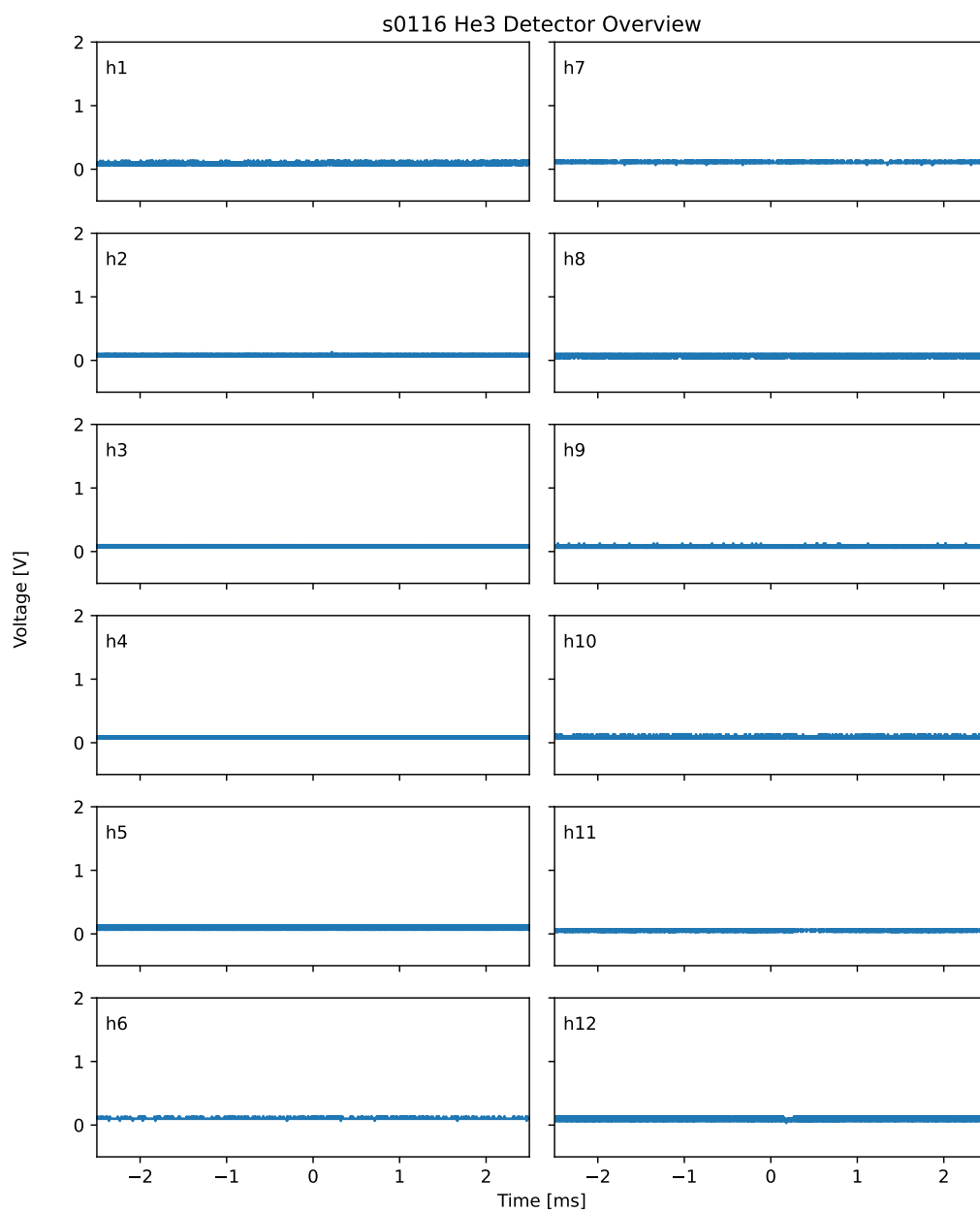
Figure 83. s0116: H$_2$ null shot

Appendix D: Neutron detector locations
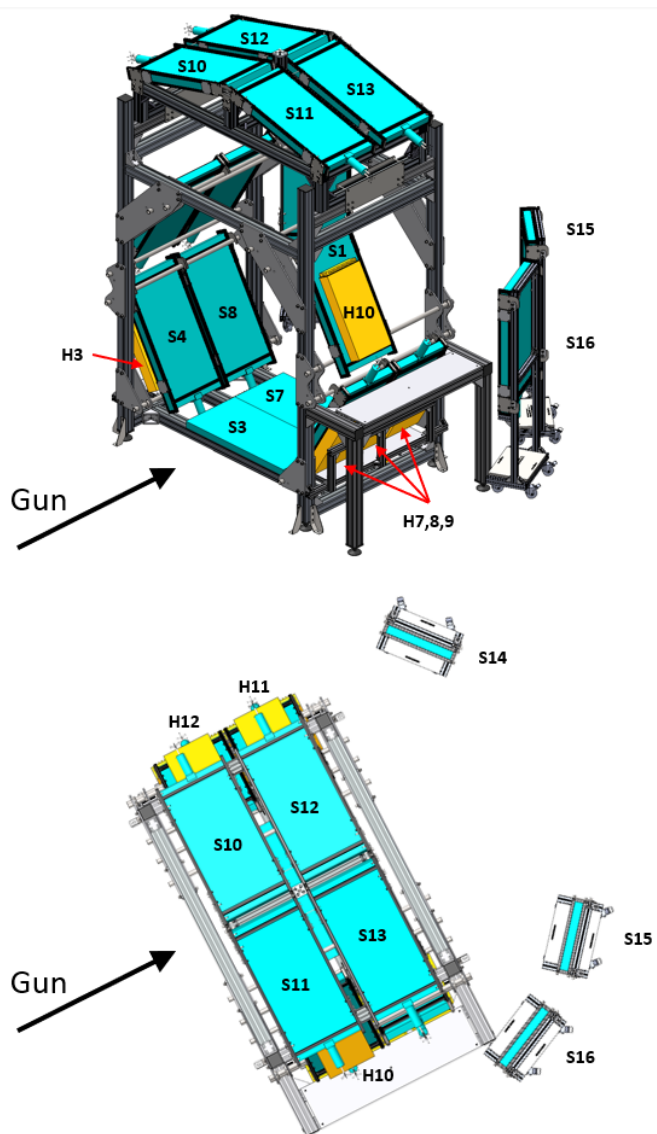
Figure 84. Locations of scintillator (blue, S) and He-3 detector (yellow, H) around the experimental chamber.
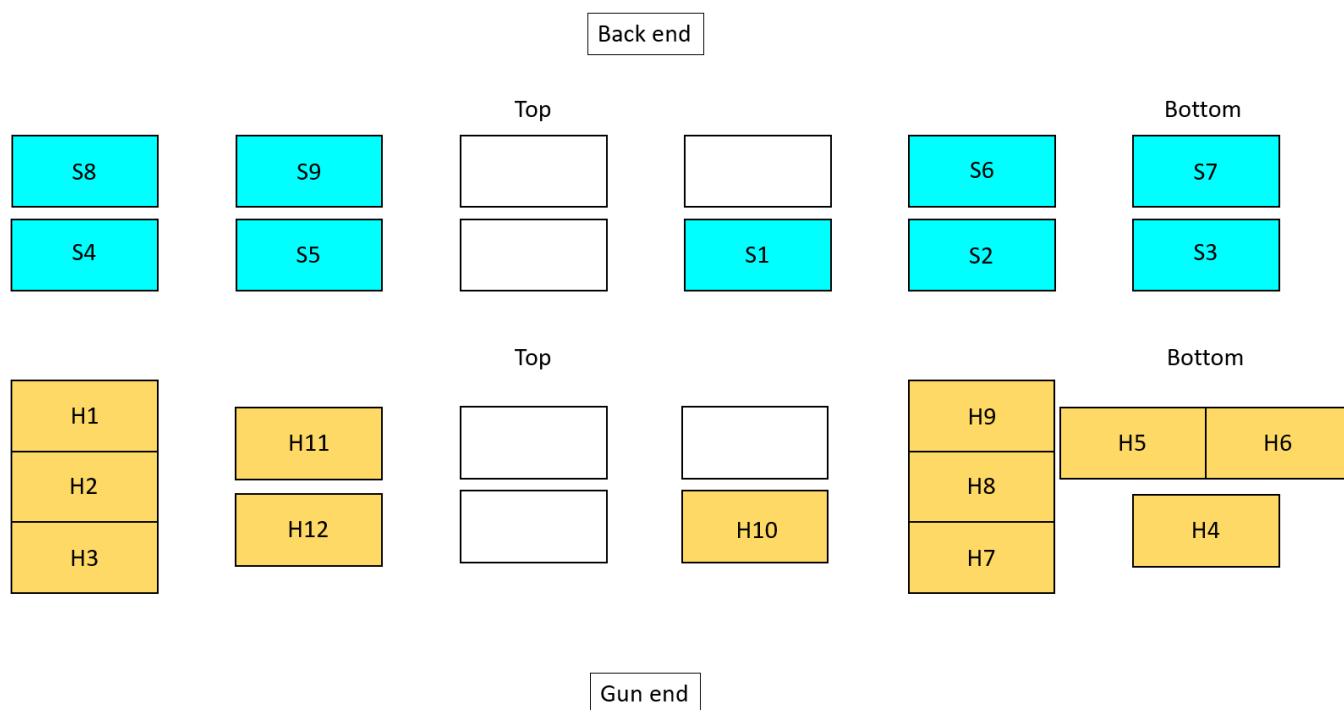
Figure 85. Unfold map of scintillator (blue) and He-3 detector (yellow) locations around the core hexagonal framework. He-3 detectors are located behind the scintillators. For example, H10 is behind S1. White rectangles are vacant locations.

Appendix E: Diagnostic Cable Delays

The cable and response time delays for each diagnostic, the scope and channel they are using and the label for this diagnostic are summarised in Table IX. The detailed calculation of the delay associated with each diagnostic is summarised in Table X. The value of $t_{\text{ion\_offset}}$ used for each shot is shown in Table XI.

| Diagnostic	Diagnostic label	Cable number	Scope	Scope Channel	Cable/diagnostic delay [ns]
Time fiducial	t0_1		8ch1	1	0
Passive fibre 1	passive 1	17	8ch1	2	170
Passive fibre 2	passive 2	18	8ch1	3	170
Ionisation pin	ion pin	19	8ch1	4	162
Small PMT	ss1	20	8ch1	5	182
Large PMT 1	s1	1	8ch1	6	190
Large PMT 2	s2	2	8ch1	7	190
Large PMT 3	s3	3	8ch1	8	190
Time fiducial	t0_2		8ch2	1	0
Large PMT 4	s4	4	8ch2	2	190
Large PMT 5	s5	5	8ch2	3	190
Large PMT 6	s6	6	8ch2	4	190
Large PMT 7	s7	7	8ch2	5	190
Large PMT 8	s8	8	8ch2	6	190
Large PMT 9	s9	9	8ch2	7	190
Large PMT 10	s10	10	8ch2	8	190
Time fiducial	t0_3		8ch3	1	0
Large PMT 11	s11	11	8ch3	2	190
Large PMT 12	s12	12	8ch3	3	190
Large PMT 13	s13	13	8ch3	4	190
Large PMT 14	s14	14	8ch3	5	190
Large PMT 15	s15	15	8ch3	6	190
Large PMT 16	s16	16	8ch3	7	190
Room APD		29	8ch3	8	150
Time fiducial	t0_4		4ch1	1	0
He3 detector 1	h1	21	4ch1	2	150
He3 detector 2	h2	22	4ch1	3	150
He3 detector 3	h3	23	4ch1	4	150
Time fiducial	t0_5		4ch2	1	0
He3 detector 4	h4	24	4ch2	2	150
He3 detector 5	h4	25	4ch2	3	150
He3 detector 6	h6	26	4ch2	4	150
Time fiducial	t0_6		4ch3	1	0
He3 detector 7	h7	27	4ch3	2	150
He3 detector 8	h8	28	4ch3	3	150
He3 detector 9	h9	29	4ch3	4	150
Time fiducial	t0_7		4ch4	1	0
He3 detector 10	h10	30	4ch4	2	150
He3 detector 11	h11	31	4ch4	3	150
He3 detector 12	h12	32	4ch4	4	150

Table IX. Summary of all diagnostics, their associated time delays, and which scope and channel they are connected to.

Diagnostic	Components				Total delay [ns]
Passive fibres	2 m Silica optical fibre in chamber	2 m Silica optical fibre to APD	APD internal delay	30 m LBC240 Extraflex to scope	
Delay [ns]	10	10	0	150	170
Ionisation pin	Probe internal delay	30 m LBC240 Extraflex to scope			
Delay [ns]	12	150			162
Small PMT	PMT internal delay	3 m RG58 in chamber	30 m LBC240 Extraflex to scope		
Delay [ns]	17	15	150		182
Large PMTs	PMT internal delay	30 m LBC240 Extraflex to scope			
Delay [ns]	40	150			190
He3 detectors	30 m LBC240 Extraflex to scope				
Delay [ns]	150				150

Table X. Table showing how the diagnostic delay was calculated for the large and small PMTs, the He3 detectors, passive fibres and ionisation pin.

Shot number	$t_{0IP}[ns]$
86	11.65
87	11.21
88	10.50
89	12.83
90	11.32
91	11.13
92	9.62
94	10.66
95	9.87
99	5.07
100	12.24
101	15.32
102	16.15
103	19.97
104	14.40
115	14.38
116	11.44

Table XI. Table showing t_{0IP} [ns], described in III G, for each shot. This variable, t_{0IP}, is the time between the ion pin firing and the fusion event occurring.

Appendix F: Small detector inside the chamber

A small format scintillator-photomultiplier tube (PMT) detector was placed inside the target chamber to record time-of flight data at the minimum possible distance from the fusion event. At 15 cm from the target, the solid angle subtended by the 100×200 mm detector area is 0.705 sr, or 11% of the full 4π solid angle. This is equivalent to 1.6 large format detectors placed at 1 m. Neutron time-of-flight over 15 cm is 6.9 ns, compared to 46.2 ns over 1 m. The close proximity and small n-TOF uncertainty for a small format detector makes it suitable for validation of the ionisation pin t_0 diagnostic.

To protect the small detector and avoid the hazardous materials being released from the PMT, it was encased in a 10 mm thick steel box, and placed under the target rather than behind the target along the axis of impact. The positioning of the detector inside the chamber can be seen in Fig. 86a. The box containing the detector is secured to other shielding around the target area with a G-clamp. Power for the detector is provided by an SHV connection via a vacuum feedthrough flange on the chamber exterior, and a BNC signal cable is also fed via the same flange.
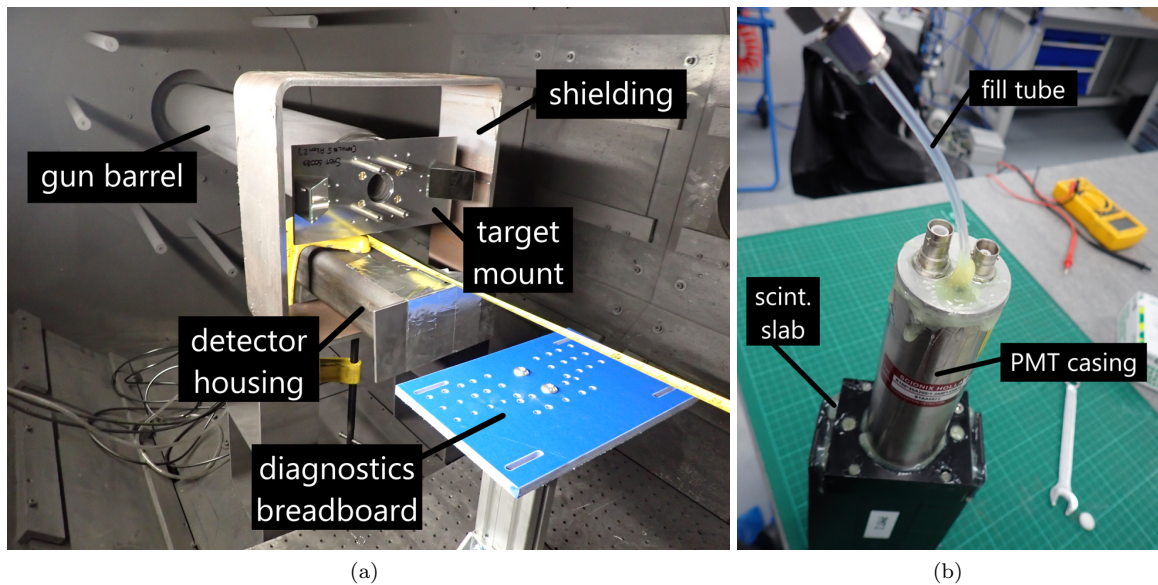

Figure 86. Fielding a small detector inside the target chamber. (a) The small detector positioned inside the target chamber, encased in a steel box and secured to a larger section of steel shielding with the yellow G-clamp. The target is attached to the four small rods in the centre of the image. (b) The modifications to the PMT casing to stop the high voltage breakdown under vacuum.

The PMT suffers electrical breakdown as the vacuum pressure is decreased (falling into the minimum of the Paschen curve for air), causing the power supply to trip. To fix this, the PMT casing was pressure sealed and fed nitrogen from outside the target chamber. A photograph of the modified PMT casing is shown in Fig. 86b. Leaks were identified and sealed with epoxy, and the gas fill tube was glued to a hole made in the top of the PMT housing.

Appendix G: Fusion experiment MCNP model geometry

Num	Material	Density (g/cm3)	R	G	B	Reference
1	EJ200	1.023	143	175	143	https://eljentechnology.com/products/plastic-scintillators/ej-200-ej-204-ej-208-ej-212
2	S355 J2H	7.8	143	143	175	https://www.westyorkssteel.com/carbon-steel/s355/
3	SS304	8	175	143	143	https://www.pnnl.gov/main/publications/external/technical_reports/PNNL-15870Rev1.pdf
4	Mild Steel 43a	7.8	175	159	143	https://matmatch.com/materials/minfm21427-bs-4360-grade-43a-hot-rolled
5	AISI 4330 Mod	7.84	143	175	175	https://www.ssa-corp.com/documents/Data%20Sheet%204330-AMS-6411-UNSK23080.pdf
6	Tantalum	16.654	159	175	143	https://www.pnnl.gov/main/publications/external/technical_reports/PNNL-15870Rev1.pdf
7	Concrete	2.3	192	192	192	https://www.pnnl.gov/main/publications/external/technical_reports/PNNL-15870Rev1.pdf
8	Al 6060	2.7	175	143	175	https://www.aalco.co.uk/datasheets/Aluminium-Alloy-6060-T5--Extrusions_144.ashx
9	Polyethylene	0.93	143	159	175	https://www.pnnl.gov/main/publications/external/technical_reports/PNNL-15870Rev1.pdf
10	Al 6082	2.7	175	143	159	https://www.nedal.com/wp-content/uploads/2016/11/Nedal-alloy-Datasheet-EN-AW-6082.pdf
11	SS303	8.027	159	143	175	https://www.ss303.com/303-stainless-steel-material-data-sheet.pdf
12	Al	2.7	128	64	0	
13	He3	0.000627225	0	0	255	

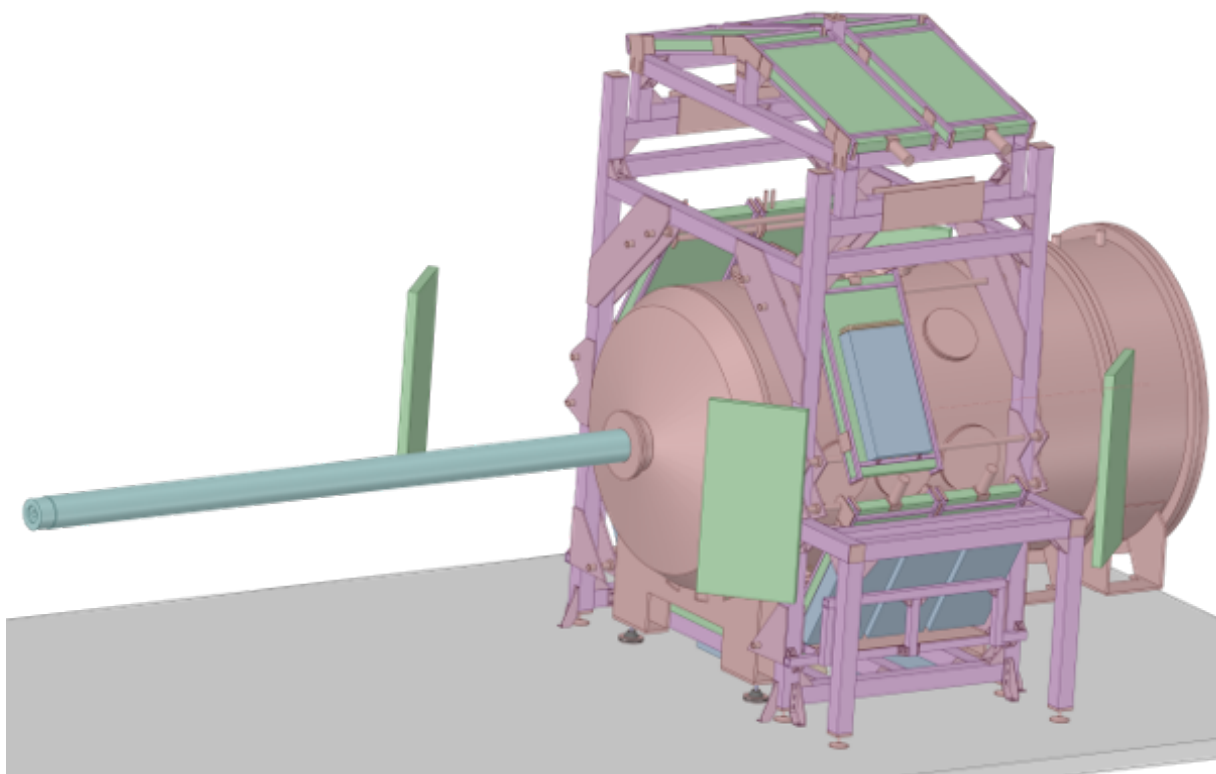Figure 87. Material specifications for the UKAEA MCNP model. Table credit: S. Bradnam, UKAEA.

Figure 88. Simplified 3D CAD input for the UKAEA MCNP model. Image credit: S. Bradnam, UKAEA.
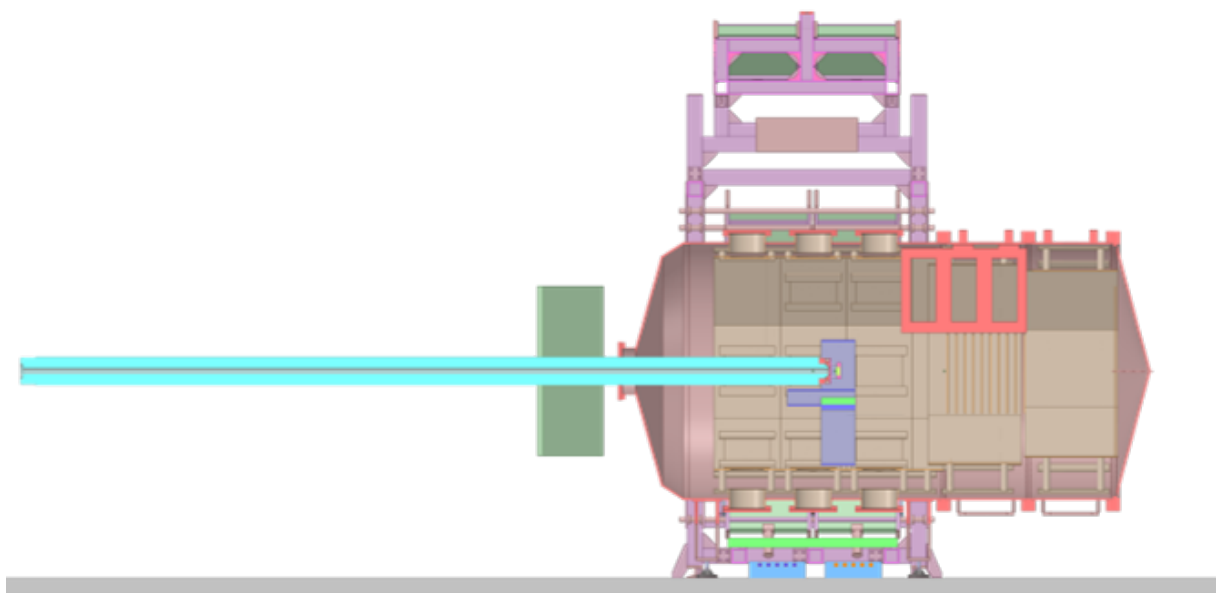

Figure 89. Vertical cut of the simplified 3D CAD input for the UKAEA MCNP model. Image credit: S. Bradnam, UKAEA.
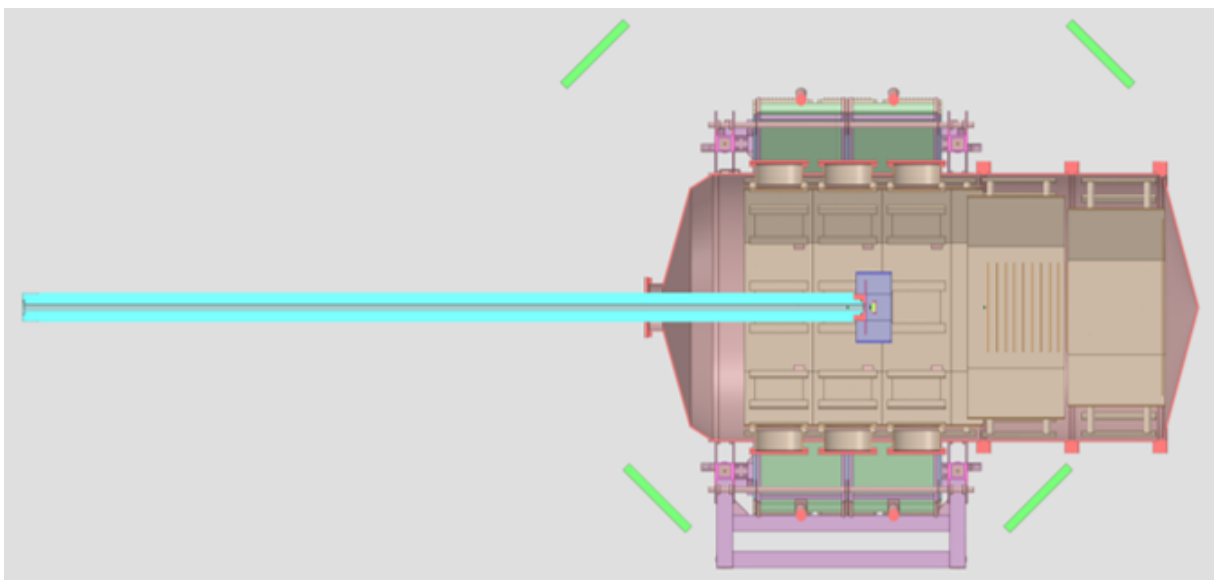
Figure 90. Horizontal cut of the simplified 3D CAD input for the UKAEA MCNP model. Image credit: S. Bradnam, UKAEA.
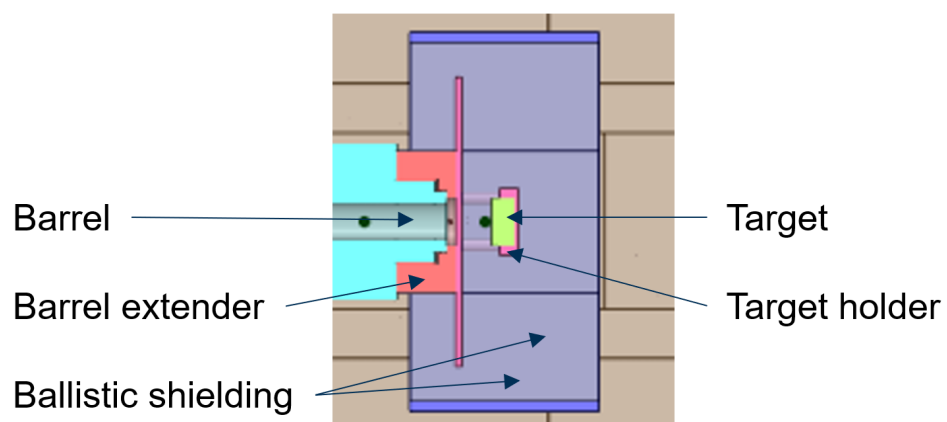

Barrel

Barrel extender

Ballistic shielding

Target

Target holder

Figure 91. Detail of the target region from the simplified 3D CAD input for the UKAEA MCNP model.

[1] G.F. Knoll. *Radiation Detection and Measurement*. Wiley, 2010.